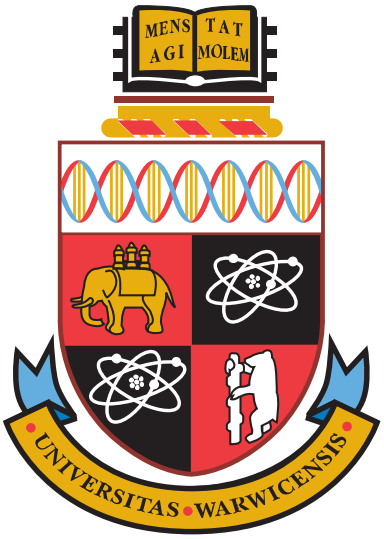

The use of Ultrasound to create Tissue Hyperthermia to support the Treatment of Cancer

by

Adam H. Aitkenhead

Thesis

Submitted to the University of Warwick

for the degree of

Doctor of Philosophy

Department of Physics

November 2008

THE UNIVERSITY OF WARWICK

Contents

List of Tables

List of Figures

Acknowledgements

I wish to express my thanks to my supervisor, Prof. Adrian Wilson, for his guidance and encouragement throughout my four years at Warwick University, especially during the long months of thesis writing. I would also like to thank Dr. John Mills (University Hospital Coventry and Warwickshire) for his advice and encouragement.

I am grateful to everyone in the Physics department mechanical and electronic workshops for their help and advice, especially in machining custom parts for the ultrasound transducers and for providing electronics support for the experimental apparatus.

I am also thankful for the support of the many friends I have made during the course of my studies, especially those with whom I have shared a house at some point (Si, Andre, Eva, Lucia, Christina, Sarah, Naomi, Mary and Sam). Thanks also to Monihar for keeping me sane at lunchtimes.

Finally, I would like to thank my family for all their support and encouragement.

The work described in this thesis was supported by the Engineering and Physical Sciences Research Council through a Doctoral Training Award.

This thesis was typeset with LaTeX 2$_\varepsilon$[1] by the author.

Let everything that has breath praise the Lord.

Psalm 150:6

[1] LaTeX 2$_\varepsilon$ is an extension of LaTeX. LaTeX is a collection of macros for TeX. TeX is a trademark of the American Mathematical Society. The style package *wnewthesis* was used.

Declarations

The work for this thesis was carried out in the Department of Physics at the University of Warwick from September 2004 to July 2008. It is the result of my own independent research except where specifically referenced in the text and has not been previously submitted for any other degree.

Material from this thesis has been published in part in the following paper. In addition, it is hoped that further material (particularly the results of chapter 7) will be submitted for publication in the near future.

Aitkenhead AH, Mills JA, and Wilson AJ. The design and characterization of an ultrasound phased array suitable for deep tissue hyperthermia, *Ultrasound Med Biol*, 34(11):1793-1807, 2008.

Material from this thesis has also been presented by the author at the following conferences:

Aitkenhead AH, Mills JA, and Wilson AJ. The role of a sensitivity analysis in the design of phased array ultrasound transducers for hyperthermia. Poster presented at the 10th International Congress on Hyperthermic Oncology, Munich, Germany, April 9-12, 2008. URL `http://www.icho2008.org/download/ICHO2008_Abstractbook.pdf`.

Aitkenhead AH, Mills JA, and Wilson AJ. Development of an ultrasound transducer for mild hyperthermia in deep body tumours. Paper presented at the 4th meeting of the UK Therapy Ultrasound Group, London, UK, May 13, 2008.

Abstract

The value of mild hyperthermia in improving the outcome of radiotherapy and chemotherapy treatments is well established. However, clinical applications are currently restricted to accessible tumours, with the application of controlled hyperthermia in solid tumours deep within the body presenting an unresolved problem. Ultrasound is an attractive heating technique because of its ability to create a focus at depth which can be steered around the tumour volume. However, despite considerable research no clinically usable transducers for deep tumour applications have resulted.

In this thesis the underlying principles that govern the characteristics of phased array transducers have been examined. The concept of an idealised phased array has been introduced, and analysis of simulated fields from such arrays has enabled a new set of equations to be defined which relate the geometry of the field to the fundamental array design parameters (including the array diameter, radius of curvature and frequency of operation). Further simulations have examined the impact of secondary array design parameters (such as the individual element size, number density and layout geometry) which modify the field from that of the idealised case. Analysis of these has enabled an upper limit to be placed on the element size within any planar array in order to prevent undesirable changes in the characteristics of the focal region.

A fifteen element phased array with a random element distribution has been constructed based on the design principles established in the simulation work. Measurements of the inter-element cross-coupling have been made, demonstrating that acoustic coupling dominated for inter-element pitches of less than 8 mm, while electrical coupling dominated at larger inter-element pitches. The field produced by the array in an acoustic tank has been characterised and compared against simulation predictions, showing good agreement in terms of the geometries of the focal region and the grating lobes. However, a number of differences have also been identified. In particular, the focal region was closer to the surface of the physical transducer in the measured fields compared to the simulation results, and there were numerous small high intensity regions between the surface of the transducer and the focus which were absent from the simulated fields. A sensitivity analysis, using a simulated factorial experiment, has been performed to identify the origin of these differences, with the results indicating that the presence of a secondary vibrational mode within the elements of the array was the principal causative factor.

Finally, calculations have been performed which demonstrate the feasibility of manufacturing an array suitable for the application of mild hyperthermia in deep tumours based on the array design scheme presented in this thesis. Potential extensions of the array design have also been described which would improve the behaviour of the array under steering and provide further increase in the focal intensity.

Abbreviations

ASCII	American Standard Code for Information Interchange
CW	Continuous Wave
DAC	Digital to Analogue Converter
DC	Direct Current
DNA	Deoxyribonucleic Acid
FET	Field Effect Transistor
FUS	Focussed Ultrasound Surgery
HIFU	High Intensity Focussed Ultrasound
HILP	Hyperthermic Isolated Limb Perfusion
PVDF	Polyvinylidene Fluoride
PZT	Lead Zirconate Titanate
RF	Radio-frequency
RMS	Root Mean Square
RNA	Ribonucleic Acid
USB	Universal Serial Bus
WBH	Whole Body Hyperthermia
WLS	Weighted Least Squares

Chapter 1

Introduction

By definition, hyperthermia is an elevation in the temperature of either the entire body or a region of it to above the normal body temperature of 37°C. Increasing the temperature of tissue results in a number of physical and physiological changes which depend on the magnitude of the temperature increase as well as the length of time for which the elevated temperature is maintained. These changes provide several routes for the application of hyperthermia as part of the treatment of cancer, including ablation techniques which destroy tissue directly and mild hyperthermia techniques which are used as an adjunct to radiotherapy and chemotherapy.

Within this chapter the principal applications of hyperthermia in the treatment of cancer will be described in brief, touching on the physiological effects upon which the uses of hyperthermia in the treatment of cancer are based, and describing the results of clinical trials which demonstrate its value. The techniques that are used to create hyperthermia either clinically or in the laboratory will also be described, highlighting the capabilities of each technique and the applications to which each is best suited. Hynynen [1988] reported that ultrasonic methods are the only suitable heating techniques for non-invasive localised heating of deep tumours, and therefore ultrasonic heating techniques and their application will be described in greater detail.

1.1 Applications of hyperthermia in the treatment of cancer

Hyperthermia can produce a number of different physiological responses in tissue, depending on the temperature attained, the duration of the temperature elevation and the characteristics of the tissue itself. These physiological responses provide several routes by which hyperthermia may be used in the treatment of cancer, both on its own and as an adjunct to other treatment modalities (particularly radiotherapy and chemotherapy). In the following sections the main hyperthermic treatment modalities will be described, along with a discussion of the relevant physiological mechanisms and clinical trial results for each modality.

1.1.1 Hyperthermia and direct cytotoxicity

The application of heat to a region of tissue may produce a cytotoxic effect, such that it can be used to destroy cells directly, and without any accompanying radiotherapy or chemotherapy. This cytotoxic effect has been described in reviews such as that by Hildebrandt et al. [2002], who notes that the susceptibility of cells to hyperthermia and the mechanism by which cell death occurs depend on several factors, such as the temperature attained, the duration of the heating, and the phase of the cells in the cell-cycle. However, two general cell death processes which result directly from hyperthermia can be identified: apoptosis and necrosis. These two cell death mechanisms are described by Kerr et al. [1994], and can be summarised as follows:

- Apoptosis:

  Apoptosis is a cell death process that occurs within normal tissue, most commonly where cells die to balance the number of new cells produced by mitosis. As such, apoptosis tends to occur to individual cells scattered throughout a region of tissue. When a cell dies via apoptosis, the process begins with the cell nucleus breaking into discrete fragments which disperse throughout the cell. Within a few minutes of this occurring the cell splits into membrane enclosed bodies, and over the next few hours each of these is phagocytosed

and ingested by nearby cells.

- Necrosis:

  In contrast to apoptosis, necrotic cell death begins with the disruption of membranes and organelles within the cell, and is followed by the disintegration of the cell membrane itself. The constituents of necrosed cells are not phagocytosed by the surrounding cells, instead they remain in place until removed by mononuclear phagocytes. An influx of these phagocytes may be stimulated by necrosis, since necrosis, unlike apoptosis, tends to provoke an immune response [Bold et al., 1997]. In addition, necrosis generally occurs within groups of adjacent cells, unlike apoptosis, which occurs to individual cells scattered throughout a volume of tissue.

Hyperthermia produces an enhancement of apoptosis within tissue when the temperature is increased to above approximately 42°C for periods of 30 minutes or more. The value of this threshold temperature may vary depending on the tissue type, but the cytotoxicity changes sharply as the threshold is exceeded, with cytotoxic and non-cytotoxic temperatures differing by as little as 0.2°C [ter Harr, 1999]. At temperatures above the threshold the enhancement of apoptosis is accompanied by other changes to the cell-cycle, with cellular reproduction slowing down or ceasing. The heat-sensitivity of cells is dependent on their phase in the cell-cycle, being most sensitive during the S-phase (DNA synthesis) and M-phase (mitosis) [Hildebrandt et al., 2002] with the result that sensitivity tends to be high for rapidly proliferating tissues (such as tumours) relative to normal tissue [Kerr et al., 1994].

Hyperthermia produces an enhancement of necrosis when tissue is heated to temperatures > 46°C for periods of 30 minutes or more [Kerr et al., 1994]. The required heating time decreases as the temperature is increased [Dewhirst et al., 2003], and when temperatures of about 60°C are applied coagulative necrosis occurs within 1-2 seconds [ter Harr, 1999].

Techniques which are aimed at killing selected volumes of tissue by using the direct cytotoxic effect of hyperthermia tend to be based on the necrotic cell death mechanism, since it is comparatively straightforward to achieve and control

the required high temperatures for a short period of time. Both non-ultrasonic and ultrasonic heating techniques may be used to achieve these high temperatures, and these will be discussed in sections 1.2 and 1.3 respectively. In contrast, the application of hyperthermia alone to achieve a cytotoxic effect by apoptosis is more difficult, requiring that a localised elevated temperature be maintained within the narrow range required for apoptotic cell death: above the apoptosis threshold temperature (42°C) but below the temperature of the onset of necrosis (46°C).

In summary, both apoptosis and necrosis provide routes that may be utilised in the treatment of cancer for killing tissue within solid, localised tumours. It should also be noted however, that these cell death pathways also mean that excessive heating of healthy tissue during hyperthermic treatments must be avoided, as otherwise normal cells will also be killed by the hyperthermia.

1.1.2 Hyperthermia and radiotherapy

Radiotherapy involves the application of ionising radiation to damage DNA within cell nuclei, which in turn promotes cell death by apoptosis [King, 2000]. Mild hyperthermia can improve the efficacy of radiotherapy via several mechanisms. The most important of these are related to the impact of hyperthermia on tumour oxygenation and on the DNA repair mechanism.

Let us consider the importance of tumour oxygenation first. It is well known that hypoxic cells are more resistant to ionising radiation. For example, Brizel et al. [1999] noted in their study of patients with head and neck cancer being treated with radiotherapy alone that local regional control, disease free survival and survival were all better by a factor of two for the group of patients with well oxygenated tumours in comparison to those with hypoxic tumours. Hyperthermia is a suitable method for increasing tumour oxygenation since one of the primary physiological responses to the heating of tissue is an increase in perfusion as the body attempts to regulate the temperature of the heated region, and with increased perfusion comes improved oxygenation [Hildebrandt et al., 2002]. This increase in tumour oxygenation with heating has been demonstrated in a clinical context by Jones et al. [2004], who found

that there was a significant improvement in oxygenation in tumours of the breast when hyperthermia was applied.

It should be noted that the impact of hyperthermia on tumour oxygenation depends upon the temperature to which the tumour is heated. While hyperthermia at relatively low temperatures (< 42°C) typically leads to an increase in tumour perfusion, heating to higher temperatures (> 42°C) can actually result in a decrease in tumour perfusion [Hildebrandt et al., 2002]. There is therefore a window of optimal temperature to which a tumour should be heated in order to maximise its oxygenation and its radio-sensitivity.

It should be noted that hyperthermia is not the only method of increasing the tumour oxygenation, but it is an attractive method since it does not require the use of drugs. Breathing of carbogen (95% 0_2, 5% CO_2) is another potential route, but Griffin et al. [1996] reported in their study on murine leg tumours that localised hyperthermia produced greater radio-sensitisation of the tumour than did the breathing of carbogen. They postulated that this may be because the increased oxygenation due to hyperthermia is longer lasting. This is consistent with the work of Jones et al. [2004] who noted that increased oxygenation of human tumours by hyperthermia can last for over 24 hours.

The second of the two main mechanisms by which hyperthermia can improve the efficacy of radiotherapy is through the inhibition of DNA repair. Work by Jorritsma and Konings [1983] investigated the effect of hyperthermia on the repair of radiation induced DNA strand breaks in *in-vitro* murine tumour cells, demonstrating that hyperthermia has a strong impact on DNA repair. There were three relevant findings:

1. The level of DNA repair inhibition increased with the temperature of the pre-radiation hyperthermia, with data reported for temperatures of 42°C to 45°C.
2. Increasing the duration of the hyperthermia also increased the repair inhibition.
3. DNA strand breaks occurred due to hyperthermia alone for treatment temperatures of 44°C or greater and treatment durations of the order of an hour

or more, resulting in an enhancement of cell death by apoptosis due to heat alone as described in section 1.1.1.

Others have reported similar findings, and have observed DNA repair inhibition at temperatures as low as 40°C [Dewhirst et al., 2005].

The mechanism by which hyperthermia inhibits DNA repair is complex. As noted by Iliakis et al. [2008], there exist a number of pathways by which the repair of DNA double strand breaks may be inhibited. The processes involved in each of these are not well understood, but could be generalised as relating to protein denaturation, aggregation and redistribution, all of which act to inhibit DNA repair [Lepock, 2004].

The enhancement of tumour oxygenation and the inhibition of DNA repair occur in a similar temperature range (40-45°C), and this overlaps with the range of temperatures required for the enhancement of apoptosis due to heat alone (42-46°C - section 1.1.1). It is difficult to control the temperature throughout a tumour with enough uniformity that only one of these mechanisms occurs, and therefore clinical applications of hyperthermia as an adjunct to radiotherapy may involve all of these processes. In any case, the results of clinical trials are clear in showing an enhancement of the radiation response as a result of hyperthermia. For example, trials reported by Jones et al. [2005] and Vernon et al. [1996] showed improvements in the complete response rate of 24% and 18% respectively for hyperthermia and radiation in comparison to radiation alone. An additional benefit of hyperthermia was noted by Jones et al. [2005], who observed a pronounced improvement in local control amongst patients who had been previously irradiated. These examples, in common with many other clinical trials, were based upon the treatment of superficial tumours. Results of trials studying the effect of hyperthermia on deep tumours are lacking in the literature, principally because it is difficult to heat such tumours adequately [Sherar et al., 1997]. However, the large enhancements in the response observed when hyperthermia is applied as an adjunct to radiotherapy for superficial tumours indicate that further work to make controlled hyperthermia clinically feasible in deep tumours could be highly beneficial.

1.1.3 Hyperthermia and chemotherapy

Chemotherapeutic treatment involves the use of drugs which disrupt the cell cycle in various ways, depending on the particular drug, with the intention of promoting cell death by apoptosis within the tumour. There are several ways in which mild hyperthermia can improve the efficacy of chemotherapy: the three most important of these concern [i] its role as a chemo-sensitising agent, [ii] the role it can play in the delivery of drugs and [iii] its impact on drug resistance.

Firstly, hyperthermia can act as a sensitising agent, improving the efficacy of drugs in much the same way as it acts as a radio-sensitiser, since the effects caused by chemotherapeutic drugs (such as damaging or disrupting the function of RNA, DNA and protein molecules within the cell [King, 2000]) are similar to those produced by ionising radiation.

Both systemic and localised hyperthermia can be of benefit when applied in conjunction with chemotherapy. [Hildebrandt et al., 2005] reported that chemotherapy in combination with systemic heat treatment produced a greater response than chemotherapy alone for patients with disseminated malignancies. But localised heating, which enhances the sensitivity only within the tumour, is often particularly advantageous since chemotherapy is generally delivered systemically.

The second way in which hyperthermia can benefit chemotherapy is in the drug delivery mechanism. Malignant tumours can be poorly perfused, and this can impede chemotherapeutic treatment since drug delivery comes via the blood. One of the primary physiological responses to mild hyperthermia (at temperatures $<$ 42°C) is an increase in perfusion as the body attempts to regulate the temperature of the heated region [Hildebrandt et al., 2002]. Localised hyperthermia is therefore beneficial since it increases the perfusion within the tumour, and therefore also increases the drug uptake relative to the normothermal tissue.

Hyperthermia can also aid drug delivery when liposomes are involved. Liposomes are vesicles composed of a lipid bilayer enclosing an aqueous volume within which drugs can be contained [Kong and Dewhirst, 1999]. The key attribute that makes liposomes attractive is that they prevent release of the drug into the blood

when the temperature is below their transition temperature. If the temperature exceeds the transition temperature then they undergo a change of phase and allow the contents of the lipid bilayer envelope to be released [Yatvin et al., 1978]. Using liposomes in combination with localised hyperthermia can therefore trigger the release of a drug within a target region, maximising the drug concentration (and therefore activity) within the tumour. Since the drug concentration elsewhere in the body will be much lower, this also has the potential to minimise the side-effects of the chemotherapy [Ponce et al., 2006].

Finally, it has been reported that hyperthermia can reduce or reverse drug-resistance [Mansouri et al., 1989; Lage et al., 2000]. However, the mechanism by which this occurs is so far unclear.

The enhanced effectiveness of chemotherapy due to hyperthermia has been demonstrated in *in-vitro* cancer cells [Nakao et al., 2000], in animals [Hahn et al., 1975] and in human clinical trials [di Filippo et al., 1998]. As with radiotherapy, the reported trials for hyperthermia as an adjunct to chemotherapy tend to be based on accessible and superficial tumours, and trials involving localised hyperthermia of deep tissue are lacking.

1.2 Non-ultrasonic heating techniques

Many techniques for the creation of hyperthermia *in-vivo* exist, and within this section the principal non-ultrasonic techniques will be briefly described. The spatial resolution of these techniques ranges from those which create hyperthermia throughout the whole body, through techniques which create regional hyperthermia, to techniques which are highly localised.

- Coley's toxins:

  In the late 1800s, William Coley developed a method for the treatment of certain cancers (especially soft tissue sarcomas) which originated from observations of cases where tumours had decreased in size or disappeared following attacks of various infectious diseases, particularly of erysipelas [Coley, 1891].

The treatment involved the preparation of what has become known as 'Coley's toxins', a mixture of heat-killed bacterial cultures that would be delivered to the patient through a course of injections with the aim of producing an immunological response [Starnes, 1992]. Development of a fever lasting 12-24 hours was part of the immunological response to each injection, and so over the course of the treatment the patient would undergo multiple periods of Whole Body Hyperthermia (WBH). The mechanism behind this treatment remains unclear [Tsung and Norton, 2006], and whether the fever itself is directly beneficial or is merely part of an overall immune response is unknown.

While parallels may be drawn between these repeated fevers and other hyperthermic treatment modalities, one clear difference is that the high fever temperatures in Coley's mode of treatment were caused by the body's own immune response rather than by the application of active heating to the body. In addition, it should be noted that since the primary aim of Coley's mode of treatment was to stimulate the immune system, such a method of creating hyperthermia is of limited compatibility with more common forms of cancer treatment (such as radiotherapy and chemotherapy), all of which compromise the patient's immune system to some degree.

- Radiative heating:

  Radiative heating is a technique which enables whole body hyperthermia (WBH) to be applied through the use of infra-red radiators. A description of the technique has been reported by Hildebrandt et al. [2005]. Two main types of radiative applicators exist, with the patient positioned within either a 'closed-chamber' or an 'open-chamber'. These two types of applicator each have their own advantages: 'closed-chamber' devices allow the environment within the chamber to be tightly controlled in terms of humidity, while 'open-chamber' devices allow more convenient access to the patient during treatment. In addition, differences in the frequencies of the infra-red radiation exist between the various applicators which affects the penetration depth of the radiation into the patient. Localised heating is not possible with radiative

heating techniques.

- Perfusion techniques:

  Hyperthermia may be applied to isolated organs by controlling the temperature of the blood using a perfusion circuit external to the body. The technique may be used for organs such as the lung, pleura or liver [Baronozio and Hager, 1998a], or for isolated limbs, in which case the treatment is called Hyperthermic Isolated Limb Perfusion (HILP) [Knorr et al., 2006]. Perfusion techniques provide good temperature control and are generally used as an adjunct to chemotherapy, enabling higher drug concentrations to be used in comparison to standard chemotherapy since the drug may be delivered to the organ or limb in isolation from the rest of the body. However, perfusion techniques carry some risk of adverse effects such as nerve damage [Wust et al., 2002]. Also, highly localised heating is not possible with perfusion heating techniques.

- Convective heating:

  Convective heating techniques involve heat transfer to tissue from a heated medium which is in contact with the tissue, such as a wax or water bath. This technique may be used either for WBH or for heating of individual limbs, and is commonly used for creating hyperthermia in laboratory work on small animals (as in the work of Song et al. [2005] for example). While it may also be used for hyperthermia in humans, it is associated with excess toxicity [Hildebrandt et al., 2005] and so alternative methods may be preferred.

- Magnetic nanoparticles:

  Nanotechnology provides a method of heating using a colloid of magnetic particles which is injected into the tumour and activated by an alternating magnetic field (typically at 50-100 kHz for humans or higher frequencies for studies on mice [Jordan, 1999]), thus producing heat. The technique uses iron-oxide nanoparticles to maximise the heating efficiency, and surface coatings are used to delay targeting by the immune system [Baronozio and Hager, 1998b]. Highly localised heating patterns can be achieved by administering the nanoparticles

within a target region, but the treatment is not non-invasive.

- Radio-frequency Ablation:

  In this technique electrodes are either positioned on the surface of the body or are inserted via a catheter into the target region, and a radio-frequency (RF) current (typically at 100-500 kHz [Baronozio and Hager, 1998a]) is applied. RF agitation of ions which compose the current within the tissue produces frictional heating.

  RF heating techniques are typically used for ablation since the heating can be confined to a highly localised region. Using a single interstitial electrode the power deposition in the surrounding tissue is inversely proportional to the square of distance [Curley, 2001], and so the temperature decreases rapidly away from the electrode. The region to be ablated is typically larger than the volume that can be lesioned by a single electrode, and therefore either several electrodes may be used, or else a single electrode must be repeatedly repositioned to allow multiple lesions to cover the target volume. RF ablation techniques are therefore invasive, and may also involve open surgery to provide access for the treatment of deep tumours.

- Electromagnetic heating:

  Electromagnetic heating techniques may be used to provide non-invasive, regional heating of tissue. Depending on the frequency of the applied electromagnetic field, heating can occur by one of two mechanisms: inductive heating or capacitive heating [Stauffer, 2005]. Inductive heating dominates within radio-frequency fields, where the frequency is in the region of 10-20 MHz, with the heat being deposited by induced currents as a result of resistive losses. Capacitive heating is dominant at microwave frequencies (above $\sim$100 MHz), and arises due to friction between water molecules which the field has caused to oscillate.

  The penetration depth and spatial resolution that can be achieved by electromagnetic heating depend on the frequency used. High frequencies provide

good localisation of the heating, but on penalty of a shallow heating depth (<2 cm). Conversely, low frequencies allow for a greater depth of heating but give poor spatial resolution because of the relatively large wavelength. The localisation of the heated region is limited to at best half a wavelength, while at 146 MHz, which is at the upper end of the range of frequencies used for deep heating, the wavelength in tissue is ∼20 cm [Lagendijk, 2000].

Various applicators have been developed for heating different parts of the anatomy. Examples include arrays designed for intra-cavitary applications (which typically operate at ∼915 MHz) [Debicki et al., 1995], planar arrays for superficial hyperthermia of the abdomen (also ∼915 MHz) [Johnson et al., 2006] and phased arrays such as the HYPERcollar for localised heating within the head and neck (433 MHz) [Paulides et al., 2007]. Systems designed for deep hyperthermia include the BSD-2000 (70-120 MHz, BSD Medical, Salt Lake City, USA), which may be used in conjunction with a variety of applicators depending on the size of the patient. The Sigma 60 is one such applicator, consisting of a phased array of eight dipoles positioned around the circumference of the body [Sullivan et al., 1992]. It has been used clinically for treatment of deep tumours in the pelvic region since the early 1990s, providing good, reproducible heating of the target region [Fatehi et al., 2007].

While electromagnetic heating systems can provide well controlled heating and are well established in clinical practice, they are unsuitable for highly localised deep heating because of the large wavelength that is essential for adequate depth penetration.

In summary, while these techniques enable heating or ablation of tissue to be performed for a number of applications, none are suitable for the non-invasive, localised heating of deep tissue that is of interest in the present work.

1.3 Ultrasonic hyperthermia

For certain applications, ultrasonic heating techniques provide a number of advantages over the alternative heating techniques already described. In particular, ultrasonic methods can be used to provide highly localised heating of tissue over a wide range of depths. Importantly, ultrasound methods allow tissue to be heated non-invasively (although interstitial techniques also exist). However, ultrasonic techniques are also subject to two main limitations: They are not suitable for heating regions where gas filled cavities exist, such as the lung, since the ultrasound is reflected at the tissue/gas interface; and they are generally not suitable for heating regions close to bones, since there may be unwanted heat deposition at the bone/tissue interface.

Within this section, the principle ultrasonic applications and applicator types will be described. Further information on these can be found in various reviews, such as those by ter Harr [2007] and Diederich and Hynynen [1999].

1.3.1 Ultrasonic applications

There are two main therapeutic applications of ultrasound: High Intensity Focussed Ultrasound (HIFU) and Mild Hyperthermia.

- High Intensity Focussed Ultrasound (HIFU):

  The use of High Intensity Focussed Ultrasound (HIFU), also called Focussed Ultrasound Surgery (FUS), in the treatment of cancer is considered in various reviews, such as those by ter Harr [1995] and Kennedy et al. [2003]. It is a method of destroying regions of tissue non-invasively by using a tightly focussed ultrasound beam to create a rapid rise in temperature to above 60°C at a targeted location, producing the formation of a lesion of ablated tissue. Due to the tight focus, the energy deposited in surrounding tissues is low, leaving surrounding tissues undamaged. HIFU is an attractive method of destroying cancerous tissue as it can be performed non-invasively, eliminating the potential complications that exist with surgery. Depending on the focal

intensity and the pulse duration, HIFU can damage tissue mechanically (via cavitation) or thermally. Cavitation is generally avoided in ultrasound surgery, since the formation of gas bubbles disrupts the ultrasound field and makes precise prediction of the lesioned volume difficult. However, Hu et al. [2007] reported that mechanical HIFU may have additional benefits in that it can induce a systemic anti-tumour immune response.

- Mild Hyperthermia:

  In contrast to HIFU, mild hyperthermia involves raising the tissue temperature by a smaller amount in order to improve the efficacy of some other mode of treatment, such as radiotherapy or chemotherapy, without necessarily reaching cytotoxic temperatures. Definitions of the temperature range for mild hyperthermia vary in the literature, but the key requirement is that the temperature is well below the necrotic threshold. A range of 39-42°C for 1-2 hours was suggested by Dewhirst et al. [2005], and this will be the definition used within the present work.

  While no ultrasound-based system is currently in clinical use for deep, mild hyperthermia applications, a number of systems based on electromagnetic, deep heating are. The key benefit of an ultrasonic heating system would be its increased localisation in comparison to existing electromagnetic systems. This would minimise the radio-sensitisation or chemo-sensitisation of healthy tissue surrounding the tumour, but it may also enable different treatment rationales to be investigated. For example, good localisation of the heat deposition may make it possible to achieve higher temperatures within the tumour volume. This could potentially be beneficial in two ways: Firstly it could lead to a reduction in the treatment time required to provide a desired thermal dose; and secondly it may make it possible to achieve temperatures within the tumour which are in the apoptotic range without causing excessive heating of the surrounding healthy tissue.

1.3.2 Ultrasonic heating techniques

The design of an ultrasound transducer can be tailored to suit the desired application. For convenience, three basic types of transducer can be considered: extra-corporeal transducers; intra-cavitary transducers; and interstitial transducers. An overview of the design approaches will be given here for devices based on the use of piezoelectric materials to generate the ultrasound field. A brief description of piezoelectric materials will be described in chapter 2.

- Extra-corporeal devices:

  Extra-corporeal ultrasound transducers enable an ultrasound field to be created within tissue, thus providing heating due to the absorption of the ultrasound (as will be described in chapter 2). The energy deposition may be targeted to a localised region by focussing the ultrasonic field, and this can be achieved using either physically focussed single element devices or phased arrays.

  Single element devices are commonly used in HIFU treatment, and focussing is achieved through the use of an element with a concave surface. Such physically focussed elements can provide fields with characteristics which are well suited to the requirements for HIFU: The position of the focus relative to the transducer is well known, aiding the targeting of the ablative treatment; the focal geometry for any transducer is simple to predict given the dimensions of the element; and the single element design maximises the focal intensity that can be achieved for a given transducer diameter, since the entire face of the transducer contributes to the field. The simple design avoids potential sources of problems that exist in phased arrays, such as the need for the multiple independent drive channels and the potential problems caused by inter-element cross-coupling.

  However, there is one key drawback which makes single elements impractical for controlled hyperthermia. To maintain an elevated and controlled temperature within a region of tissue requires that the intensity and location of the

focus can be adjusted during the treatment in order to respond to the changes in the temperature distribution in the tissue. For a single element transducer, control of the intensity is straightforward since the drive conditions can be modified, but there is no control of the position of the focus as that is determined by the geometry of the transducer. Moving the position of the focus requires physical movement of the transducer, and the mechanical system required for this may not respond fast enough to control the temperature adequately [Cain and Umemura, 1986].

In contrast, transducer designs based on phased arrays can be electronically focussed and steered around the volume to be heated and are more promising for the treatment of tumours deep within the body. Several styles of phased array have been considered for deep tissue hyperthermia, with each style having different capabilities. Concentric-ring arrays [Fjield et al., 1996] and combined concentric-ring sector-vortex arrays [Cain and Umemura, 1986] provide the ability to move the focal region along the central axis of the transducer and are able to produce a focal region with an annular geometry suitable for optimal heating of a region of tissue, but are unable to create a focus steered away from the central axis of the array. In contrast, sparse arrays of discrete elements afford maximum flexibility in terms of steering the beam in 3 dimensions and can be used to synthesise complex focal shapes [Goss et al., 1996; Daum and Hynynen, 1999; Gavrilov and Hand, 2000].

Many of the proposed array designs have an overall geometry based on a hemispherical shell [Daum and Hynynen, 1999; Fjield et al., 1996; Goss et al., 1996], which helps produce an inherently focussed beam. However, a transducer with all the elements in a plane would be more appropriate for use on many parts of the body (e.g. the lower abdomen). The key advantages of planar arrays are that they allow for a relatively straightforward construction, and that they may allow closer placement of the transducer to the surface of the patient than is possible with a curved array.

The majority of reported sparse arrays for deep tissue application are intended

for HIFU (such as those by Goss et al. [1996] and Gavrilov and Hand [2000]), and there is a lack of designs aimed at mild hyperthermic applications. However, the requirements of a device for mild hyperthermia are similar to those for HIFU, particularly the requirement for adequate control of the focal region.

The work reported by workers such as Goss et al. [1996]; Daum and Hynynen [1999]; Gavrilov and Hand [2000] has considered many of the design aspects of extra-corporeal phased arrays. For example, they have demonstrated the benefits of a random distribution of elements over regular patterns, especially in the suppression of grating lobes, and have considered the steering ability of their arrays. However, several aspects of the behaviour of arrays are not well understood, such as the relationships between the overall array geometry and the field characteristics, and between the element geometry and the field characteristics. These characteristics need to be fully understood before such an approach can be considered for use in the clinical environment. Within the present work the underlying principles of phased array behaviour have been examined using simulation, and the results of this analysis are described in chapter 3.

- Intra-cavitary devices:

  Numerous workers have reported on the design and characterisation of intra-cavitary ultrasound transducers, such as devices for rectal and vaginal applications. There are two principal differences between these devices and the extra-corporeal devices: Clearly, the physical dimensions of the intra-cavitary devices are limited by the nature of the application, and so intra-cavitary devices are generally smaller than extra-corporeal devices; and intra-cavitary devices are generally targeted at regions closer to the transducer than typical target depths for extra-corporeal devices. Despite these two differences, intra-cavitary devices follow the same design principles as extra-corporeal transducers and so a brief discussion of a few devices of interest in the literature is worthwhile.

Although mechanical movement of an intra-cavitary device is limited, systems where a single element transducer is moved mechanically have been reported for HIFU applications [Sanghvi et al., 1996]. However, many intra-cavitary arrays are based on phased arrays rather than single elements to allow control over the pattern of the heat delivery with minimal mechanical movement of the device. Saleh and Smith [2004] described such an array designed for HIFU treatment of the prostate, where the maximum required focal depth was 40 mm. Their array was constructed from a 20 mm × 20 mm planar slab of PZT-8, diced into an 8×8 grid of rectangular elements. The size of the elements decreased with distance from the centre of the array, from 3 mm in the centre to 2 mm at the edge. This tapering of the element size towards the edge of the array was to minimise the intensities in the grating lobes by reducing the periodicity of the array. In addition to impacting on the grating lobes, the size of the elements in any array will also have an impact on the characteristics (such as intensity and geometry) of the focal region produced by the array. However, the relationships between the element size and these characteristics is not clear.

It is common for intra-cavitary arrays to incorporate a water-cooled bolus surrounding the applicator to prevent overheating of the tissue directly in front of the ultrasound source. For example, applicators designed for hyperthermia or ablation of the prostate (such as those reported by [Smith et al., 2001] and Sanghvi et al. [1996]) may include such a cooling layer to prevent damage to the rectum during treatment.

- Interstitial devices:

  As well as the non-invasive ultrasonic devices mentioned already, interstitial devices have been reported which may be inserted directly into tissue. While these devices are invasive, they provide good control of the heat localisation and minimise the heating of healthy tissue which would lie between other non-invasive ultrasound transducers and the target region [Nau et al., 2000].

As with extra-corporeal and intra-cavitary devices, the use of external cooling layers in conjunction with interstitial devices has been investigated to reduce the heating of the tissue in contact with the applicator and thereby increase the penetration of the heat in the radial direction [Nau et al., 2000]. Other cooling systems have also been described, including routing the water coolant through the internal core of the applicator rather than around the outside in order to cool the piezoelectric device itself rather than the tissue [Deardorff and Diederich, 2000].

In summary, much research has been carried out on the development of ultrasound devices for hyperthermic applications, but as yet no device is in clinical use for localised mild hyperthermia of deep tissue. In addition, the principles behind the design of a suitable array are not well defined in several aspects, particularly with regard to the relationship between the dimensions and geometry of a phased array and the characteristics of the field produced by the array.

1.4 Objectives of the present work

Reviews by Falk and Issels [2001] and Wust et al. [2002] summarise the results of numerous clinical trials and conclude that hyperthermia as an adjunct to other treatment modes can be of benefit. However, Wust et al. [2002] also notes that improvements in the locoregional control of the heating are necessary to allow the full potential of hyperthermic treatments to be evaluated. The present work is aimed towards this need, by considering the development of an ultrasound phased array suitable for deep tissue mild hyperthermia applications.

While a number of surface and intra-cavitary ultrasound systems for mild hyperthermia are currently in clinical use, ultrasound systems for localised and controlled hyperthermia of solid tumours deep within the body are not. The present work therefore examines the problem of constructing a multi-element ultrasound transducer suitable for producing localised hyperthermia deep within the body.

The focus of this work was to establish the physical principles for a planar

phased array transducer that can be electronically focussed and steered, and to produce a physical array to verify these design principles in an experimental context.

To guide the design of the physical array a hypothetical tumour was considered, with the aim being to produce an array capable of creating a focal region within the tumour. This tumour was considered to be centred at a depth between 60 and 100 mm, typical of the depths required for deep tissue hyperthermia, and to be solid and spherical in shape, with a diameter of 40 mm.

To allow comparison between the simulations and the physical array, methods for the characterisation of the array were required. This called for the construction of equipment suitable for experimental measurement of the ultrasonic field produced by an array, and the development of suitable techniques for comparison of the experimental data to simulation.

A further objective was to investigate the differences between the simulated and measured performance of the array. This was achieved using a sensitivity analysis, which involved the use of simulation to investigate the influence of various parameters in the construction and operation of the array, so as to provide an understanding of which parameters in the construction and operation of the array influence the field produced by the array.

The final objective was to look at the feasibility of *in-vivo* use of an array based on the same design scheme as that developed within the simulation work and tested in the experimental measurements. This required predictions to be made of the focal intensity that could be achieved for a practical array, and the development of an array design suitable for clinical use.

Chapter 2

Background theory

As described in section 1.4, the present work is aimed towards the development of an ultrasound phased array suitable for deep tissue mild hyperthermia applications. It will be useful to set out the background theory behind certain aspects that are relevant for the simulation and experimental work on phased arrays described in later chapters. In particular, the following topics will be described briefly: the mechanism by which an ultrasound field may be generated; the structure of the field produced by single and multiple ultrasonic sources; and the effects of attenuation and non-linear propagation within the medium.

2.1 The generation of ultrasound via the piezoelectric effect

The most common ultrasound generation mechanism for medical purposes involves the use of piezoelectric materials. These materials, first discovered by Curie and Curie [1880], develop an electrical potential across the material upon the application of stress. The effect is reversible, and so the application of an electrical potential to a piezoelectric material produces a mechanical stress, resulting in a deformation of the material. Application of an alternating electrical potential produces a periodic stress, causing the material to vibrate. When the material is in contact with a medium, this vibration acts as the source of an acoustic wave.

While a variety of different piezoelectric materials exist, ultrasonic applications typically make use of lead zirconate titanate ($Pb(Zr,Ti)O_3$), a ceramic more

commonly known as PZT. The properties of PZT and the processes involved in its manufacture are described by Haertling [1999]. Different grades of PZT can be formed by fine-tuning the manufacturing process or via the addition of various dopants [Berlincourt, 1992; Haertling, 1999], allowing the characteristics of the PZT to be tailored to suit a particular application.

The key parameters that are used to quantify the properties of piezoelectric materials are as follows:

- $\boldsymbol{d_{33}}$: The d constant is the ratio of the strain to the applied electric field, and has units of mV^{-1} (or equivalently CN^{-1}). The subscripts define the directions of the strain and the applied field. In this case, the subscript '33' indicates that both the strain and electric field are in the thickness direction.

- $\boldsymbol{k_3^T}$: k_3^T is the relative permittivity of the dielectric. The superscript indicates the conditions under which the parameter has been measured, since k is greater for an unstressed, free element than for one which is physically clamped. In this case the superscript 'T' indicates that k has been measured with the element in a mechanically unstressed condition. The subscript indicates the direction, with the '3' here indicating the thickness direction. The capacitance C of an element can be calculated from k_3^T using equation 2.1, where ε_0 is the permittivity of free space, L is the thickness of the element and A is the element's surface area.

$$C = \frac{k_3^T \varepsilon_0 A}{L} \tag{2.1}$$

- $\boldsymbol{f_r}$: The resonant frequencies f_r of a free piezoelectric element are defined by its thickness L according to equation 2.2, where n is an integer and c is the speed of sound in the piezoelectric material. The fundamental vibrational mode occurs when $n = 1$, in which case the thickness of the element is equal to half the ultrasonic wavelength. Equation 2.2 relies on the assumption that the element vibrates with a piston-like motion, an assumption which is also typically made when considering the ultrasonic field produced by a vibrating

element (section 2.2).

$$f_r = \frac{(2n-1)c}{2L} \tag{2.2}$$

- $\boldsymbol{T_C}$: A PZT element is formed from its powdered constituents by heating under pressure to form a polycrystalline ceramic. At the time it is formed, the ceramic has no intrinsic piezoelectric properties. An additional processing step is required to produce these properties. Electrodes are added to two faces of the element and an electric potential is applied across these electrodes while the PZT is heated beyond its Curie temperature, T_C. Above this temperature, the electric dipoles in the PZT are able to align with the electric field, polarising the material. Cooling the PZT element to below T_C while maintaining the electric potential ensures that the polarisation is fixed, and the ceramic is now a piezoceramic. T_C therefore serves as the maximum allowed operating temperature of a piezoelectric ceramic, since at temperatures above T_C the material loses its polarisation, and hence its piezoelectric characteristics.

2.2 The structure of the field produced by a single piston radiator

The case of a vibrating piston located within an infinite baffle is considered in many acoustic textbooks, such as those by Ford [1970], Hall [1987] and Hill et al. [2004a], and is a useful concept since a single circular element is a commonly used source of ultrasound. A piston radiator can be thought of as one where all points on the surface of the disc vibrate at the same phase and with the same amplitude. If the face of the piston is assumed to undergo simple harmonic motion, then the surface velocity u at time t is given by equation 2.3, where u_0 is the surface velocity amplitude and ω is the angular frequency of vibration.

$$u(t) = u_0 \mathrm{e}^{\mathrm{i}\omega t} \tag{2.3}$$

The motion of the piston's surface creates a pressure wave in the medium, with regions of compression and rarefaction propagating away from the disc surface.

The pressure amplitude p_0 at the surface can be related to the velocity amplitude u_0 by equation 2.4, where ρ_0 is the unperturbed density of the medium.

$$p_0 = \rho_0 c u_0 \tag{2.4}$$

Assuming that the piston has a diameter much less than the ultrasonic wavelength in the medium, a hemispherical pressure wave results. If the diameter of the piston is comparable to or larger than the ultrasonic wavelength, then one can consider its surface as being composed of a large number of elemental areas. The elemental pressure δp at a time t and a distance r from the elemental area δS is then given by equation 2.5, where k is the wavenumber.

$$\delta p(r,t) = \frac{p_0}{r} \mathrm{e}^{\mathrm{i}(\omega t - kr)} \delta S \tag{2.5}$$

The total pressure at a field point $\vec{r}$ in the medium due to the vibration of the entire surface S can be found using the Rayleigh integral [Strutt, 1896; Mast, 2005], where R is the distance from the field point $\vec{r}$ to the elemental area dS on the piston surface.

$$p(\vec{r},t) = -\frac{ik}{2\pi} p_0 \int \frac{\mathrm{e}^{\mathrm{i}(kR-\omega t)}}{R} dS \tag{2.6}$$

Finding a general solution of equation 2.6 for any source geometry is not straightforward and various approaches (such as numerical integration or expansion of the integral to form a series from which specific solutions may then be computed) may be applied depending on the purpose of the work. Indeed, for the simple case of a baffled, circular source of radius a, analytic solutions exist only for the axial field and for the asymptotic far-field [Mast, 2005].

Taking the case of the axial field first, the pressure amplitude p along the central axis of symmetry (which shall be called the z-axis) is given by:

$$p(z) = 2\rho_0 c u_0 \left| \sin\left[\frac{kz}{2} \left(\sqrt{1 + \left(\frac{a}{z}\right)^2} - 1 \right) \right] \right| \tag{2.7}$$

From equation 2.7 it can be observed that there are number of maxima and minima along the central axis. These maxima and minima occur according to equation 2.8 where m is an integer.

$$\frac{kz}{2}\left(\sqrt{1+\left(\frac{a}{z}\right)^2}-1\right)=\frac{m\pi}{2} \tag{2.8}$$

The axial maxima occur when m is odd, while minima occur when m is even. The positions of these axial maxima and minima can be found by rearranging equation 2.8 as shown:

$$z=\frac{a^2}{m\lambda}+\frac{m\lambda}{4} \tag{2.9}$$

When $m = 1$ the position of the last axial maximum (denoted z_{LAM}) is given. Where $a \gg \lambda$, this is generally expressed as:

$$z_{LAM}=\frac{a^2}{\lambda} \tag{2.10}$$

The position of the last axial maximum is a convenient boundary marker between the near and far field regions. At distances less than z_{LAM} the field is composed of numerous pressure amplitude maxima and minima, while at distances greater than z_{LAM} the pressure amplitude along the central axis is inversely proportional to z.

The second analytic solution for the pressure field produced by a baffled, circular, piston vibrator is for the asymptotic far-field ($r \gg z_{LAM}$), giving the pressure at an angle θ away from the axis as shown in equation 2.11, where J_1 is a Bessel function of the first kind.

$$p(r,\theta)\rightarrow \mathrm{i}ka^2\frac{J_1(ka\sin\theta)}{ka\sin\theta}\frac{\mathrm{e}^{\mathrm{i}kr}}{r} \tag{2.11}$$

In summary, analytical solutions for the field generated by an ultrasound source only exist for certain source geometries, such as that of a circular, piston radiator, where the axial field and the asymptotic far field are given by equations 2.7 and 2.11 respectively. General analytical solutions of the ultrasound field outside

these special cases are not available. Within the present work a method of computing the complete field was required, and since there is no analytic solution which is able to provide this, another method of computing the field was required. In chapter 3 the method used in the present work will be described, and the application of this method in the design of an array suitable for heating of deep tissue will also be discussed.

2.3 The structure of the field produced by a large number of sources

A phased array can be used to create a focussed field by applying drive signals of the appropriate phase to each element in the array. For the simple case of a homogeneous medium the required phases can be calculated geometrically, in order that ultrasonic waves originating from all the elements result interfere constructively at the required focal position. It is also possible to control the phases such that multiple foci are created simultaneously [Ebbini and Cain, 1989], but within the present work only the case of a single focal region will be considered.

For any regular array of identical sources each producing waves in phase, it is inevitable that grating lobes will exist in the far-field. The position and intensity of these grating lobes is dependent on the wavelength and on the geometry of the array of sources, and texts such as Pain [1999] and Main [1993] describe the physics behind this phenomenon in detail.

To illustrate the principles behind the behaviour of an array of sources it will be useful to consider the case of a linear diffraction grating, which is a regular 1-D array of identical in-phase sources. In the far-field of such an array, the pressure P in the plane perpendicular to the direction of propagation is given by equation 2.12, where $P(x = 0)$ is the pressure amplitude on the central axis of the array and x is the distance away from the central axis in the direction perpendicular to the direction of propagation. Terms D_1 and D_2 are defined as shown in equations 2.13 and 2.14, where k is the wavenumber, z is the distance from the array, N is the

number of elements in the array, d is the inter-element pitch and a is the element radius. It can be seen from these equations that D_1 is related to the parameters which define the geometry of the array (N,d) while D_2 is related to the dimensions of the sources within the array (a).

$$P(x) = P(x = 0)D_1D_2 \tag{2.12}$$

$$D_1 = \left| \frac{\sin\left(\frac{Nkdx}{2z}\right)}{\sin\left(\frac{kdx}{2z}\right)} \right| \tag{2.13}$$

$$D_2 = \left| \text{sinc}\left(\frac{kax}{z}\right) \right| \tag{2.14}$$

Figure 2.1a illustrates the typical form of D_1, D_2 and the total pressure $P(x)$ for a linear diffraction grating. A number of observations can be drawn from this figure:

1. D_1 is composed of a repeating pattern which contains principal and subsidiary maxima. Decreasing the inter-element pitch d increases the distance between each principal maxima, while increasing the number of elements in the array N reduces the width of each maxima and increases the number of subsidiary maxima (which is equal to N-2). In the present work, the principal maxima are referred to as the grating lobes of the array.
2. In contrast to D_1, the function D_2 has the form of a sinc function, and increasing the element radius a reduces the width of the sinc function.
3. $P(x)$ is given by the product of D_1 and D_2.

The position of the central pressure maximum may be steered laterally by appropriate phasing of the elements in the linear array. The effect of steering is that the function D_1 is shifted laterally, while D_2 remains unchanged. This is shown in figure 2.1b where the array has been steered by approximately 2° to the right, equivalent to a lateral shift of 3 mm at a depth of 80 mm. D_2 can be thought of as an envelope around function D_1, with the result that the central pressure maxima

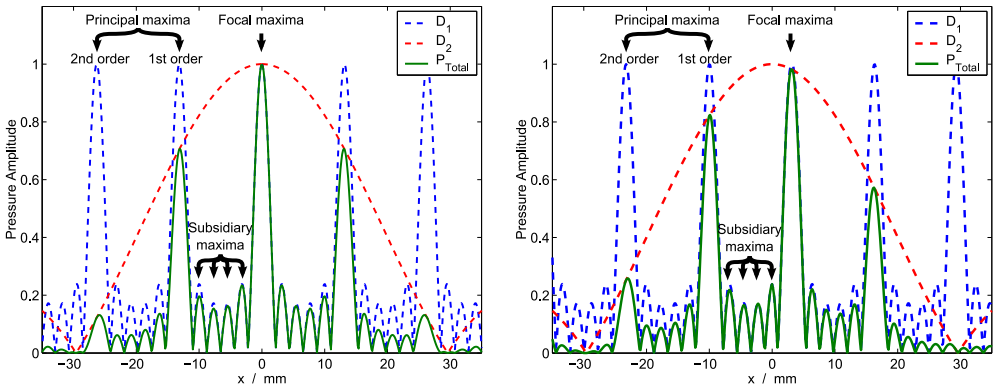

Figure 2.1: (a) Plot showing the Fraunhofer grating lobes produced by a 1-D linear array containing 6 wave sources each with a width of 4 mm (= 2a) and a pitch of 9 mm (=d). The pressure amplitude at a depth z = 80 mm and perpendicular to the direction of propagation is shown as computed using equations 2.13, 2.14 and 2.12. (b) Plot showing the grating lobes produced by the same array when a steering angle of 2° is applied.

for a steered array is reduced in amplitude. All the other principal maxima are also shifted in the same direction, and therefore the amplitude of the first order principal maximum on the left of the focal maxima is increased.

In summary, consideration of equations 2.12, 2.13 and 2.14 can provide useful insight into the behaviour of phased arrays. For example, Wooh and Shi [1998] stated that the element size should be maximised in order to minimise the intensity of the grating lobes, and this can be confirmed from the equations: Increasing the element radius a reduces the width of the sinc function D_2, and since P_x can be found by using D_2 as an envelope around function D_1, reducing the width of D_2 will reduce the grating lobe intensity. However, other effects that would result from increasing the element size can also be observed: Figure 2.1b illustrates that as the central maxima is steered laterally its amplitude decreases, following the D_2 envelope. Increasing the element radius will therefore limit the off-axis steering ability of an array.

2.4 Attenuation and speed of sound within the medium

So far the consideration of the ultrasonic field from a single source or a number of sources has been limited to a non-attenuating medium. The effects of attenuation must be added to the consideration since energy carried by the ultrasound wave must be absorbed by the medium in order to produce heating.

The earlier discussion in this chapter has considered ultrasound as a pressure wave propagating within a medium. Equation 2.15 relates this pressure wave to the energy carried by the wave, where I is the intensity and p_{RMS} is the root mean square (RMS) of the pressure wave propagating within a medium of density ρ and speed of sound c.

$$I = \frac{p_{RMS}^2}{\rho c} \tag{2.15}$$

The intensity of an ultrasound wave propagating within any medium decreases with distance due to attenuation of the wave. There are a number of mechanisms which contribute to the overall attenuation, but the most dominant of these in tissue media is absorption, which results in heating of the tissue.

For a plane wave within a homogeneous medium the intensity decreases exponentially, as described by equation 2.16, where I_0 represents the intensity at the source, z the depth within the medium, and μ the intensity attenuation coefficient.

$$I(z) = I_0 \mathrm{e}^{-\mu z} \tag{2.16}$$

The attenuation coefficient can also be quoted in the form of the pressure amplitude attenuation coefficient α. For a plane wave, equation 2.17 describes how the pressure amplitude decreases with distance from the source due to attenuation within a homogeneous medium, where p_0 is the pressure amplitude at the source, $p(z)$ is the pressure amplitude at a distance z from the source and α is the pressure amplitude attenuation coefficient.

$$\frac{p(z)}{p_0} \propto \mathrm{e}^{-\alpha z} \tag{2.17}$$

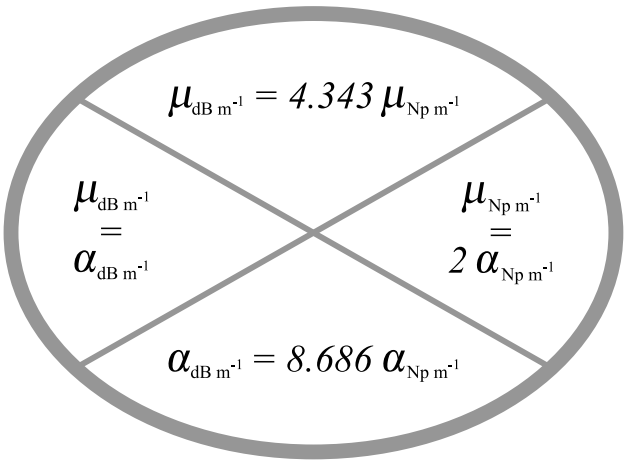

Figure 2.2: Relationships between the intensity (μ) and pressure amplitude (α) attenuation coefficients.

Care must be taken when using the attenuation coefficient to distinguish between the intensity and pressure amplitude coefficients. In addition, two different units of measure may be used when quoting an attenuation coefficient ($\mathrm{Np\,m^{-1}}$ and $\mathrm{dB\,m^{-1}}$), and so care must also be taken to ensure that the appropriate units are used in any calculations. Figure 2.2 illustrates the relationships that exist between the intensity (μ) and pressure amplitude (α) attenuation coefficients, as well as illustrating the relationship between the measurement units of $\mathrm{Np\,m^{-1}}$ and $\mathrm{dB\,m^{-1}}$. For simplicity, attenuation coefficients will be quoted in units of $\mathrm{dB\,m^{-1}}$ throughout the present work, since for this choice of units the intensity and pressure coefficients are numerically the same (i.e. $\mu = \alpha$).

For biological, soft tissues, the attenuation coefficient increases approximately linearly with frequency [Wells, 1975]. Consequently, higher ultrasonic frequencies tend to be more suitable for heating of superficial tissue, since the high absorption coefficient reduces the penetration depth of the ultrasound. As an example, Mitsumori et al. [1996] noted in their clinical trial of an ultrasound hyperthermia system that they based their choice of ultrasonic frequency on the depth of the tumour to be treated, ranging from a 1 MHz applicator for tumours located at depths greater than 6 cm, to a 3 MHz applicator for tumours at depths of less than 0.5 cm.

As described in section 1.4, the work described within this thesis is aimed towards the development of a system suitable for heating tumours located at depths of 6 to 10 cm, and frequency of 1 MHz was therefore used throughout the experimental work.

Most of the simulation work and all of the experimental measurements performed within this project studied ultrasonic fields in a medium of water, for which the intensity attenuation coefficient μ is 0.0022 $\mathrm{dB\,cm^{-1}}$ at 1 MHz and 20 °C [Krautkrämer and Krautkrämer, 1990]. The absorption coefficient of soft tissue at 1 MHz is much greater than that of water, ranging from approximately 0.3 to 1.0 $\mathrm{dB\,cm^{-1}}$ at 1 MHz [Wells, 1975] depending on the type of tissue. Whenever tissue has been considered within the present work, an attenuation coefficient of 0.5 $\mathrm{dB\,cm^{-1}}$ [Wang et al., 1999; Damianou et al., 1997] has been used.

According to Kaye and Laby [1995], the speed of sound in water is approximately 1480 $\mathrm{ms^{-1}}$ at 20°C, and this value has been used throughout the present work. Within tissue the speed of sound is similar, ranging from 1520-1590 $\mathrm{ms^{-1}}$ depending on the temperature and the tissue type [Nasoni et al., 1980]. This similarity enables the characterisation of the field produced by an array to be performed within a water tank rather than tissue, since the similar speeds of sound results in similar field geometries within the two media.

2.5 Linearity of the medium

Non-linear wave propagation is described in texts such as those by Mason [1965], Duck et al. [1998a], Duck [2002] and Hill et al. [2004b]. It can have an important impact on focussed ultrasound fields since its effects are greater for large amplitude waves.

Within a homogeneous medium, the degree of non-linearity can be characterised by the parameter β, which relates the particle velocity v_p at a particular point on the waveform to the wave speed c and the particle velocity u_p, as shown in equation 2.18. (Typical values of β are 3.5 for water [Mason, 1965; Duck, 2002] and

4-6 for tissue [Duck et al., 1998a].) In regions of compression u_p is positive, and so $v_p > c$, but in regions of rarefaction u_p is negative, and $v_p < c$. Regions of compression therefore travel slightly faster than regions of rarefaction, leading to distortion in the shape of the waveform with increasing distance from the ultrasound source.

$$v_p = c + \beta u_p \tag{2.18}$$

Since the regions of compression travel more quickly than the regions of rarefaction, the pressure gradient (dp/dz) in the region leading the compressions and trailing the rarefactions becomes more negative. In a non-attenuating medium dp/dz will ultimately approach $-\infty$, at which point a shock discontinuity is formed. The distance from the source to the point at which the shock is formed is termed the discontinuity distance, l_d, which is defined by equation 2.19 for a plane wave (where ρ is the unperturbed density of the medium, ω is the angular frequency of the ultrasound and p_0 is the pressure amplitude at the source).

$$l_d = \frac{\rho c^3}{\omega \beta p_0} \tag{2.19}$$

The level of distortion present at any position in the field can be quantified relative to the discontinuity distance l_d through the use of the parameter σ, which is defined according to equation 2.20. By definition, $\sigma = 1$ at the point where the shock discontinuity is first formed, and at greater values of σ the shape of the waveform approaches that of a sawtooth [Hill et al., 2004b].

$$\sigma = \frac{z}{l_d} \tag{2.20}$$

Figure 2.3 illustrates the formation of a shock discontinuity when $\sigma = 1$. The x-axis in this figure represents distance, such that the wave is propagating from left to right. It should be noted that some authors (such as Duck [2002] and Hill et al. [2004b]) follow this designation of the x-axis, while others (such as Bacon [1984] and Hoffelner et al. [2001]) use the x-axis to represent time, with the result that their waveforms are travelling from right to left. Care should therefore be taken when comparing waveforms reported by different authors.

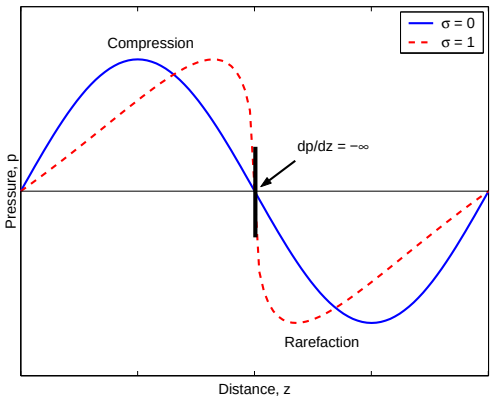

Figure 2.3: Plot showing the effect of a non-linear medium on the pressure waveform: $\sigma = 0$ illustrates a wave with no distortion and $\sigma = 1$ illustrates a wave which has become distorted after propagating for some distance within a non-linear medium, such that a shock discontinuity has begun to form between the regions of compression and rarefaction. The wave is propagating from left to right.

For a focussed field, the calculation of σ must be modified from the plane wave case. For a spherically focussed ultrasound source, σ at the focus can be calculated as shown in equation 2.21 [Bacon, 1984], where p_f is the pressure amplitude at the focus, z_f is the focal distance and G is the pressure amplitude focal gain, defined here by equation 2.22.

$$\sigma = \frac{\omega \beta p_f z_f}{\rho c^3} \left[\frac{ln(G + \sqrt{G^2 - 1})}{\sqrt{G^2 - 1}} \right] \tag{2.21}$$

$$G = \sqrt{\frac{Area_{source}}{Area_{focus}}} \tag{2.22}$$

As can be seen from equations 2.19, 2.20 and 2.21, the effect of a non-linear medium on the shape of the waveform (as quantified by σ) becomes greater with both increasing frequency and increasing pressure amplitude.

To illustrate the potential significance of non-linear propagation, a 1 MHz ultrasound wave with an intensity of 1 Wcm^{-2} in a medium of water can be considered as an example. If the wave is planar, then the discontinuity distance $l_d = 86$ cm, meaning that the effects of non-linear propagation will be small at depths less

than this. However, if the field is focussed by using a concave source of radius 25 mm and radius of curvature of 60 mm, a focal intensity of 1 Wcm^{-2} would correspond to a focal σ value of 1.18, indicating that distortion of the wave may be significant at the focal region.

Non-linear effects are important for hyperthermia applications because distortion of the waveform results in the introduction of higher frequency components to the wave spectrum. Since ultrasonic attenuation increases with increasing frequency (section 2.4), the introduction of these higher frequencies results in increased attenuation, changing the geometry of the field from the linear case. In addition, the effects of non-linear distortion are greater for strongly focussed fields.

While the impact of non-linear propagation on the present work was negligible because of the low intensities involved ($\sim$25 mWcm^{-2}, detailed in section 6.4.1), its impact is likely to be important in future work based on tissue media, partly because $\beta_{tissue} > \beta_{water}$, but primarily because the focal intensities required for hyperthermic applications are much greater, being in the region of 50-300 Wcm^{-2} (section 8.2). A study by Meaney et al. [2000] noted that there are two main ways in which non-linear propagation impacts on HIFU lesions in tissue: [i] The position of the lesion is shifted towards the transducer surface; and [ii] the geometry of the lesion is modified from what Meaney called a 'cigar-shaped' region to a 'tadpole-like' shape, where the maximum width is forward of the lesion centre. Both of these changes are a consequence of the fact that absorption increases with frequency, with the result that energy is deposited in a non-linear medium forward of where it would be deposited in a linear medium. A further HIFU-centred study by Liu et al. [2006] noted that this increased absorption can produce an increase in the rate of heat deposition by up to a factor of two in comparison with that expected under linear conditions.

While these studies of non-linear effects have been focussed on HIFU applications, little work has been reported concerning the impact on mild hyperthermia applications. Although it would be expected that the impact would be less severe than for HIFU, work will be required to quantify and model the effects so that

non-linearity of the medium can be taken into account in the development of a temperature control scheme.

Chapter 3

Ultrasound field simulation

3.1 Introduction

Simulation tools are useful in the design of ultrasound phased arrays as they provide a means of studying the behaviour of arrays which may be impractical or impossible to study experimentally. The impact of various design choices may be investigated quickly without having to build physical arrays for each scenario, providing a useful tool for the optimisation of array designs. Simulation tools can also be useful in provide insight into the operation of phased arrays, and the impact that various environmental factors can have on the field produced by the array.

Simulation also offers the potential of linking different models together. For example, in the context of the present work models of the ultrasound field profile can be linked to thermal models to look at the temperature distributions that can be obtained within particular tissues [Meaney et al., 1998] and at the problem of controlling the thermal dose delivered to the tissue [Arora et al., 2005].

Several techniques exist which enable the operation of ultrasound arrays to be modelled by simulation. Finite element methods, such as those employed by the package PZFlex (Weidlinger Associates, Washington, USA), provide a means of simulating the vibrational behaviour of the materials within an array in terms of the stresses and strains that the material in the array is subject to, as well as modelling the field produced by the array. These methods can provide useful insight into the mechanical behaviour of structures within the transducer (such as the elements and matching layers [Wojcik et al., 1996]), as well as the behaviour of

the field in complex media [Meaney et al., 1998]. However, a detailed knowledge of the structure of the array or medium is necessary to configure these simulations, requiring information about the properties and geometries of the materials and interfaces under investigation.

Simpler methods exist which allow the field produced by a piston-like radiator within a homogeneous medium to be computed numerically [Holm et al., 1998]. While these methods do not provide information about the behaviour of internal structures within the transducer or allow the field to be computed in complex media, they are suitable for the general study of array design and for the simulation of fields within homogeneous media. Such methods are therefore particularly suitable for the present work where the aim is to study the physical principles behind the design of phased arrays, and to provide results which may be compared against experimental fields measured in a water medium. In addition, such numerical simulation methods make it relatively straightforward for the user to make custom modifications to the simulation code.

3.2 Ultrasim

The simulations within the present work were performed using Ultrasim, a Matlab based package for ultrasound wave simulation developed by Vingmed Sound (Horten, Norway), the Department of Physiology and Biomedical Engineering and the Department of Mathematical Sciences of the Norwegian University of Science and Technology (Trondheim, Norway) and the Department of Informatics of the University of Oslo (Oslo, Norway). A brief description of the basic function of Ultrasim will now be presented as well as a description of the custom modifications that were made within the present work. A fuller description of Ultrasim, which includes details on many features not used in the present work, is given by Holm [2001].

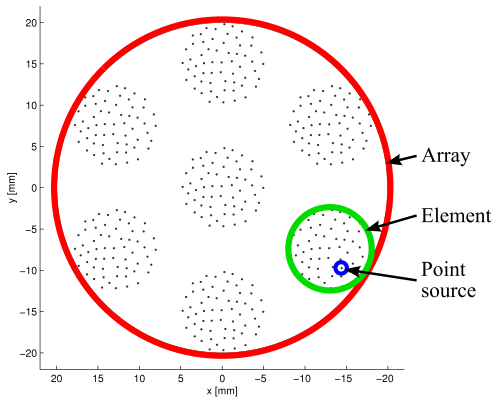

Figure 3.1: Illustration of a typical planar array, as configured by Ultrasim. This array is composed of 7 circular elements arranged in a hexagonal grid, where each element is composed of a number of point sources distributed evenly across its surface. These definitions of the terms 'array', 'element' and 'point source' are used throughout the present work.

3.2.1 Method used for the calculation of the pressure field

The terms array, element and point source will be used to describe the transducer within the simulation work, and the definitions of these are illustrated in figure 3.1.

To calculate the field from a single vibrating element, the method employed by Ultrasim is to solve the Rayleigh integral (equation 2.6). It does so by distributing a number of points across the surface of the element (as shown in figure 3.1), each of which is modelled as the source of a pressure wave of defined phase and amplitude radiating spherically into an infinite linear homogeneous medium. Since the parameters defining the ultrasonic wave and the medium (in particular: the frequency, the speed of sound and the attenuation coefficient) are defined by the user, the pressure contribution from a single point source can be calculated at any position in the field. The total complex pressure at any field position is then given by the sum of the pressure contributions from all the point sources within the element. When simulating the field produced by a single vibrating element Ultrasim assumes that the amplitude and phase of vibration are the same for all point sources which make up the element, which is to say that it assumes each element behaves like an

ideal piston vibrator.

To calculate the field from a phased array composed of a number of elements focussed to a particular location in the medium, the phase shifts for each element necessary to produce the focus at the required position were first calculated. These were found using a geometrical method where, given the distance from the centre of each element to the focus and the speed of sound in the medium, the time of flight required for the wave to travel from the element to the intended focus can be calculated. Using this information, appropriate phase shifts can be applied to each element to ensure that waves originating from each element all arrive at the focus in phase, such that constructive interference occurs. For example, if for some array the time of flight to the focus from element A is 50.0 ms and from element B is 50.2 ms, then the phase of vibration of element B should be 0.2 seconds (which is equivalent to $\sim$1.26 radians for 1 MHz ultrasound) ahead of element A.

It should be emphasised that this method of calculating the phase shifts for focussing of the ultrasound field is, strictly speaking, only suitable for a homogeneous medium. Its use within the present work, where the simulations and experimental measurements are based on a water medium is therefore appropriate. However, some other technique is required for calculation of the phase shifts required for optimal focussing in an inhomogeneous medium. For example, a series of papers by Fink [1992], Wu et al. [1992] and Cassereau and Fink [1992] described the time-reversal technique, where phase shifts are calculated based on an analysis of echoes returned from a reflective surface in the medium. Future work will need to consider the suitability of these and other techniques such as this for the calculation of phase shifts for optimum focussing in inhomogenous tissue media.

The total ultrasound pressure P_{total} produced by a phased array at any location in a homogeneous field could then be computed by summing the pressure contributions from all point sources within all elements of the array as shown in equation 3.1, where N is the total number of point sources in the array, P_n is the pressure amplitude at the surface of the nth point source, α is the pressure attenuation coefficient, k is the wavenumber, x_n is the distance from the nth point source

to the location in the field and ϕ_n is the phase delay for the nth point source. As was the case for a single element, when calculating the field produced by a phased array Ultrasim assumed that each element behaved as an ideal piston, with all point sources within an element having the same amplitude and phase of vibration.

$$P_{total} = \sum_{n=1}^{N} P_n \mathrm{e}^{-\alpha x_n} \mathrm{e}^{\mathrm{i}(kx_n + \phi_n)} \tag{3.1}$$

Using this method, Ultrasim was able to compute the complex pressure at any position in the field at any time. The software was capable of simulating the evolution of the field over time for the case where a transducer is driven by a discrete pulse. However, the present work was aimed at studying the steady state, or continuous wave (CW) case, where the transducer is driven with a continuous sinusoidal drive signal.

3.2.2 Assumptions required by the simulations

The simulation tool required the following assumptions to be made about the medium, all of which were reasonable approximations to the acoustic tank used in the experimental work to verify the results of the simulations:

1. The medium was infinite.
2. The medium was homogeneous.
3. The medium was non-scattering.
4. The medium was linear.

In addition, the following assumptions were made about the behaviour of the elements. In chapter 7 the effect of several of these assumptions will be considered as part of the investigation into the discrepancies between the simulated and experimentally measured fields for the fifteen element array described in chapter 6.

1. All point sources within a single element were assumed to vibrate with the same phase and amplitude, which is to say that the vibration of each element was a piston-like motion.

2. It was assumed that the oscillation of an element was sinusoidal and continuous.
3. In an array of elements, the phase of the drive signal was precisely controlled, with no quantisation.
4. The behaviour of each element was assumed to be independent of all other elements. (I.e. there was no crosstalk between elements in the array.)

3.2.3 Modifications to Ultrasim

A customised version of Ultrasim was used throughout this work, in which some extra functionality was added to the simulation software which allowed several additional parameters to be included in the simulations. The modifications that were used generally throughout the simulation work will be described here, while those that are unique to the sensitivity analysis will be described in detail in section 7.

1. Definition of arbitrarily configured arrays:

   Ultrasim provides a range of transducer configurations that can be selected by the user: Single element transducers; phased arrays composed of rectangular grids of elements; and concentric ring phased arrays can all be defined. The number of elements and the element dimensions are configurable, as is the curvature of the transducer and the excitation frequency. However, there are limitations to the arrays that Ultrasim can configure as standard. Design of an array with no restrictions on element shape, size and placement is not possible. In addition, all array configurations provided by Ultrasim are composed of elements which butt against each other, with no inactive regions separating the elements.

   Modifications to Ultrasim were required to allow arbitrarily configured arrays to be defined, where the number, shape and layout pattern of the elements were not subject to these default limitations. The main custom array configurations used in the work reported here were for the idealised arrays considered in section 3.4 and the planar arrays of circular elements considered throughout

the rest of the work. Scripts were written to allow the coordinates of the elements and point sources within these arrays to be defined and imported into Ultrasim.

2. Exporting simulation results:

   While there were various plotting tools available in Matlab for reviewing the results of a simulation, there was no provision for exporting the results for external analysis or for comparison to other datasets. A custom script was therefore required to enable the results to be exported in a suitable format.

   The first step was to calculate the pressure amplitude at each position in the field from the complex pressures computed by Ultrasim, since it is the amplitude that is physically meaningful and can be compared to experimental pressure measurements. Following this, the data was exporting using tab delimited ASCII files to ensure maximum portability.

   The majority of the simulations performed in the present work were of the field within a 2-D plane, since the symmetry of the field produced by single elements and phased arrays made full 3-D simulations unnecessary for most situations. For 2-D simulations, the simulated pressures are held within an $m \times n$ Matlab array, with each entry in the array corresponding to a particular location in the $m \times n$ plane of simulation. To export the results, four ASCII files were used: three files to record the x, y and z coordinates defining the plane, and one file to record the pressure amplitudes at each of the $m \times n$ locations in the plane.

   On a small number of occasions 3-D simulations were performed (such as in section 3.5.4). For these a similar method was used to export the results, since the $m \times n \times o$ locations within a simulated 3-D volume can be regarded as multiple 2-D simulation planes. The x, y and z coordinates defining the volume were exported within three ASCII files, and multiple ASCII files were used to export the simulated pressure amplitudes, using one ASCII file per 2-D plane.

3. Automated full-factorial simulations:

   The unmodified Ultrasim package allowed the user to configure the array, the excitation conditions and the medium for a single simulation. Using Ultrasim to study the effects of several factors through a large number of simulations would be very repetitive and impractical for the user. Matlab scripts were written to allow the user to define a range of values for several factors, so that simulations could be run automatically and the results saved for analysis.

Several other modifications were made to Ultrasim specific to the sensitivity analysis to allow additional effects to be simulated, such as non piston-like motion of the element surface, inter-element crosstalk and quantisation of phase delays. These modifications will be discussed in section 7.

3.3 Simulation objectives

Part of the difficulty in designing phased arrays is that there are many design parameters which define the array, such as the overall array radius, the array radius of curvature, the geometry of the element layout, and the size and shape of each element. In addition, factors such as the ultrasonic frequency and the focal depth must be considered. While other workers have proposed array designs for various applications (examples of which are given in section 1.3.2), there are several aspects in which the general principles of array design are not well established.

For example, while generalised equations exist which relate the geometry of the focal region to the geometry of the transducer for a single concave ultrasound source, no similar equations have been reported to relate the geometry of the focal region to the geometry of a phased array. Similarly, other aspects of the design of phased arrays are not well established. For example, while workers such as Gavrilov and Hand [2000] have placed an upper limit (of $\sim 5\lambda$) on the size of element that should be used in an array, their suggested upper limit is only applicable to arrays with a similar geometry and focal depth to the specific array considered in their work. A more generalised understanding of the impact of element size would be

desirable.

Within the present work a new approach has been used to establish the general design principles for ultrasound phased arrays. The problem has been separated into two parts, by separating the parameters that define all real arrays into two groups:

1. The fundamental array parameters related to the dimensions of the array itself, including the overall array radius and radius of curvature.
2. The secondary parameters related to the individual elements within that array, including the size and shape of each element and the geometry of the element layout.

Simulations investigating these two sets of parameters separately will now be described in turn: The fundamental array parameters alone will be considered through simulations of an idealised array; and following this the secondary array parameters will be considered through simulations of practical arrays.

3.4 Simulation of an idealised transducer

An idealised array may be defined as one consisting of a very large (theoretically infinite) number of elements, each infinitesimally small. This was approximated in the simulation by distributing point sources evenly over a concave surface of defined radius of curvature, and within a defined array radius. In this context a planar array was considered a special case of a concave array with an infinite radius of curvature.

The time required to compute a simulated field was proportional to the number of point sources used to define the array, and so using very high point source densities was undesirable. However, if too few point sources were used to define the array then the simulated pressure amplitudes would be dependent on the positioning of the point sources, particularly in the region of the field close to the array surface. Simulations of a plane circular single element were performed to establish the minimum point source density that should be used. The results of these indicated that for point source densities greater than approximately 10 points

per mm^2 the pressure amplitudes in the simulated fields were independent of the exact positioning of the individual point sources, and so a minimum point source density of 10 points per mm^2 was used throughout the simulations.

Such an idealised transducer could be used to simulate four situations: a planar single element, a spherically curved single element, a planar phased array, and a spherically curved phased array. Defining a planar transducer required the radius of curvature to be set equal to infinity. To simulate an idealised single element all point sources were run in phase, while for an idealised phased array an appropriate phase shift was applied to each point source in the array. A uniform amplitude of vibration was applied for all point sources in both the idealised single element and idealised phased array simulations.

3.4.1 Simulations of an idealised single element

Figure 3.2 illustrates the typical simulated field for a plane circular single element, with the field being axisymmetric about the central axis of the element. The -3 dB intensity contour used to define the length and width of the central high intensity region at the near/far field transition is shown in figure 3.2, and throughout the present work the -3 dB contour has also been used to define the focal dimensions for focussed fields. The purpose of the simulations was to understand how the focussing of a phased array changes the focal dimensions. For a focussed field (from either a spherically curved element or a phased array), the geometry of the field essentially follows the same general form as figure 3.2, but with the last axial maximum shifted towards the transducer surface due to the focussing.

Equations describing the geometry of the field produced by a single element (both planar and spherically curved) are well known [Lucas and Muir, 1982; Duck et al., 1998b] and are shown in table 3.1. Simulations on single element transducers have been performed which have confirmed these relationships for the planar case, and for the spherically curved case where the amplitude gain G is greater than 9. For such spherically curved elements, G is defined by equation 3.2 [Lucas and Muir, 1982], where a is the element radius, λ is the ultrasonic wavelength in the medium,

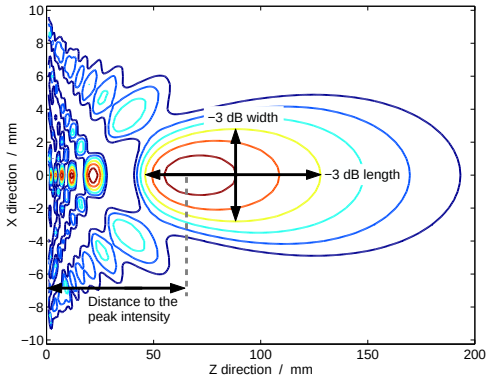

Figure 3.2: Simulated field of a plane circular single element of radius a = 10 mm, in a non-attenuating medium where λ = 1.48 mm. The contours indicate regions of intensity 1,2,3,4,5 and 6 dB less than the peak intensity at the near/far field transition. Note that the maximum width of the -3 dB region occurs beyond the position of the peak intensity.

Table 3.1: Equations describing the geometry of the focal region for an idealised single element, where λ is the ultrasound wavelength, a is the array radius, R is the array radius of curvature, and R is the element radius of curvature.

Focal geometry	Plane circular single element	Spherically curved single element
Axial position of peak =	$\frac{a^2}{\lambda}$	$R - 12(\frac{\lambda^2 R^3}{\pi^2 a^4}) + O[\frac{\lambda^4 R^5}{\pi^4 a^8}]$
-3 dB length =	$1.35\,\frac{a^2}{\lambda}$	$0.89\,\lambda(\frac{R}{R-\sqrt{R^2-a^2}})$
-3 dB width =	$0.61\,a$	$0.52\,\lambda(\frac{R}{a})$

and R is the radius of curvature of the element.

$$G = \frac{\pi a^2}{\lambda R} \tag{3.2}$$

3.4.2 Simulations of an idealised phased array

For the design of a real array models describing the geometry of the field produced by an idealised phased array are required which, to the best of the author's knowledge, have not been reported previously. Simulations were performed to look at the relationship between the field geometry and the transducer radius, transducer curvature, phase-defined focal depth and ultrasound wavelength.

Table 3.2: Equations describing the geometry of the focal region for an idealised phased array, where λ is the ultrasound wavelength, a is the array radius, R is the array radius of curvature, and f is the focal depth of phased array.

Focal geometry	Plane circular phased array	Spherically curved phased array
Axial position of peak =	$f - 12(\frac{\lambda^2 f^3}{\pi^2 a^4}) + O[\frac{\lambda^4 f^5}{\pi^4 a^8}]$	$f - 12(\frac{\lambda^2 f^3}{\pi^2 a^4}) + O[\frac{\lambda^4 f^5}{\pi^4 a^8}]$
-3 dB length =	$2.88\,\lambda(\frac{f}{a})^{\frac{3}{2}}$	$1.47\,\lambda(\frac{R}{R-\sqrt{R^2-a^2}})^{\frac{1}{4}}(\frac{f}{a})^{\frac{3}{2}}$
-3 dB width =	$0.66\,\lambda(\frac{f}{a})^{\frac{3}{4}}$	$0.49\,\lambda(\frac{R}{a})^{\frac{1}{4}}(\frac{f}{a})^{\frac{3}{4}}$

By similarity with equation 3.2, a new expression for the amplitude gain of an idealised phased array G_p has been defined, as shown in equation 3.3, where f is the focal depth of the phased array.

$$G_p = \frac{\pi a^2}{\lambda f} \tag{3.3}$$

Using least squares curve fitting, equations were obtained from the simulation results to describe the field geometry for values of G_p greater than 9, and are given in table 3.2. While only the equations for an idealised plane circular phased array are of interest for the array design in the current work as discussed in section 1.4, the equations for the idealised spherically curved phased array have been included in table 3.2 for completeness.

Figure 3.3 compares the models given in tables 3.1 and 3.2 for to the simulation results for both an idealised spherically curved single element and an idealised plane circular phased array, in terms of the focal position and the -3 dB length and width of the focal region. From figures 3.3b,d,f it can be seen that the predicted and simulated results for an idealised planar phased array become significantly different for a small transducer radius coupled with a long focal distance, corresponding to values of $G_p \lesssim 9$.

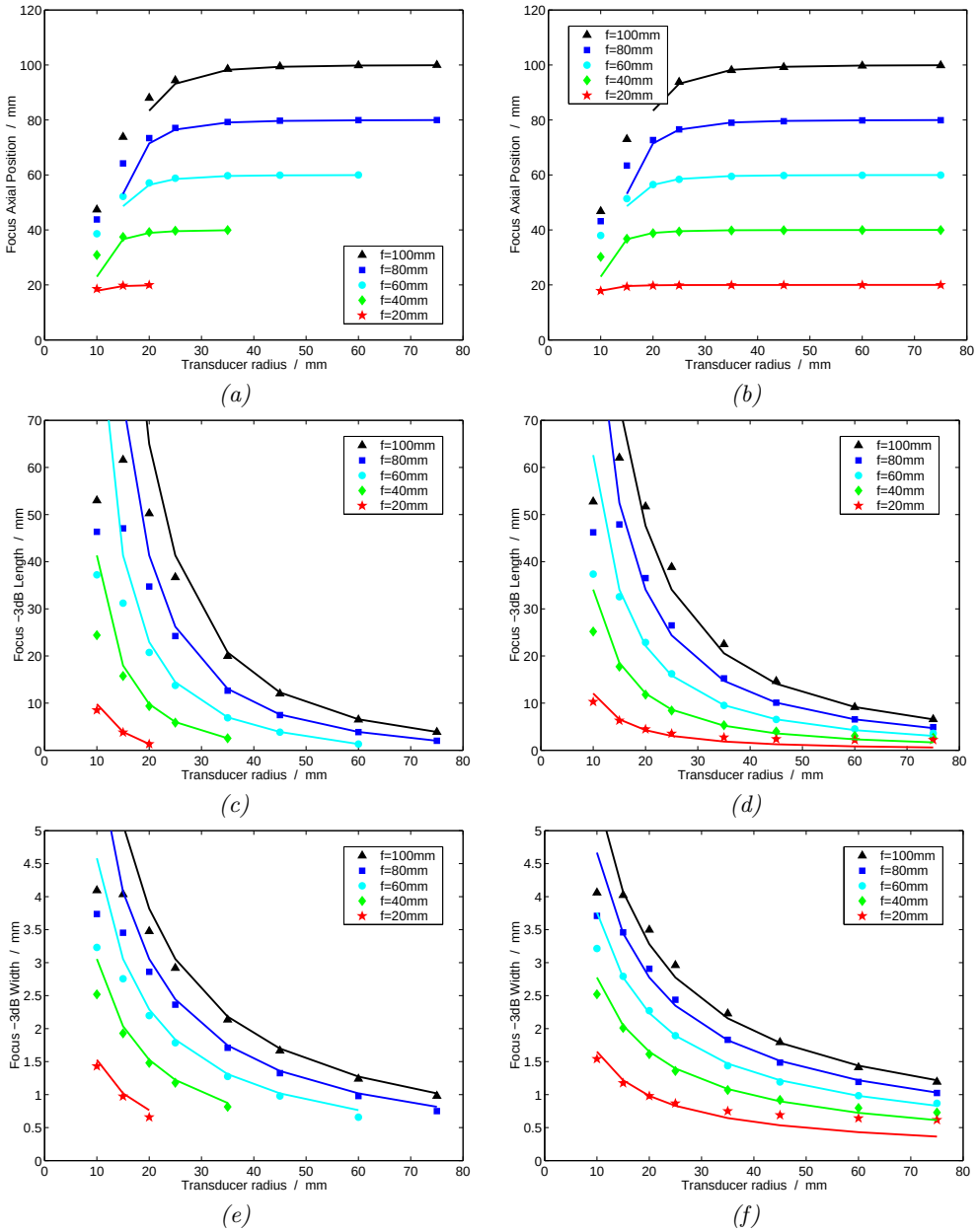

Figure 3.3: Comparison between the simulation results and the models given in tables 3.1 and 3.2 for (a,c,e) an idealised 1 MHz spherically curved single element and (b,d,f) an idealised 1 MHz plane circular phased array. (a,b) Focal position. (c,d) Focal region -3 dB length. (e,f) Focal region -3 dB width. The points indicate the simulation results, while the lines represent the models given in the tables.

3.5 Simulation of a practical transducer

The secondary array design parameters, which relate to the elements within the array, modify the field from the idealised case. These include practical considerations such the size and shape of elements, and the geometry of the element layout. These factors had to be considered in order to develop a design for our prototype array.

3.5.1 Element shape

Manufacturing considerations influenced the choice of element shape, with complex shapes being avoided to simplify the construction process and allow the use of elements available from manufacturers without machining to shape. In particular, circular elements were chosen to keep the design simple and robust, since machining a frame to house circular elements is relatively straightforward. Moreover, the use of circular elements avoids unwanted 'hot-spots' that may appear close to the corners of rectangular elements [Cahill and Baker, 1997]. Simulations investigating element shapes other than circular are therefore not reported here.

3.5.2 Element size

The impact of element size on the ultrasound field of a planar array of variable radius with a phase defined focal depth had to be considered. Since no method for addressing this has been previously reported, a geometric approach has been adopted in the present work. For elements of a finite size, it is useful to note that the path length from the outermost edge of an element to the focus is different from the path length from the element centre. Let us call this difference in path length $\Delta Path$. In particular, it is useful to consider the outermost element in an array which, for focussing on the central axis of symmetry, will exhibit the largest value of $\Delta Path$ of any element, which shall be called $\Delta Path_{max}$.

Figure 3.4 illustrates the definition of $\Delta Path_{max}$, which is the difference in length between paths r_1 and r_2 for the outermost element in an array. If it is assumed that angle $\theta_3 \approx \frac{\pi}{2}$, then angles θ_1 and θ_2 are equal and can be calculated

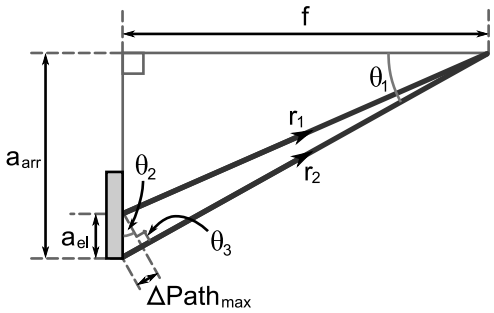

Figure 3.4: Diagram showing the definition of $\Delta Path_{max}$, where a_{el} is the element radius, a_{arr} is the array radius, and f is the phase-defined focal depth.

by equations 3.4 and 3.5 where a_{el} is the element radius and a_{arr} is the array radius.

$$\theta_1 = \sin^{-1}\left(\frac{\Delta Path_{max}}{a_{el}}\right) \tag{3.4}$$

$$\theta_2 = \sin^{-1}\left(\frac{a_{arr}}{r_2}\right) \tag{3.5}$$

Combining these two equations allows $\Delta Path_{max}$ to be expressed in terms of the element radius a_{el}, the array radius a_{arr}, and the length of path r_2. Using Pythagoras' theorem, $r_2 = \sqrt{a_{arr}^2 + f^2}$, where f is the phase-defined focal depth. Hence $\Delta Path_{max}$ can be expressed as shown in equation 3.6.

$$\Delta Path_{max} = \frac{a_{el}.a_{arr}}{\sqrt{a_{arr}^2 + f^2}} \tag{3.6}$$

Simulations were performed to look at the impact $\Delta Path_{max}$ has on the field produced by an array. This was done using an annular grid of circular elements as illustrated in figure 3.5, where the array radius, the element radius, and the phase-defined focal depth were varied in order to vary $\Delta Path_{max}$.

Figure 3.6 illustrates the effect $\Delta Path_{max}$ had on the 1D intensity profiles taken along the central axis of the transducer through the focal region, for an array of radius a_{arr} and a phase-defined focal distance f of 80mm. The relationship between intensity and element size will be discussed shortly, but first the relationship between the focal geometry and element size will be considered.

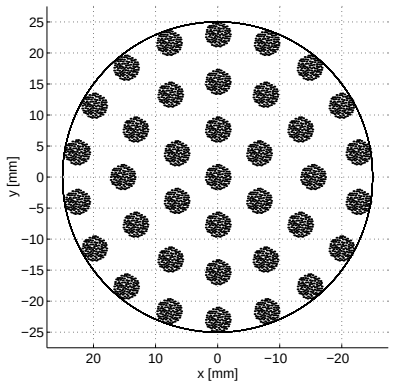

Figure 3.5: Layout of the annular grid of 37 circular elements used in the simulations studying the effect of increasing the element size. $\Delta Path_{max}$ was variable, depending on the chosen array radius a_{arr}, element radius a_{el} and phase-defined focal distance f.

From figure 3.6 it can be seen that the length of the focal zone was larger for arrays composed of larger elements. As $\Delta Path_{max}$ increased beyond approximately 0.5λ (where λ is the ultrasonic wavelength in the medium), the focal region grew significantly, with a regional minimum appearing where the focal peak was expected as $\Delta Path_{max}$ increased beyond about 0.7λ.

Figure 3.7 illustrates the relationship between the length of the focal region and $\Delta Path_{max}$, in this case for an array radius a_{arr} of 25 mm and for phase-defined focal distances f of 60, 80 and 100 mm. Simulations were performed for other values of a_{arr} and f and gave the same general result: the length (and hence volume) of the focal zone increased sharply when $\Delta Path_{max}$ increased beyond approximately 0.5λ. Beyond this limit, waves from the edge of an outermost element in the array arrive at the focus out of phase with waves from the centre of the same element, leading to destructive interference and a local minimum within the focal region, as was seen in figure 3.6.

It should be noted that while figures 3.6 and 3.7 were both obtained from the same set of simulated fields, care must be taken if making a visual estimate of the -3 dB focal length from the curves in figure 3.6, since the peak focal intensity of the 0.4λ profile is taken as the 0 dB point for all four curves in figure 3.6. In contrast,

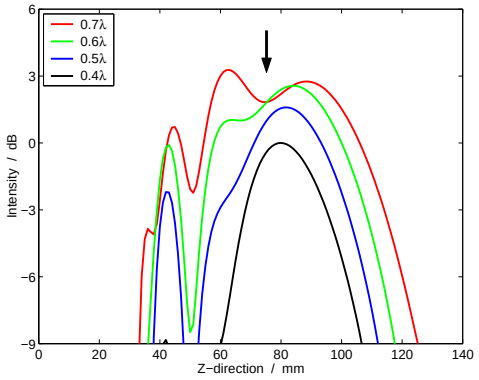

Figure 3.6: Simulated intensity profiles along the central axis of symmetry for an annular grid of 37 circular elements, where the array radius a_{arr} = 25 mm, the wavelength λ = 1.48 mm, and the phase-defined focal distance f = 80mm. The profiles shown are for arrays of four different element radii, chosen such that $\Delta Path_{max}$ = 0.4λ, 0.5λ, 0.6λ and 0.7λ. Note that the length of the focal zone increased in size significantly as $\Delta Path_{max}$ was increased beyond 0.5λ, and a regional minimum (indicated by the arrow) appeared at the focal peak as $\Delta Path_{max}$ was increased beyond 0.7λ.

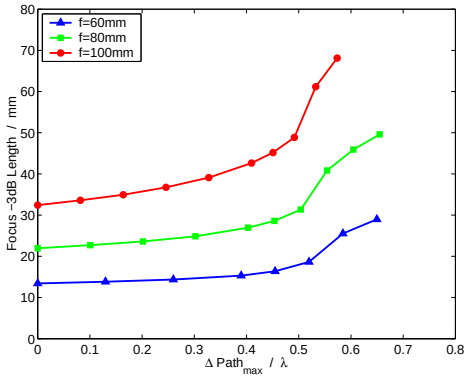

Figure 3.7: Graph showing the -3dB length of the focal zone from simulations of an annular grid of 37 circular elements, where the array radius a_{arr} = 25 mm, and the wavelength λ = 1.48 mm. $\Delta Path_{max}$ was varied by modifying the element radii and the phase-defined focal distance f. Note the sharp increase in the length of the focal zone as $\Delta Path_{max}$ was increased beyond 0.5λ.

in figure 3.7 the -3 dB focal lengths have been measured relative to the peak focal intensity of the profile in question. That is, for the 0.6λ data, the focal length uses the peak focal intensity of the 0.6λ profile as the 0 dB point.

A similar relationship was seen between the width of the focal region and element size. The focal width also increased with increasing $\Delta Path_{max}$, although without such a sharp increase beyond 0.5λ as was seen for the focal length.

To summarise, in order to produce a tight focal region $\Delta Path_{max}$ should be constrained as shown in equation 3.7. In combination with equation 3.6, this limits the size of element that can be used in a planar array.

$$\Delta Path_{max} < \frac{\lambda}{2} \tag{3.7}$$

Let us now return to the relationship between intensity and element size. In the simulations described here, the power delivered to the array remained constant per unit area of PZT, meaning that an array with larger elements was capable of delivering more power. As a result, the intensity of the focus increased as the element radius (and hence $\Delta Path_{max}$) increased. The relationship between element radius and the simulated focal intensity is illustrated in figure 3.8a, which demonstrates that there is a linear relationship (when plotted on a log-log scale) for the region of the graph where the elements are small. Best fit straight lines are shown on the plots, illustrating that the intensity I increases with the element radius a_{el} to the fourth power as described in equation 3.8. (This relationship can be verified visually from figure 3.8a, since on a log-log scale a fourth power relationship appears as a straight line with a gradient of four.)

$$I \propto a_{el}^4 \tag{3.8}$$

That the peak focal intensity increases with the element radius to the fourth power may seem unintuitive, but can be understood by considering the pressure amplitude rather than the intensity. The peak focal pressure amplitude increases linearly with the element area, since it is the integral of the pressures produced by each elemental area of the vibrating element. (This is the principle upon which Ul-

trasim is based, as described in section 3.2.1.) Intensity is proportional to the square of the pressure amplitude, and therefore the peak focal intensity is proportional to the square of the element area. This then leads to the relationship described in equation 3.8, that the peak focal intensity is proportional to the fourth power of the element radius.

As mentioned above, figure 3.8a indicates that the relationship between intensity and element radius is only valid where the element radius is small: As the radius is increased, the simulated data diverge from the best fit line. For different focal depths, the relationship between intensity and element radius breaks down at different values of the element radius, making it difficult to identify a convenient upper boundary for the relationship between intensity and element radius.

A clearer view of the situation can be obtained by considering the relationship between the peak focal intensity and $\Delta Path_{max}$, which is shown in figure 3.8b for the same set of simulations. Again, the straight lines in this plot represent the fits for the region of the plot where the element size was small, where the focal intensity is proportional to the element radius to the 4th power (equation 3.8). The point at which this relationship breaks down is easier to identify in this plot, and the 0.3λ and 0.5λ values (labelled in figure 3.8b as A and B respectively) are used as indicators of the approximate points at which: (A) The simulated data diverges from the trend ($I \propto a_{el}^4$); (B) The increase in intensity with $\Delta Path_{max}$ levels off. At values of $\Delta Path_{max} > \sim 0.5\lambda$ there is no further increase in intensity with element size.

In summary, an analysis of the focal intensity places the same upper limit on the element size as the analysis of the focal geometry, that $\Delta Path_{max}$ should be kept below $\frac{\lambda}{2}$.

Other workers have also considered the impact of element size on the function of phased arrays. Gavrilov and Hand [2000] noted in their simulations of a 256 element array (with a diameter of 110mm and a radius of curvature of 120mm) that increasing the element diameter beyond $\sim 5\lambda$ resulted in a deterioration of the intensity distribution and the appearance of grating lobes. There are similarities

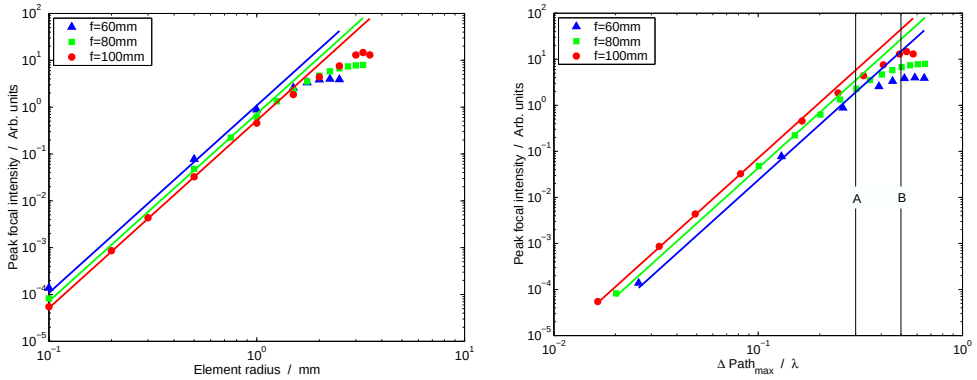

Figure 3.8: Graphs showing the peak intensity of the focal zone from simulations of an annular grid of 37 circular elements, where the array radius a_{arr} = 25 mm, and the wavelength λ = 1.48 mm. Simulations were performed for a variety element radii a_{el}. Plot (a) shows the peak focal intensity against element radius, and plot (b) shows the simulated peak focal intensity against $\Delta Path_{max}$. In each plot, the points represent the simulation results while the straight lines illustrate the fit, where $I \propto a_{el}^4$. In plot (b), two vertical black lines labelled A and B are also shown, indicating the locations on the x-axis where $\Delta Path_{max}$ is equal to 0.3λ and 0.5λ respectively. See the main text for further comments on A and B.

between this and the finding from the present analysis that $\Delta Path_{max}$ must be limited to less than $\frac{\lambda}{2}$. Wooh and Shi [1998] also considered the impact of element size on the field produced by a phased array. Although their work did not place an upper limit on the useful element size, it did highlight that element size has an impact on the grating lobes. However, as will be demonstrated in the next section, the geometry of the element layout is the critical factor in this regard.

3.5.3 Element layout geometry

For arrays composed of circular elements, the geometry of the element layout has been considered by Goss et al. [1996] and Gavrilov and Hand [2000], who demonstrated that there are advantages in the use of a randomised distribution of elements over a regular arrangement of elements. In particular, the use of a randomised layout significantly reduces the intensity of the grating lobes in comparison to a regular array layout.

Goss et al. [1996] investigated the element layout pattern, looking at the possibility of basing an array on a close-packed hexagonal pattern, but with elements omitted to reduce the regularity in the array. Their results showed that this approach still has fundamental problems with grating lobes under steering, as might be expected given that such an element layout is based upon multiples of a single lattice constant. To achieve a reduction in the grating lobe intensity an array with elements distributed randomly, not based upon multiples of a common lattice constant was required.

To quantify the performance of a planar array of circular elements, simulations were performed to study a number of element layout geometries. Figure 3.9a,d,g,j illustrates the layouts of the simulated arrays, each of which had an overall array radius of 22 mm, enclosing elements of radius 2 mm arranged in a number of patterns: square grid; hexagonal grid; annular grid; and randomised. The number of elements within the arrays was 61 for each of the regular layouts, and 60 for the randomised layout.

For each array geometry, two further graphs are shown in figure 3.9 as a way of visualising the spatial periodicity of the array. In the first of these (figure 3.9b,e,h,k) the spectrum of inter-element pitches is shown for all combinations of element pairs within the array. The periodicity of the square and hexagonal arrays is evident from the large discrete peaks in figure 3.9b,e, while the annular grid (figure 3.9h) has a somewhat reduced periodicity. The random array has an even spread of inter-element pitches (figure 3.9k) with a single prominent peak at an inter-element pitch of 4.5 mm, and this peak is a consequence of the need to pack the elements tightly enough to allow 60 to fit within the radius of the array. The fact that the inter-element pitch is never less than 4 mm in any of the four arrays is a consequence of the finite element size, since elements cannot be spaced more closely than twice the element radius.

The periodicity of an array is not defined by the distribution of inter-element pitches alone, and therefore the second graph for each array (figure 3.9c,f,i,l) is shown to illustrate the spectrum of inter-element angles for all combinations of element

pairs. The inter-element angle is defined as the angle between the y-axis and the line through the centre of both elements in the pair. The probability densities in these plots are quantised with a bin width of $\frac{\pi}{128}$ radians to achieve a resolution of better than 1% while using a power of 2 for ease of computation. Since the square array has fourfold rotational symmetry, the distribution of inter-element angles in figure 3.9c repeats with a period of $\frac{\pi}{2}$. Similarly, the hexagonal and annular grid arrays have sixfold rotational symmetry, and the distribution of inter-element angles for these (figure 3.9f,i) repeats with a period of $\frac{\pi}{3}$. The random array has no rotational symmetry, and hence has an evenly spread distribution of inter-element angles (figure 3.9l).

The benefit in obtaining the distributions of inter-element pitches and angles for each array is that these can be used to provide simple estimates of the positions of the grating lobes. The peaks in the distribution of inter-element pitches may be used to obtain a simple prediction of the off-axis distance between the focus and the primary grating lobes (using equation 2.13) and the peaks in the distribution of inter-element angles may be used to predict the angles at which these grating lobes will occur. For example, for the hexagonal array (figure 3.9d,e,f) the first peak in the distribution of inter-element pitches is at approximately 5 mm. Using equation 2.13, this would predict that at a depth of 80 mm the primary grating lobe will occur at a distance of 24 mm away from the central focal region. The three most prominent peaks in the distribution of inter-element angles define the angles at which these primary grating lobes occur. This therefore predicts that there will be six localised primary grating lobes surrounding the central focal region, each separated by an angle of $\frac{\pi}{3}$ radians.

Simulations were performed with the array focussed at a depth of 80 mm, the midpoint of the proposed range of depths for the hypothetical tumour (section 1.4), which was centred at a depth between 60 and 100 mm. A number of simulations were performed for each array to study the effect of steering the focus away from the central axis of the array by up to 20 mm, equal to the proposed width of the hypothetical tumour.

Figure 3.10a,c,e,g illustrates the simulated intensities for each array in the x, y plane through the focus, where the array was focussed to a depth of 80 mm on the central axis of the array. It can be observed from figure 3.11e that the positions of the grating lobes for the hexagonal array are in good agreement with the predicted positions calculated above: The simulated primary grating lobes are at a distance of approximately 25 mm from the central focal region, and are each separated by an angle of $\frac{\pi}{3}$ radians.

Figure 3.10b,d,f,h illustrates the simulated intensities for each array in the x, y plane through the focus, where the array was focussed to a depth of 80 mm and a distance of 20 mm away from the central axis of the array.

It can be observed from these plots that the pattern of grating lobes produced by an array is dependent on the geometry of the array, and follows the same principle as the maxima produced in a plane parallel to the surface of a diffraction grating. Arrays based upon a regular layout of elements produce grating lobes with localised maxima, while an array based on random layout of elements produced a grating lobe where the energy within the lobe was spread over a large volume rather than concentrated within a small region. Thus the grating lobes produce by the random array (figure 3.10g,h) appear as a band rather than a number of localised maxima. The position of this band relative to the focus is determined by the average inter-element pitch, which is turn is determined by the element radius in addition to the condition that no two elements may overlap. In addition, the annular grid has a layout similar to that of the hexagonal grid but with slightly reduced periodicity, and as a result its grating lobes (figure 3.10e,f) are slightly more diffuse than the localised hot-spots produced by the hexagonal grid (figure 3.10c,d).

While the positions of the grating lobes peaks relative to the focus are unaffected by steering, the relative intensities of the grating lobes are not. As a consequence of steering the focus away from the central axis of the array the grating lobes also move, with the result that some of the grating lobe maxima move closer to the central axis of the array and increase in intensity. Figure 3.10b,d,f shows that for a square, hexagonal or annular grid of elements, steering the focus 20 mm away from

the central axis resulted in the intensities of the grating lobes increasing to greater than the intensity of the focus itself. While the intensity of the grating lobe for the random array also increased, it remained well below the intensity of the focal region since energy in the grating lobes was spread across a relatively large volume rather than being localised in a number of discrete hot-spots.

To allow a more detailed analysis of the relative grating lobe intensity to be made, further simulations of the field intensities in a plane parallel to the transducer surface and through the centre of the focus were performed for both water and a homogeneous tissue media ($\mu = 0.5$ dBcm^{-1}). The ratio of the maximum intensity in the grating lobes to the peak focal intensity was found in this plane for fields focussed 0, 5, 10, 15 and 20 mm away from the central axis of the array.

Figure 3.11 compares the peak intensity of the grating lobes relative to the focal intensity for the four array geometries illustrated in figure 3.9a,d,g,j as the focal region is steered away from the central axis of the array, demonstrating the clear benefits of a non-periodic distribution of elements. When focussed on the central axis of the array, the relative grating lobe intensity is lower for the randomised array than for any of the others, and it remains the lowest as the focus is steered away from the central axis. Indeed, it is the only array geometry of the four where the grating lobes are less intense than the focal region when the focus is steered 20 mm away from the central axis.

3.5.4 Element number density

To study the effect of increasing the number density of elements within a planar array of randomly positioned elements, simulations were performed for a number of focal positions. To characterise the field, the effect of increasing the number of elements on the following field characteristics was investigated: the intensity (both peak and average) of the focal region; the volume of the focal region; the intensity of the grating lobes relative to the focal intensity; and the pressure distribution within the region of the field between the surface of the transducer and the focus. The impact of the element number density on the steering capability of the array was

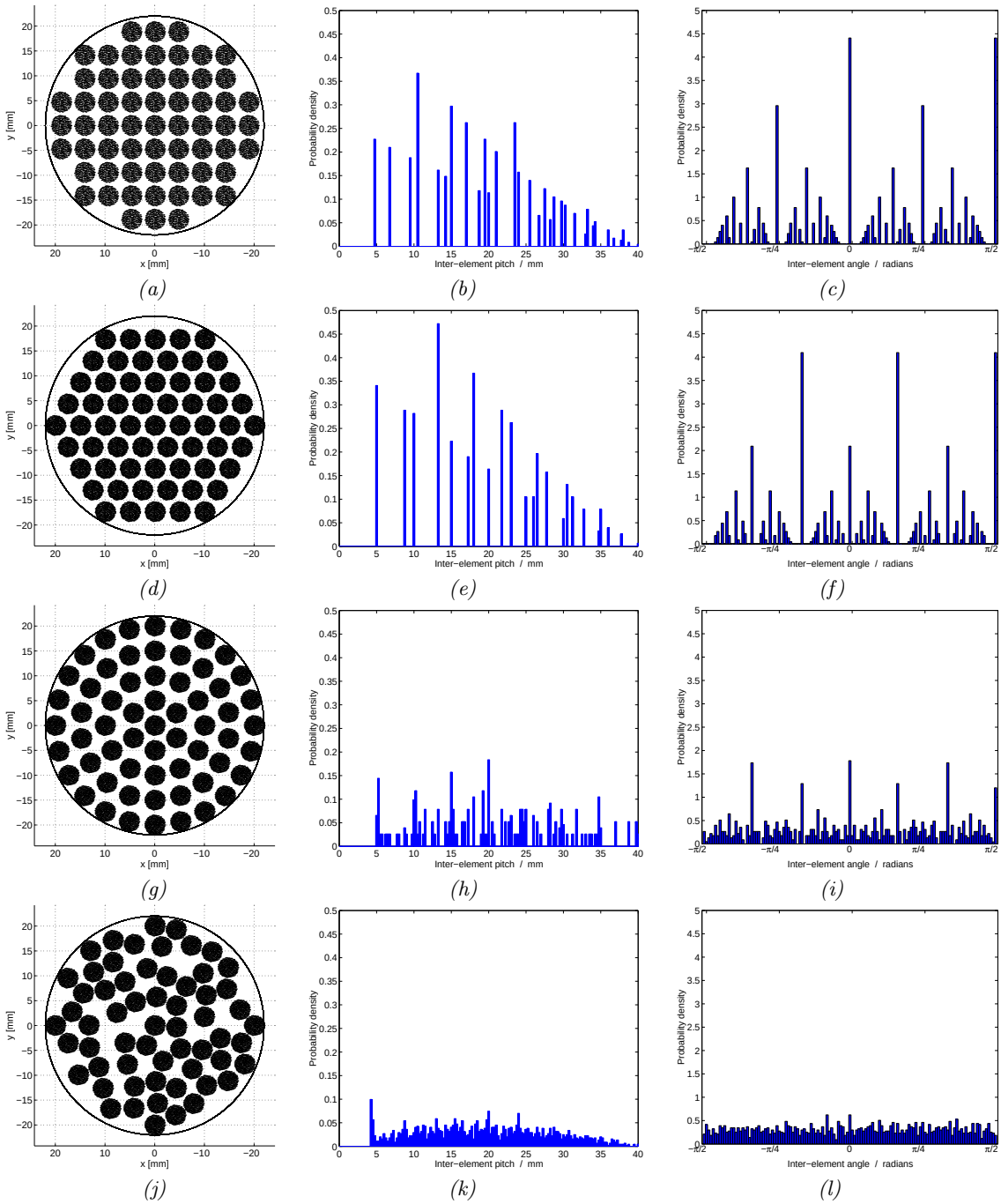

Figure 3.9: The array configurations used to study the impact of array geometry. Plots (a,d,g,j) illustrate the layouts of square grid, hexagonal grid, annular grid and random arrays respectively. For each of these arrays, the spectrum of inter-element pitches is shown in plots (b,e,h,k), where the probability densities are quantised with a bin width of 0.25 mm. Similarly, the spectrum of inter-element angles is shown in plots (c,f,i,l), where the probability densities are quantised with a bin width of $\frac{\pi}{128}$ *radians.*

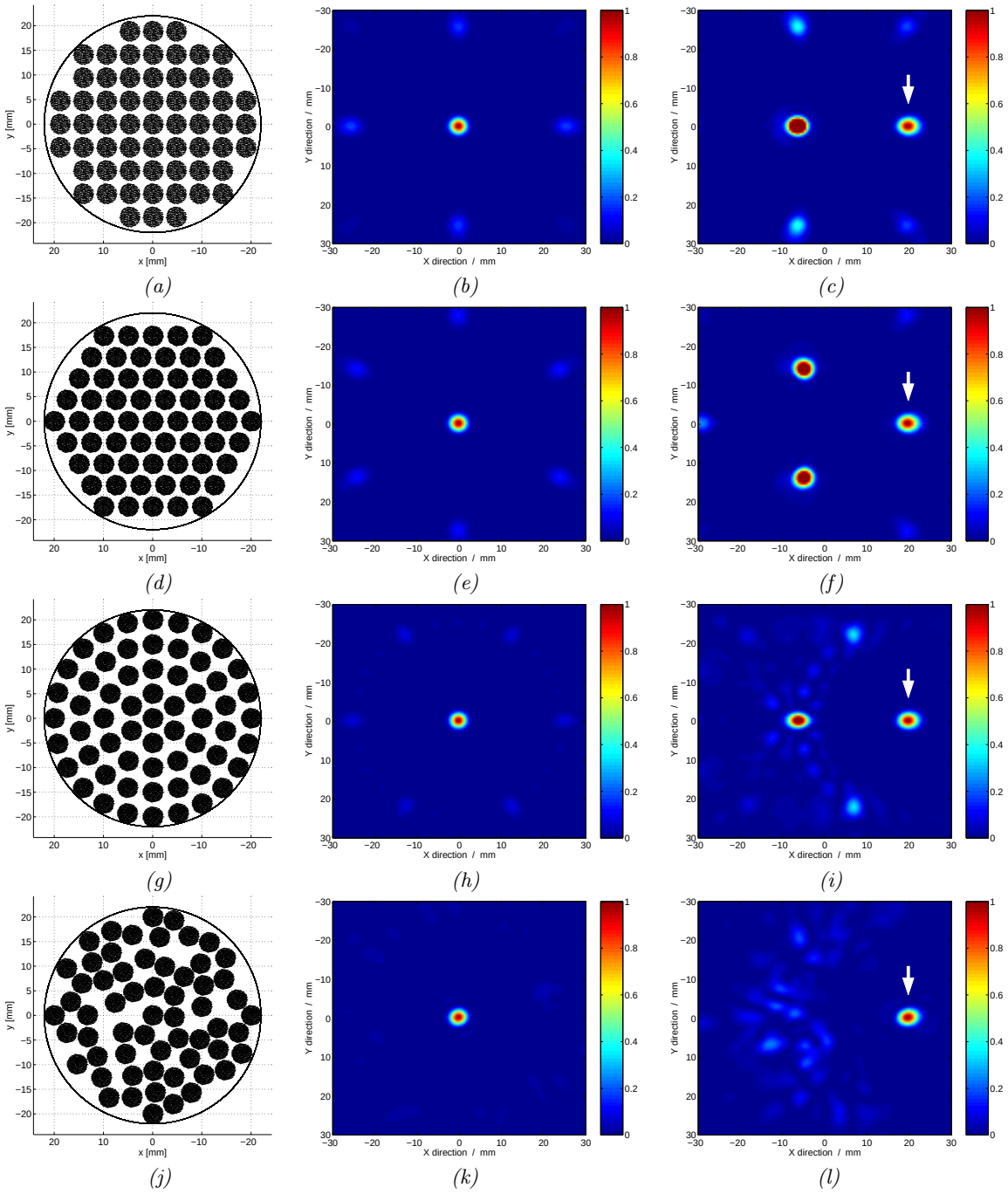

Figure 3.10: 2-D simulation results illustrating the grating lobes produced by the arrays shown in plots (a,d,g,j). The plots illustrate the intensity in the x, y plane through the focal region with the array focussed at a depth of 80 mm and steered away from the central axis of the array by a distance of (b,e,h,k) 0 mm and (c,f,i,l) 20 mm. The intensities are normalised relative to the peak focal intensity. In (c,f,i,l) the white arrows indicate the position of the focal region, while the other maxima belong to the grating lobes.

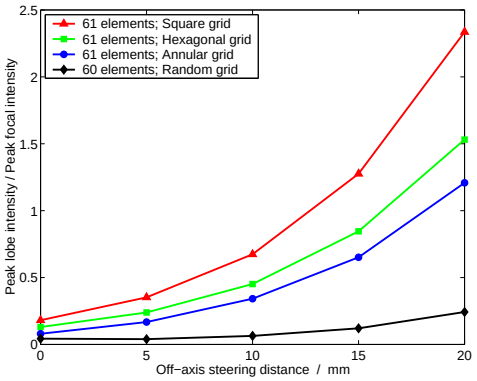

Figure 3.11: Simulation results showing the peak relative grating lobe intensity produced by several array geometries as the focus is steered away from the central axis of the array. The focal depth was 80 mm.

also considered here.

The simulations described in the present section studied the field produced by a planar array of radius 22 mm, composed of randomly positioned elements each of radius 2 mm, with the number of elements in the array varied between 7 and 60. The choice of array and element radii used here is the same as those which will be used in the construction of the physical array described in chapter 4, and the rational behind their use will be covered in that chapter. While the present section makes use of this particular choice of dimensions, the conclusions which will be reached regarding the impact of the element number density on the characteristics of the field can also be applied more generally to any choice of array and element dimensions which satisfy equation 3.7.

Analysis of the simulation results showed that both the peak and average intensity of the focus increased with the square of the number of elements (figure 3.12b). In addition, the focal intensity decreased as the focus was steered away from the central axis of the array (figure 3.12b). When steered to a distance of 20 mm away from the central axis, the intensity of the focal region was just less than half the on-axis focal intensity. As described in section 2.3, the decrease in intensity with off-axis steering is defined by the element geometry, and the simulated result

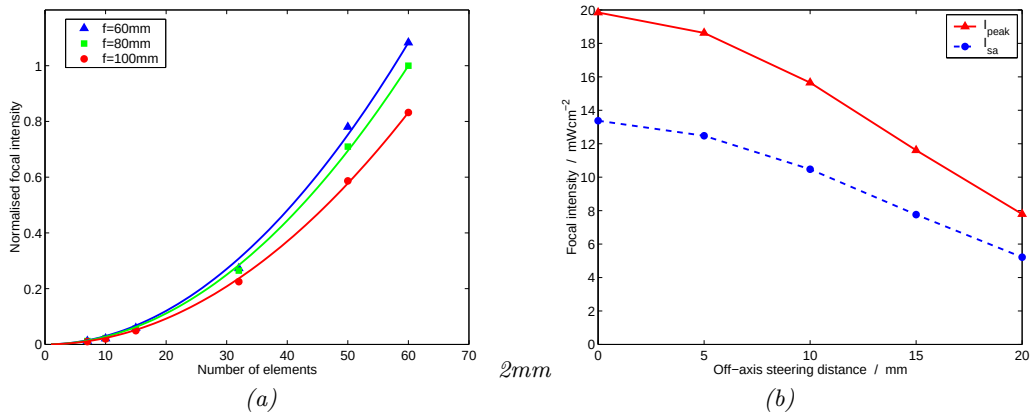

Figure 3.12: (a) Simulation results illustrating the effect of increasing the number of elements within the array on the peak focal intensity. The focus was positioned on the central axis of the array at depths of 60, 80 and 100 mm. The intensities are normalised relative to the peak focal intensity of the 60 element array focussed at a depth of 80mm. (b) Simulation results illustrating the effect of steering the focus away from the array's central axis of symmetry on the focal intensity for an array composed of 15 randomly positioned elements. The focal depth was 80 mm.

can be compared against the simple prediction obtained from equation 2.14 for an array of elements each of radius 2 mm which was shown in figure 2.1, where the focal intensity also decreased to just less than half the on-axis focal intensity when steered 20 mm away from the central axis.

Analysis of 3-D simulation results showed that the volume of the focus increased as the focal region was steered away from the central axis of the array (figure 3.13). Increasing the number of elements in the array had no effect on the -3 dB volume of the focal region.

For analysis of the relative grating lobe intensity, a plane parallel to the transducer surface and through the centre of the focus was taken, and the ratio of the maximum intensity in the grating lobes to the peak focal intensity was found in this plane. This analysis was performed for water and a homogeneous tissue media ($\mu = 0.5$ dBcm^{-1}).

The ratio of the maximum intensity of a grating lobe outside the focal zone to the maximum intensity within the focal zone was determined and is shown in

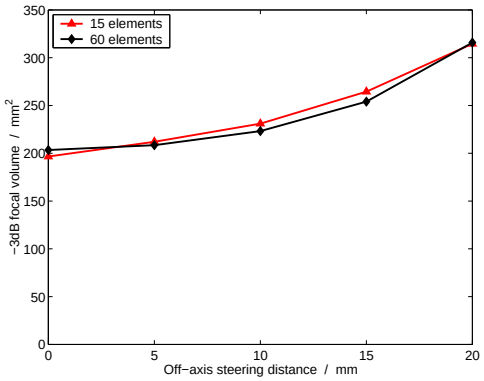

Figure 3.13: Simulation results illustrating the effect of steering the focus away from the array's central axis of symmetry on the focal volume for an array of randomly positioned elements. The focal depth was 80 mm.

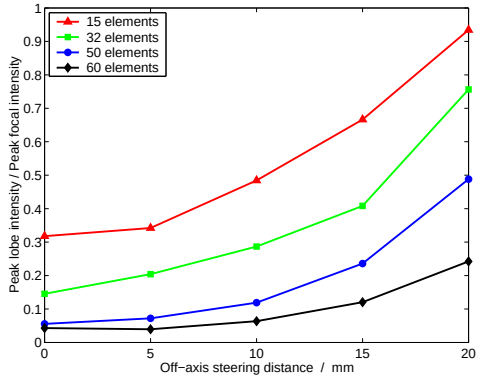

Figure 3.14: Simulation results illustrating the effect of increasing the number of elements in a random array on the peak relative grating lobe intensity. The focal depth was 80 mm.

figure 3.14. This clearly shows that the relative grating lobe intensity increased as the focus was steered away from the central axis of the array, while increasing the number of elements for a particular focal position decreased the maximum grating lobe intensity relative to the peak focal intensity.

What is happening here is that an increase in the number of elements results in a decrease in the characteristic inter-element pitch for the array, since the overall array radius remains constant. The consequence of this is that the grating lobes occur at a greater distance from the central focal region and, as demonstrated by

figure 2.1 in section 2.3, will therefore have a lower intensity relative to the focal region.

Although the absolute intensities of the focus and the grating lobes were affected when the simulated medium was changed from water to a homogeneous tissue medium, the geometries of the focal region and grating lobes and their relative intensities were not.

3.6 Summary

The primary aim of the simulation work reported in this chapter was to establish the physical principles that govern the behaviour of planar phased array transducers. This has been dealt with in the current work by separating the problem into two parts, by first considering the fundamental array parameters in section 3.4 and the secondary array parameters in section 3.5.

In section 3.4 the concept of an idealised transducer transducer was introduced, enabling a new set of equations to be established which relate the field characteristics (such as the geometry of the focal region) to the fundamental array parameters (the overall array radius and the radius of curvature).

Section 3.5 considered the impact of the secondary array parameters which modify the field from that of the idealised case. The analysis has demonstrated that an upper limit can be placed on the element radius, allowing the focal intensity to be maximised while avoiding the undesirable effects that arise if elements with a radius greater than the upper limit are used. The benefits of a random layout have been demonstrated, especially with regard to minimising the intensities of the grating lobes under steering. And finally, the impact of the number density of elements on the field under steering have been investigated, demonstrating that increasing the element number density has no impact on the geometry of the focal region, but provides a reduction in the intensities of the grating lobes relative to the focal region.

Chapter 4

Array design and construction

4.1 Requirements of the prototype array

The hypothetical spherical tumour described in chapter 1.4, with a diameter of 40 mm and centred at a depth between 60 and 100 mm, was considered to guide the design of the array described in this chapter, with the aim being to produce an array capable of creating a focal region within such a tumour. The simulation models discussed in sections 3.4 and 3.5 were used to develop the array design, and an experimental array was constructed and characterised in an acoustic tank to verify the viability of the chosen approach.

4.2 Design of the array

Given the requirement to produce an array design that would be straightforward to construct, the design of the experimental array was based upon a planar array of circular elements. A random element distribution pattern was chosen as chapter 3, in combination with work reported by Goss et al. [1996], had shown that this gave significant benefits compared to regular patterns. The exact element co-ordinates within the array were generated within Ultrasim, using the custom script described in section 3.2.3. The remaining array parameters that needed to be specified to complete the design were the array radius and the element radius.

The models obtained from the consideration of an idealised phased array (section 3.4) were used to determine the minimum array radius required to ensure that the focal region (defined by its -3 dB surface) lies within the dimensions of the

hypothetical spherical tumour defined in section 1.4. For a planar array with an ultrasonic frequency of 1 MHz (section 2.4), such that the ultrasonic wavelength in a medium of water is approximately 1.48 mm, an array radius of at least 22 mm ($G_p = 10$) is required according to the equations in table 3.2. This ensures that the length of the focal region lies within the tumour, since it is the focal length, rather than width, which is the limiting dimension.

While an array could be constructed with a radius larger than this, for the present work an experimental array with a radius of 22 mm was constructed to study the limiting case for several reasons:

1. The available drive electronics [Lovejoy et al., 1994] limited the number of elements within the array to fifteen, and therefore minimising the array radius would minimise the space between elements. It is to be expected that the magnitude of the inter-element crosstalk will be greater for closely spaced elements than widely spaced elements, and therefore measurements of the crosstalk within the array will be of more interest for smaller arrays.
2. Increasing the radius of the array would require the element radius to be reduced in order to satisfy equations 3.6 and 3.7 at the edge of the array. Since the number of elements in the array is fixed at fifteen, reducing the element radius would lower the total output power of the array, in turn reducing the focal intensity that could be achieved by the array.
3. For an planar array to be used in a clinical context, a small array radius will be advantageous in that it will allow the array to fit better to the curvature of the body than would a large planar array.

The maximum element radius is defined by equations 3.6 and 3.7, which for a drive frequency of 1 MHz, a minimum depth of 60 mm and an array radius of 22 mm limited the element radius to no more than 2.15 mm. Since the intensity produced by each element is proportional to the square of the element's area (as shown in figure 3.8a), choosing as large an element as possible is desirable to maximise the heating capability of the array. In practice elements of radius 2 mm were chosen

for the array as this dimension is commonly stocked by PZT suppliers. The fifteen elements in the array were arranged quasi-randomly, with a minimum inter-element pitch of 9 mm to ensure an approximately even distribution.

Figure 4.1a illustrates the final design of the array. The distributions of inter-element pitches and angles are shown in figures 4.1b and 4.1c respectively, and provide a simple way of visualising the spatial periodicity of the array (as described in section 3.5.3).

The peak in the inter-element pitch distribution at 9 mm is a consequence of the fact that the element layout is not truly random, but has been constrained by forcing a minimum pitch of 9 mm to ensure a spatially even spread of elements. Without this constraint, a truly random placement tends to produce an uneven spread of elements, creating an array containing clusters of elements as well as large spaces free of elements. An even spread of elements is desirable as it better approximates an ideal array of the desired radius.

Using equation 2.13 along with the information presented in figures 4.1b and 4.1c, the positions of the grating lobes produced by the array can be predicted. From the peak in the distribution of inter-element pitches at 9 mm, the first order grating lobe can be calculated to occur at an angle of 9.5° from the focal region. Due to the absence of any strong peaks in the distribution of inter-element angles (figure 4.1c), the grating lobes will take the general form of a ring surrounding the focal region, rather than being composed of localised high intensity spots. As will be discussed in section 6.5, simulated and experimentally measured fields from the array are in good agreement with these simple predictions.

4.3 Construction of the array

PZT comes in a variety of compositions which are designed for a number of different applications [Gallego-Juárez, 1989]. Of the possible compositions, PZT-8 is particularly suitable for applications which require high power handling capabilities and has been used by previous workers in the construction of ultrasonic arrays intended

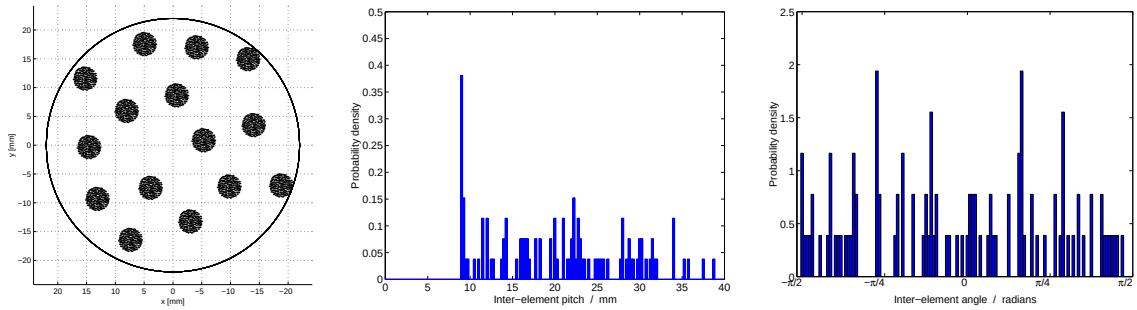

(a) *(b)* *(c)*

Figure 4.1: The design of the prototype array. (a) The array layout. (b) The spectrum of inter-element pitches, where the probability densities are quantised with a bin width of 0.25 mm. (c) The spectrum of inter-element angles, where the probability densities are quantised with a bin width of $\frac{\pi}{128}$ *radians.*

for both hyperthermic [Sun et al., 2003] and FUS [Saleh and Smith, 2004, 2005] applications. PZT-8 (Sparkler Ceramics, Bhosari, India), equivalent to Navy type III for which the PZT parameters are given in table 4.1, was therefore chosen for use in the experimental array in the present work.

For a circular PZT element vibrating as an ideal piston, the ultrasonic wavelength in the PZT is equal to twice the thickness of the element. Given the planar frequency constant of PZT-8 in table 4.1, for a resonant frequency of 1 MHz an element thickness of 2.30 $\pm$ 0.18 mm is required. In practise, the nearest suitable thickness readily stocked by PZT suppliers is 2 mm, corresponding to a resonant frequency of 1.15 $\pm$ 0.09 MHz, and so these were used for construction of the experimental array. Although this frequency is slightly higher than that of the drive electronics, seeking to achieve a perfect match is impractical since the resonant frequency of PZT decreases slightly as the elements heat up during use [Martin et al., 2003].

A Perspex frame was machined to house the elements, with fifteen 4 mm diameter holes in the correct position for each element according to the design described in section 4.2. The front surface of the frame was recessed around each hole to allow a matching layer to be incorporated for each individual element, as illustrated in cross-section in figure 4.2a. Separate matching layers were provided

Table 4.1: Navy type III specifications for the PZT used in the fifteen element array [U.S. Department of Defense, 1995].

Property	Symbol	Units	Typical Value
Relative permittivity	k_3^T		1025 $\pm$ 12.5%
Piezoelectric coefficient	d_{33}	10^{-12} mV^{-1}	215 $\pm$ 15%
Planar frequency constant	N_p	Hz·m	2300 $\pm$ 8.0%
Density	ρ	kgm^{-3}	$\geqslant$ 7450
Curie Temperature	T_C	°C	325

for each element to prevent lateral propagation of ultrasound along the matching layer, a potential cause of acoustic crosstalk between transducer elements [Wojcik et al., 1996; Daum and Hynynen, 1999].

A network of copper wire was constructed at the rear of the Perspex frame, and holes were drilled in the frame to allow branches of the network to pass through the frame into each of the recesses at the front face. With the PZT elements held in place in the frame, a wire was soldered between the front face of each element and the network connection in the recess. This provided a single common electrical connection to the front electrode of all the elements. The solder contacts to the front of the PZT elements were kept small to ensure that they did not extend above the level of the front face of the Perspex frame. This would allow the matching layer, which would later fill the recesses, to provide electrical isolation between these solder contacts and the medium. However, since the front face of each element was electrically common and would be connected to ground during the operation of the array, the electrical isolation provided by the matching layer would not be critical for safety if such an array were used in a clinical context. The high drive voltages would be applied to the rear face of the PZT, precluding the possibility of a high voltage coming into contact with the medium, and providing safety should the matching layer isolation be breached by damage or scratches to the front of the array.

Once the soldering had been completed at the front of the array, adhesive

tape was applied to form a seal at the rear face of each element and the rear of the Perspex frame, and the alignment of each element within the frame was checked. The tape was required to prevent the liquid epoxy from seeping through between the elements and the frame. The recesses on the front surface of the array were then filled with the epoxy resin to form the matching layer.

Araldite 2020 was chosen as a suitable epoxy due to its low viscosity in its liquid form and its water-resistant nature in its cured state. It was mixed at a ratio of 100:35 (resin:hardener) by volume according to the manufacturer's recommendation, poured onto to the front surface of the Perspex frame until it stood proud of the Perspex surface, and then allowed to cure at an elevated temperature (approximately 40°C) for 24 hours to ensure adequate epoxy conversion [Karayannidou et al., 2006]. Once cured, the epoxy was ground back using wet abrasive paper until the surface was once again level with the Perspex. This process allowed a smooth, level matching layer to be formed, while at the same time bonding each element securely into the frame and also providing protection for the front electrodes. The low viscosity of the Araldite allowed any gas bubbles formed during its application to rise to the surface of the epoxy. While some of the bubbles escaped to the atmosphere, some were trapped by the skin of the curing epoxy. However, since the epoxy was applied so that it stood proud of the front surface of the Perspex frame, the bubbles within that region would be removed during at a later stage in the construction process.

The thickness of the matching layer was defined by the depth of the recess in the Perspex frame. Once the epoxy was ground level with the Perspex, the thickness of the frame was measured with a micrometer at several points around the array to ensure that it was even at each point, and therefore that the matching layer was an even thickness across the face of the array. The speed of sound in Araldite 2020 is 2610 ms^{-1} [Ma et al., 2007], and hence the wavelength of a 1 MHz sound wave is 2.6 mm. To provide a matching layer of thickness $\frac{\lambda}{4}$ for optimal matching between the PZT and the medium, a layer thickness of 0.65 mm was required. For the construction of the experimental array a thicker 1 mm matching layer was used to ensure that the solder connections at the front of the PZT lay entirely within the

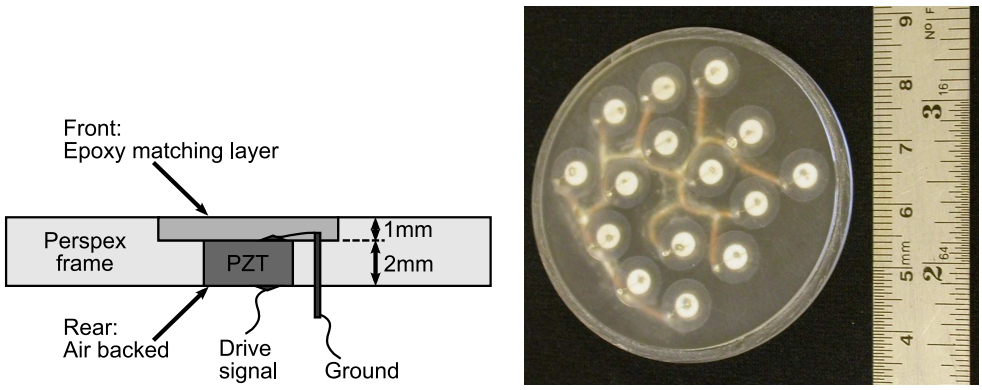

Figure 4.2: (a) Cross-section of an element within the array. (b) The completed array, before being housed and wired. The array radius was 22 mm, each PZT element was 2mm in radius, and each element's matching layer enclosed it by 2 mm. Since the perspex frame and the epoxy matching layers are transparent, the network of copper wire used to route the common electrical connections to the front faces of the PZT discs can be seen.

matching layer, thus avoid any breaches in the electrical isolation provided by the layer. The results reported by Wojcik et al. [1996] indicate that the thickness of the matching layer is not critical to ensure adequate coupling into the medium.

At this stage, the array looked as shown in figure 4.2b and was ready to be built into its housing. The common connections to the front face of each element can be seen in the figure, as can the individual matching layers surrounding each element and the network of copper wire at the rear of the frame (visible through the transparent Perspex).

The completed Perspex frame was then housed within an aluminium case as illustrated in figure 4.3a. Fifteen 1.50 m lengths of 50 Ω coaxial cable (type RG178B/U) were used to supply the drive signals for the PZT elements. The cables entered the transducer casing from the top, connecting to sections of stripboard inside the casing, as can be seen in figure 4.3b. Due to the limited space inside the casing, three separate sections of stripboard were used with five drive channels per section. Wires were run from each drive track on the stripboard and soldered to the rear face of the appropriate PZT element. The stripboard ensured that the solder

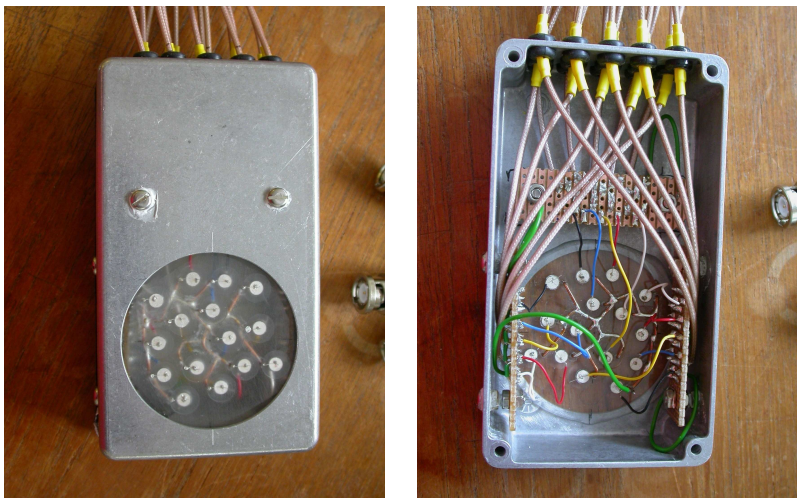

(a) *(b)*

Figure 4.3: The 15 element array. (a) External. (b) Internal.

connections to the PZT would not be stressed by movement of the coaxial cables, making sure that the wiring of the array was robust.

The total length of each of the signal pathways, measured from the output of the transducer drive electronics to the element's rear electrode, differed by up to a few centimetres due to the three different stripboard positions within the casing and the range of distances between the elements and the stripboard. An estimation of the phase delay introduced by this difference in signal path length can be made by assuming that the difference lies in the lengths of the coaxial cables. Since the propagation velocity of the coaxial cable is specified as 2×10^8 ms^{-1}, the delay introduced by a difference in cable length of a few centimetres is less than 1 ns, which is negligibly small since it translates to less than 0.1% of a wavelength. The assumption could therefore be made that the relative phase of each channel at the output of the transducer drive electronics was the same as that at the PZT drive electrode.

Steps were taken to minimise electrical cross-coupling between drive channels. The outer conductor of each coaxial cable was grounded to shield the inner conductor which carried the drive signal, and ground tracks were placed between each drive

track to minimise electrical cross-coupling on the sections of stripboard. A ground connection was also made to the aluminium casing.

Other workers have reported the use of various backing materials at the rear of each element such as tungsten/epoxy mixtures [Hutchins et al., 1986] to dampen the element vibration after the end of each drive pulse or to suppress undesirable modes of vibration, or a flow of water [Deardorff and Diederich, 2000] to improve cooling of the elements within the array. In the present work the rear faces of each element were left air-backed, allowing the PZT to ring undamped after application of a drive pulse and avoiding any loss of energy due to absorption in the backing layer [Persson and Hertz, 1985]. The absence of any backing layer also had the added benefit of keeping the array design as simple as possible.

Impedance matching of the elements to the output of the drive electronics was not provided, keeping the interface between the two as simple as possible, and ensuring that the phase of the drive signal to each element was precisely defined.

Chapter 5

Array characterisation techniques

5.1 Introduction

As discussed in section 4, a transducer array design was developed based upon the simulation work. To verify the simulation predictions, measurements were made of the field produced by the transducer array. This chapter describes the experimental apparatus and the methods used to make measurements of the field profiles from the transducer array. Also described are the techniques used in the comparison between the simulation predictions and the experimental results.

5.2 Apparatus

The standard method for experimental measurement of the field from an ultrasonic source is to place the source in a water tank (termed an acoustic tank) and use a hydrophone to measure the ultrasonic pressure at various positions in the field [Benkeser et al., 1991; Cathignol et al., 1995; Fan et al., 1997; Clement and Hynynen, 2000]. The water contained within a sufficiently large acoustic tank approximates an infinite, homogeneous medium which can be considered as linear for the range of (relatively low) ultrasonic pressures that will be encountered in the present work. These properties mean that a water tank is a suitable medium in which experimental measurements can be taken for comparison against fields simulated using Ultrasim,

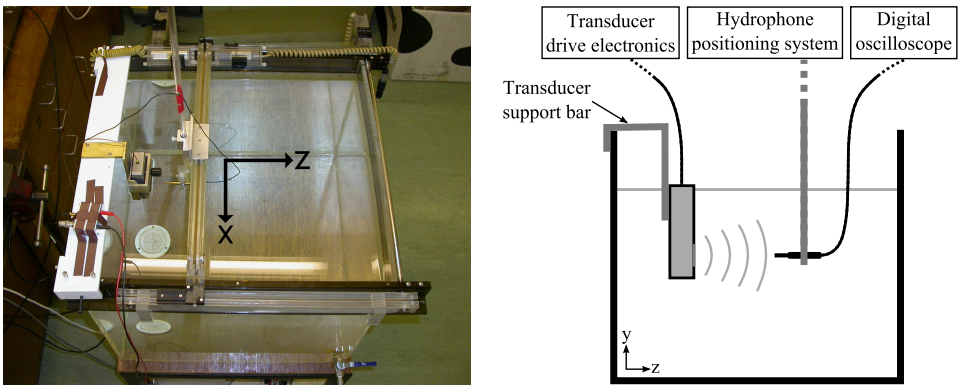

Figure 5.1: (a) The acoustic tank. A transducer is positioned at the left hand side of the tank, with the ultrasound beam propagating left to right. (b) Cross-section in the y, z plane through the transducer and hydrophone.

bearing in mind the assumptions about the medium required by Ultrasim which were discussed in section 3.2.2. In addition, water is a suitable choice of medium for experimental analysis of arrays intended for medical purposes since it has a speed of sound close to that of tissue (section 2.4).

In the present work, a Perspex acoustic tank (approximately cubic and 60cm per side) containing deionised water was used to measure 2-D field profiles of the array described in section 4. The acoustic tank is illustrated in figure 5.1, where a transducer is in position at the left hand side of the tank and a hydrophone, used to measure the ultrasonic pressure at each position in the field, is suspended from the carriage located at the middle of the x-axis belt-drive slide.

The apparatus was computer controlled, allowing for automated 2-D field profile measurement in the x, z plane. While the system was unable to scan in 3-D, scanning in the 2-D x, z plane alone is sufficient for fields with rotational symmetry (such as those produced by single circular elements - section 2.2), if the system is aligned such that the axis of symmetry is included in the measurement plane. While the fields produced by phased arrays typically exhibit some degree of rotational symmetry, depending on the geometry of the array it may be necessary to align the rotation of the array about the z axis to ensure that the grating lobes lie in the

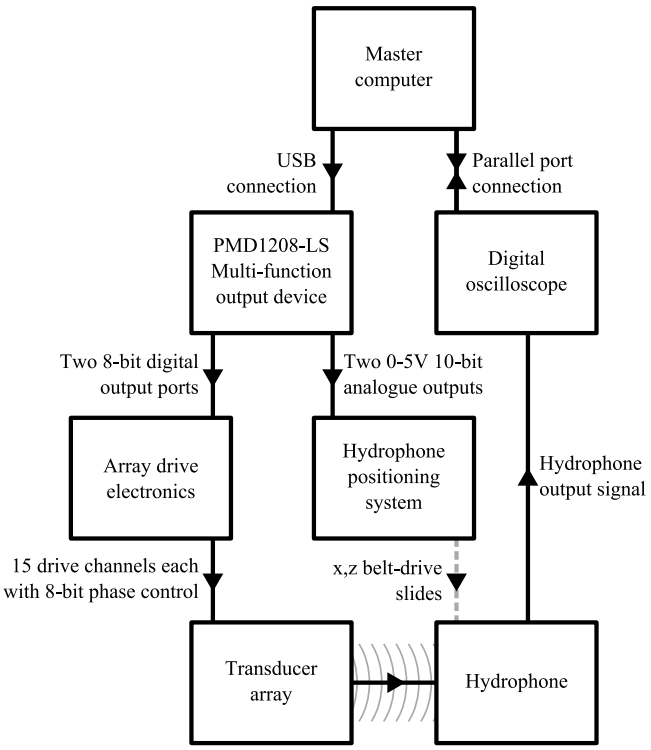

Figure 5.2: A schematic of the experimental apparatus.

plane of the measured field.

The diagram in figure 5.2 illustrates the relationships between the various parts of the system, each of which will now be considered in turn (except for the transducer array which has already been considered in section 4).

Transducer array drive electronics

Two versions of the transducer drive electronics were used throughout the work. A multi-channel version was used for the majority of the work, and a single-channel version was used where higher drive voltages were required.

The multi-channel transducer drive electronics was designed and constructed by Adrian Lovejoy (of the department of Physics, University of Warwick) [Lovejoy et al., 1994]. The electronics provided 15 output channels, each of which produced a 1 MHz, 0-33 V peak to peak square wave to drive an element within an array.

The phase of each channel was programmable with 8-bit resolution, such that the phases were quantised in steps of $\frac{\pi}{128}$ radians. The phases required to produce a focussed field were calculated using a geometrical method where, given the distance from the centre of each element to the focus, appropriate phases were assigned so that the waves from each element produced constructive interference at the focus. This method relied on the assumption that water can be considered as a homogeneous medium with a known speed of sound.

To programme of the phase of each channel, two 8-bit digital output ports (labelled A and B) on the PMD-1208LS were used to interface between the master computer and the transducer array drive electronics. The phases were programmed for each of the 15 channels in turn using the following method:

1. Port A was chosen as the address port, used to specify the address into which the phase information was to be stored in the drive electronics. 4-bits of port A were required to specify the addresses since there were 15 drive channels to be programmed.
2. Port B was the data port, used to specify the phase of the channel. The full 8-bits of port B were used to define the phase.
3. The 8th bit of port A was used as a latch to signal to the drive electronics when to read the address and data bits.
4. For each channel in turn, ports A and B were configured appropriately before the information was latched into the drive electronics using the 8th bit of port A.

This process used 4-bits of port A to specify the addresses for the 15 drive channels and 1 bit as a latch. One further bit of port A was used to instruct the drive electronics to start and stop sending pulses to the transducer array. Figure 5.3 summarises the function of each of the bits within port A.

The output stage of the drive electronics followed the design shown in figure 5.4. One of these stages was required for each of the fifteen channels provided by the multi-channel drive electronics. Within the output stage a FET controlled the

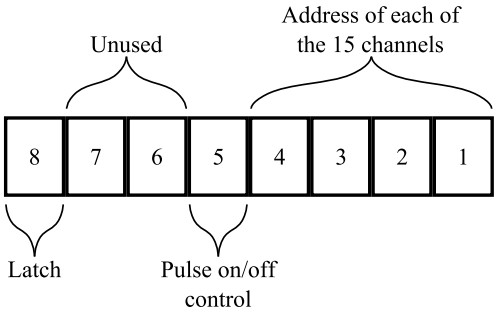

Figure 5.3: The function of each of the bits within port A, the digital output port provided by the multi-function output device (Measurement Computing PMD-1208LS) which was used to control the phased array drive electronics.

output voltage which was applied to the rear face of the PZT element. The FET itself was switched using a 1 MHz square wave whose phase was controlled with 8-bit resolution as described above. With the FET switched off, the voltage at the rear face of the PZT was equal to V_{drive} minus the voltage dropped across resistor R_1, and with the FET switched on, the rear face of the PZT was grounded. The presence of resistor R_1 was necessary to limit the current flowing to ground when the FET was switched on. This design resulted in power being dissipated by R_1 for 50% of the duty cycle, and as a result the multi-channel drive electronics was unable to operate in continuous wave mode without overheating.

The output stage of the single-channel drive electronics followed the same design as figure 5.4, although the power rating of resistor R_1 was increased and a FET capable of handling a higher drain voltage was used to enable safe operation of a single element transducer at voltages of up to 70 V for continuous operation, or up to 280 V for short, user-controlled periods. The single-channel drive electronics thus allowed single elements to be driven at higher voltages than was possible with the multi-channel electronics.

Hydrophone positioning system

The hydrophone positioning system consisted of toothed belt-drive slides arranged in the pattern of an H, as illustrated in figure 5.1, which allowed the hydrophone to be

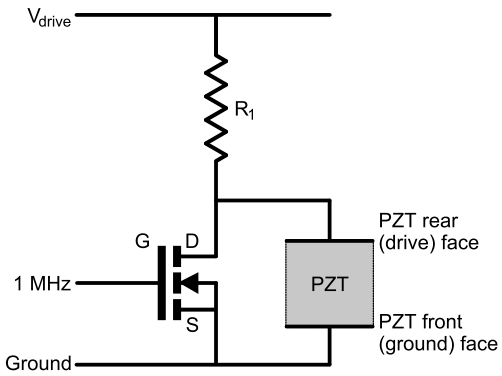

Figure 5.4: The transducer drive electronics output stage. For the multi-channel drive electronics V_{drive} was 40 V, while for the single-channel drive electronics V_{drive} could be varied between 0 and 280 V.

positioned in the x, z plane under computer control. The hydrophone was suspended from a carriage which could be moved in the x-direction along the central slide. The central slide was perpendicular to the two slides upon which it was mounted, and these two slides could be driven in unison to move the central slide in the z-direction. The y plane position was set manually.

Attached to each belt drive slide was a DC motor to provide the drive, and a 10 turn, 10 kΩ, linear potentiometer to provide positional feedback and locate the carriage on the slide. Electronics designed by Adrian Lovejoy (of the department of Physics, University of Warwick) enabled the user to specify any carriage position on each slide by the input of a DC voltage between 0 and 5 V. Using this input voltage and the resistance of the potentiometer as positional feedback, the electronics applied an appropriate drive voltage to the motor to move the carriage to the defined position.

A minimum separation of 8 mm was maintained between the hydrophone and the transducer under test to prevent damage to the hydrophone in the event of contact between the two.

Figure 5.5: The hydrophone, which is composed of a 1 mm diameter needle probe and a submersible pre-amplifier (Precision Acoustics, Dorset, UK).

Multi-function output device

A multi-function output device (Measurement Computing PMD-1208LS) was used to provide the digital and analogue outputs required for the master computer to communicate with the hydrophone positioning system and the transducer array drive electronics. The PMD-1208LS device connected to the master computer via a USB port, and provided a digital to analogue converter (DAC) with two 0-5 V 10-bit analogue outputs, and two 8-bit digital output ports. C++ code was written allowing Matlab to interface with the PMD-1208LS and control these output ports.

The two analogue outputs were used to interface between the master computer and the hydrophone positioning system, to generate the 0-5 V DC voltage required to define the positioning of the belt-drive slides within the positioning system. Since the maximum length of travel of the carriage along each slide was 500 mm and the voltage specifying the carriage position was quantised into 10 bits (or 1024 positions), the positional step-size was 0.49 mm.

The two 8-bit digital output arrays were used to control the array drive electronics, as described earlier.

Hydrophone

A hydrophone was used to measure the ultrasonic pressure at each position in the measurement plane. The hydrophone consisted of a polyvinylidene fluoride (PVDF) 1 mm diameter needle probe and a submersible pre-amplifier (both by Precision

Acoustics, Dorset, UK), as illustrated in figure 5.5. The submersible pre-amplifier was powered by a 28 V DC supply.

The output of the hydrophone was recorded by the measurement system, and was proportional to pressure with its sensitivity having been measured by the manufacturer as 1510.3 mV/MPa $\pm$ 14% at 1 MHz. Applying this calibration factor allowed the pressure to be calculated from the output of the hydrophone.

While using a hydrophone with a smaller diameter would enable field profiles to be taken at a higher spatial resolution, the sensitivity of a hydrophone increases with increasing diameter, with the result that a larger diameter provides a larger signal to noise ratio. A diameter of 1 mm was chosen for the present work since it was not thought necessary to be able to resolve a feature size of less than 1 mm in the ultrasonic field.

Using a hydrophone to measure the ultrasonic pressure amplitude required the assumption that the hydrophone itself did not significantly distort the field. The effect of a needle hydrophone on the measured field was studied using simulation by Huttunen et al. [2003], who concluded that a standing wave could be set up between the source and the hydrophone if the hydrophone diameter was greater than half a wavelength. Although the diameter of the hydrophone used in the present work was $\sim \frac{2}{3}\lambda$, the presence of standing waves was neglected for the following reasons:

1. The amplitude of a standing wave decreases as the separation between the source and the hydrophone is increased. From the results reported by Huttunen et al. [2003], the impact of any standing waves produced by the 1 mm diameter hydrophone used within this project should be negligibly small for hydrophone to source separations greater than about 10 mm.

2. For a standing wave to exist, the face of the hydrophone must very close to parallel to the plane of the ultrasonic source. For example, geometric analysis shows that for a 1 mm diameter hydrophone positioned 15 mm away from an ultrasound source no standing waves will exist if the angle between the plane of the hydrophone surface and the source is greater than 1° , since the reflected beam will lie outside the capture range of the hydrophone surface. The hy-

drophone in our experimental work was aligned with its face approximately parallel to the transducer under test in order to maximise the hydrophone response, since the response is greatest when the face of the hydrophone is perpendicular to the direction of propagation of the ultrasonic wave. However, since the hydrophone was not highly directional it is unlikely that the alignment was within the accuracy required for the existence of standing waves.

3. In the present work, a number of hydrophone readings were averaged to provide a measure of the pressure at each position in the field, and this process should reduce the impact of a standing wave on any individual measurement.

Digital oscilloscope

The measurement system consisted of a digital oscilloscope (Velleman Components, Gavere, Belgium) which was controlled by the master computer via the parallel port. The oscilloscope had 8-bit resolution and a maximum sampling frequency of 32 MHz. The size of the oscilloscope buffer was 4 kb, which enabled 4096 samples to be collected for each measurement. Each oscilloscope measurement therefore enabled data for 128 cycles of a 1 MHz wave to be captured.

C++ code was written allowing Matlab to interface with the oscilloscope and control the oscilloscope settings, the capture of data and the transfer of data to Matlab. When a series of consecutive commands were sent to the oscilloscope, a delay of approximately 170 milliseconds was required between each command to prevent any from being wrongly detected/interpreted by the device. This could otherwise lead to data being recorded at incorrect oscilloscope settings or faulty data transfer between the oscilloscope and the computer.

5.3 Alignment of transducer and hydrophone

For all experimental measurements, the axes were defined relative to the transducer as illustrated in figure 5.6. It was necessary to align the transducer and hydrophone before taking any field profiles so that this co-ordinate system was the same as the

x and z directions defined by the belt-drive slides in figure 5.1.

The transducer under test was held in the tank by a clamp attached to a metal support bar (visible as the white bar at the right hand side of the tank in figure 5.1). The metal support bar rested on the top of the tank, and incorporated several adjustment screws which allowed fine control for positioning the bar. This in turn allowed adjustment of the positioning of the transducer.

Before measuring ultrasonic field profiles for the fifteen element array in the acoustic tank, the transducer was aligned relative to the hydrophone using the iterative procedure described below.

1. The hydrophone was positioned manually at the approximate geometric centre of the fifteen element array, close to the array surface.
2. The array was focussed to the upper limit of its range (to a depth of 100 mm), and a scan of the field was taken in the x, z plane. The hydrophone was then positioned at the focus, and the adjustment screws controlling the rotation of the array about the x and y axes were adjusted to ensure the focal zone lay on the z-axis in the x, z plane.
3. Another scan was taken with the array focussed to the lower limit of its range (to a depth of 60 mm). The hydrophone was then positioned at the focus, and the y-axis position of the hydrophone was adjusted to ensure the focal zone lay on the z-axis in the plane of measurement.
4. Scans were repeated at the upper and lower depths with further adjustments made at each, until the focus lay in the same plane at both depths.
5. Finally, the array was focussed at a medium depth and steered about the y-axis (in this case, to x=10 mm, y=0 mm, z=80 mm), and the adjustment screw controlling the rotation of the array about the z-axis was adjusted to position the focal zone on the x, z plane.

Using this procedure, alignment of the hydrophone and array was relatively straightforward, with the result that the face of the array was perpendicular to the

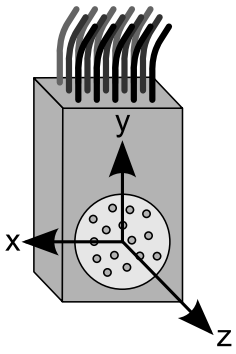

Figure 5.6: The co-ordinate system used for simulation and experimental measurements.

z-axis. By keeping the array fixed at this orientation and adjusting the y-axis setting manually, the hydrophone could also be positioned in front of each element of the array individually for measurement of the field profile of that element.

Alignment of the hydrophone and transducer was more problematic when testing single element transducers that were not part of an array. This was especially true for small diameter elements, such as the 4 mm diameter elements which made up the fifteen element array, since the measured profile of such an element was entirely in the far-field and contained no last axial maximum to use for alignment. However, by maintaining the same settings of the adjustment screws on the support bar as were used for the fifteen element array, the face of a single element could be positioned approximately perpendicular to the z-axis.

5.4 Automated data acquisition

A program was written using Matlab to integrate the interfaces to the array drive electronics, the hydrophone positioning system and the data acquisition equipment, enabling automated measurement of field profiles. The Matlab script written to collect the data from a 2-D profile followed the procedure illustrated in the flow diagrams in figures 5.7 and 5.8.

In step 1, the minimum and maximum x and z co-ordinates which defined

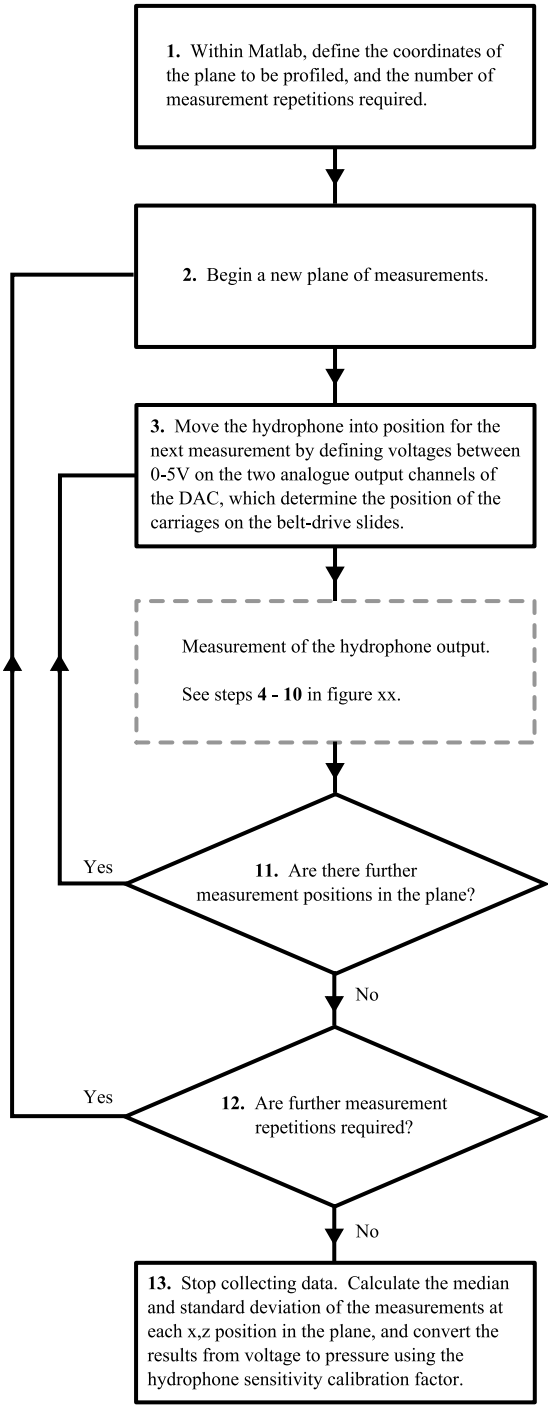

Figure 5.7: A flow chart illustrating the data acquisition procedure for a planar profile.

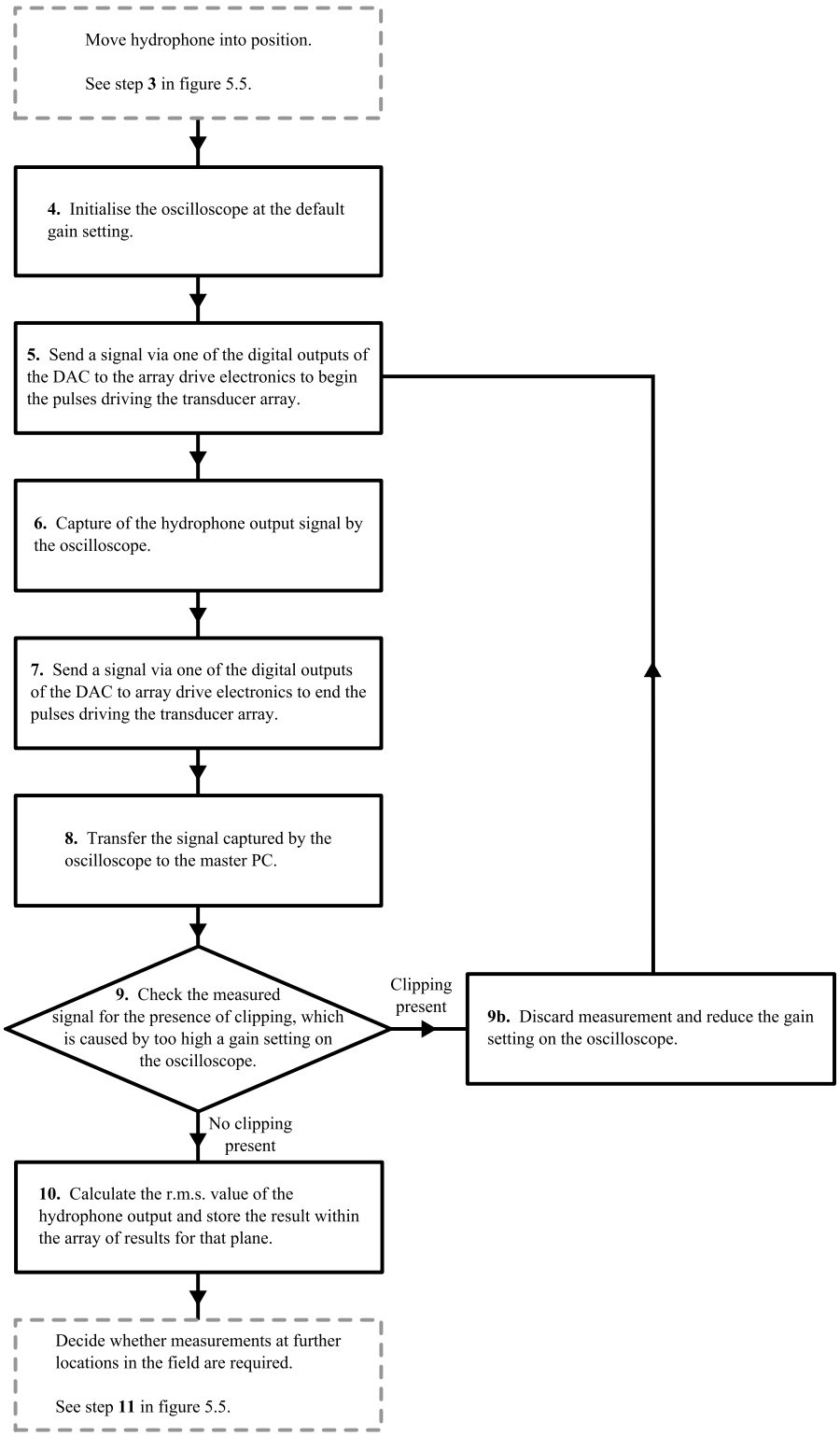

Figure 5.8: A flow chart illustrating the data acquisition procedure for a single location within a plane.

the measurement plane were defined by the user, along with the step size between measurements. The step sizes in the x and z directions were not necessarily the same, but were both multiples of the minimum step size of 0.49 mm. Increasing the step size resulted in fewer measurement points within the plane and reduced the time required to measure the profile.

Each time the hydrophone was moved to a new position in the plane (in step 3), the Matlab script ensured that it approached from the same direction so that the effect of any backlash in the belt-drive slides was constant. A delay were required after each instruction to move the hydrophone to allow time for the hydrophone to be moved and for the water to settle. The length of time required depended on the distance moved, but was typically around 7 seconds for a step between adjacent locations in a plane.

In steps 5 and 7 respectively, signals are sent via one of the digital outputs on the PMD-1208LS to tell the array drive electronics to start and stop sending pulses to the transducer array. This was done to prevent overheating of the drive electronics that would occur if run in continuous wave (CW) mode, since it was only necessary to drive the array during times when the hydrophone was to take a measurement. The mean pulse on-time at each location of a profile was 0.5 seconds. In combination with the delays required for the movement of the hydrophone and for communication with the oscilloscope, the total time required to take a measurement at each location was typically about 8 seconds, with the result that the duty cycle of the array drive electronics was approximately 6%.

In step 6, a short delay was required after applying the pulses to the array before capturing the output of the hydrophone by the oscilloscope so that the detected signal was stable and not part of a start-up transient. However, since two commands were required for the oscilloscope to make the measurement (the first command being to read the signal, and the second to capture it) and a delay of approximately 170 milliseconds was required between each command (as discussed in section 5.2), no additional delay was necessary: the delay inherent in the oscilloscope interface fulfilled the requirement.

In step 12, after all the measurements in the plane had been completed the process was repeated several times allowing the median and the standard deviation of the pressure to be calculated for each position. Measurements were repeated by re-scanning the entire plane (rather than by taking multiple hydrophone readings at each position during the initial scan) to obtain a reliable estimate which may otherwise have been affected by two factors: errors in the hydrophone positioning; and changing environmental conditions, since measurement of a single plane could take up to 14 hours. Scanning of the entire plane was typically repeated at least 5 times.

As can be seen from figure 5.9 the hydrophone output followed a normal distribution, with the result that the median and mean were approximately equivalent. However, extreme values occasionally appeared in the dataset, occurring if the communication interface to the oscilloscope failed, with the resulting reading depending upon which command to the oscilloscope had been mis-interpreted. Although this happened rarely (typically $< 0.1\%$ of the time), the large number of readings per 2-D profile meant that a few spurious results tended to be present in any profile. Since the median was much less sensitive to these extreme values than the mean, the median was used to obtain the average of the multiple readings taken at each position within a profile. The standard deviation was taken for a measure of the uncertainty in the measured pressure at each position.

5.5 Data analysis techniques

Appropriate techniques were required to analyse the data provided by the simulation and experimental measurements, to allow the characteristics of the field to be quantified and comparisons to be made between the data sets. Two particular analysis techniques were used throughout the present work, and these are described in the following sections (5.5.1 and 5.5.2).

The first technique allowed direct comparison to be made between a pair of 2-D fields (one simulated and one measured) by fitting a defined region of the

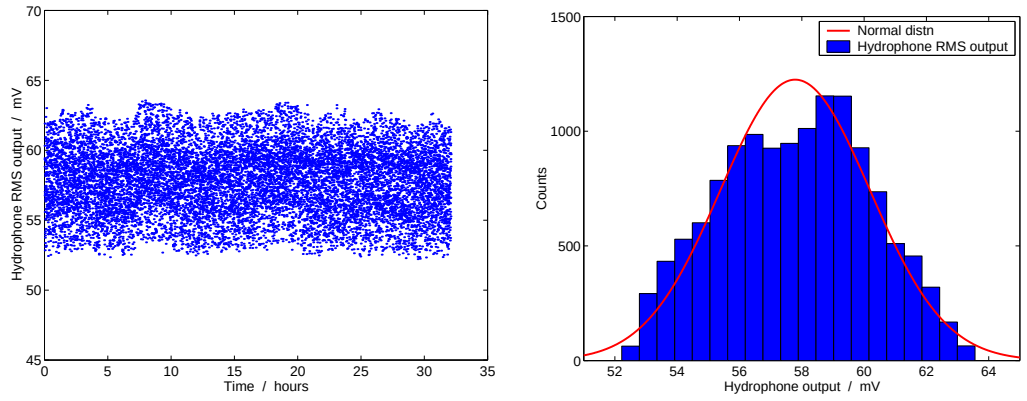

(a) *(b)*

Figure 5.9: (a) Hydrophone output (RMS voltage) against time, showing 13000 measurements taken at a constant position in the far-field of a 10 mm diameter single element PZT transducer. (b) A histogram of the same hydrophone output data. A best fit normal distribution (mean = 57.8 mV, standard deviation = 2.4 mV) obtained by least-squares regression analysis is also plotted for comparison. For the fit, the coefficient of determination $R^2 > 0.99$.

simulated field against the measured field. This allowed comparison both of the intensities within the region, and of the spatial positioning of features within the region to be made.

The focussed fields produced by the fifteen element array contained many localised high intensity maxima between the surface of the array and the focal region. Examples of this will be shown in section 6.4.1 and discussed in detail in section 6.6. The positions and intensities of these maxima were likely to be sensitive to the exact choice of plane through which the field was measured, as well as to variation in the physical and material factors which affect the behaviour of each element in the array. As a result it was impossible for the simulations to reproduce the positions and intensities of these maxima, and the 2-D fitting algorithm was therefore inappropriate for comparison of these regions of the field in the simulated and experimentally measured profiles. A more appropriate method was to analyse the distribution of pressures within the region of interest, and this technique will be described in section 5.5.2.

5.5.1 Field profile fitting algorithm

The experimental measurements from the acoustic tank provided 2-D field profiles of the RMS pressure in the x, z plane from a transducer under test. The simulation software also provided 2-D field profiles of the pressure, computed using the method outlined in section 3.2. However, while the experimental data was in physical units (Pascals), the simulation data was not. Because of this, while making direct comparison between two experimentally measured fields or between two simulated fields was straightforward, comparing an experimental field against a simulated field was not. Using the technique outlined in this section, a scale factor which related the simulated pressures to physical pressures could be found by fitting the simulated field to the experimental field, allowing comparisons to be made between the two.

The algorithm worked by fitting a region of the simulated field against the experimental field using a weighted least squares (WLS) technique as described by Ryan [1997]. This provided a scale factor that allowed the simulation data to be scaled to fit the experimental data, and provided a measure of the goodness of fit in terms of the reduced χ^2 (i.e. χ^2 normalised by the number of points included in the fit).

It was found that fitting the entire simulated field against an experimental field led to a poor correlation for the features of interest (such as the focal zone) since the large background area of the field dominated the fit. Because of this, only a limited window of the simulated field was fitted against the experimental field. For focussed fields, this window was generally limited to a region a few millimetres larger than the -3 dB focal zone.

As noted in section 5.4, extreme values occasionally appeared in the experimental measurements caused by a failure of the communication interface between the master computer and the digital oscilloscope. Although this happened rarely (typically $< 0.1\%$ of the time), the large number of readings per 2-D profile meant that a few spurious results tended to be present in any profile. To prevent this impacting on the fit, the median of the experimental measurements was used rather than the mean, since the median is affected less by any extreme values. While the

presence of an extreme value also increases the standard deviation of a particular experimental value, the impact of this on the fit is small. It results in less weight being placed on that particular point, such that that point has little impact on the overall fit.

The algorithm described here also made it possible to make comparisons between simulated and experimentally measured focussed fields in terms of the spatial position of the focus. This was necessary since, as will be discussed in chapter 6, the position of the focus differed in the measured and simulated fields for the fifteen element array. This analysis was incorporated into the algorithm by performing repeated fits between the experimental and simulation data, with the window of the experimental data being stepped in the x and/or z direction for each fit, and the resulting scale factor and χ^2 value being recorded. The difference in the simulated and measured focal position could then be analysed by finding the position shift required to provide the best fit (minimum χ^2 value) between the simulation and experimental windows.

5.5.2 Rayleigh distribution fitting algorithm

While the field profile fitting algorithm (section 5.5.1) was useful for making comparisons between two 2-D field profiles, there were regions of the field for which this technique is inappropriate. For a phased array transducer, in the region of the field between the array surface and the focal region (which we shall call the near-field of the array) the geometry of the field is complex, with many localised intensity maxima and minima. Modelling these maxima and minima by simulation is extremely difficult since their positions and intensities are sensitive to many factors (including variation in the characteristics of the PZT from which the elements in the array are composed, mounting and matching layer differences, and drive conditions). In addition, in an experimentally measured field the positions and intensities of the localised maxima and minima will be sensitive to the choice of measurement plane. For comparison against a simulated field, the spatial position of the hydrophone for each experimental measurement would have to be known with a precision greater

than that possible with the experimental apparatus used in the present work.

For these reasons, another analysis technique had to be developed for the analysis of this region of the field. By constructing the distribution of the RMS pressures within the near-field of a phased-array, the field could be characterised in a way that did not take the positions and intensities of each of the maxima and minima into account. Fitting of a function to this distribution of pressures then provided a means for quantitative comparison between fields.

The distribution of pressures was considered within this analysis rather than the distribution of intensities. This has no impact on the results since the RMS pressure and the intensity are related by equation 2.15, but it facilitates the analysis since, as will be shown, a simple function exists which can readily be fitted to the pressure distribution.

To obtain the pressure distributions, the region of interest within the field first had to be defined. For the analysis of the fields produced by the fifteen element array (in chapters 6 and 7) this region was defined as the area bounded by the outermost edges of the array, and between the surface of the array and a depth of half the focal distance. The maximum depth was taken as half the focal distance in order to include as much of the near-field as possible while ensuring that the focal region was excluded from the region of interest.

Within this region of interest the pressures were normalised relative to the peak focal pressure, so as to allow straightforward comparison between experimental and simulated field profiles. Following this, the probability density distribution of pressures with the region was constructed, and a function was fitted to it in order that the parameters defining the function could be used as a quantification measure for comparison between multiple distributions. The requirements for this function were that it should meet the following conditions:

1. It should be continuous.
2. It should give good agreement with the pressure distributions obtained from experimental and simulation results.

3. It should be characterised by a small number of parameters (ideally by a single parameter) to allow straightforward comparison between pressure distributions.

Strutt [1880, 1894] showed that a Rayleigh distribution is the proper choice of function to describe the pressure field produced by a large number of vibrations of the same pitch (i.e. frequency) and of arbitrary phase. This function is therefore appropriate to describe the pressure distribution in the near-field of a sparse phased array, since the field is the resultant of a number of incoherent vibrations coming from multiple sources (which are the elements in the array). In addition, this function meets the three requirements listed above.

It should be noted that while it is appropriate to use the Rayleigh distribution to describe the pressure field produced by a large number of vibrations of the same frequency, the experimental array was actually driven with a square-wave drive signal. The Fourier series for a square-wave is composed of a series of harmonic frequencies, and it is therefore possible that the ultrasound field may also contain a range of frequencies. Simulations investigating the potential impact of this are discussed in section 7.2, demonstrating that the impact of square-wave harmonics on the distribution of pressures in the near-field is negligible, and that a Rayleigh distribution remains an appropriate function to model the pressure field.

The probability density function of a Rayleigh distribution is defined by equation 5.1, where $f(r)$ is the probability density of the variable r. The distribution is characterised by a single variable, σ, which corresponds to the mode (i.e. the peak of the function occurs at $r = \sigma$). The Rayleigh distribution is illustrated in figure 5.10 for several values of σ. It can be observed from the figure that increasing σ increases the width of the Rayleigh probability density function. The integral of the Rayleigh distribution (and of any probability distribution) is equal to 1, allowing straightforward comparison to the probability density distribution of the pressures within the near-field region of a phased array since the integral of these was also equal to 1.

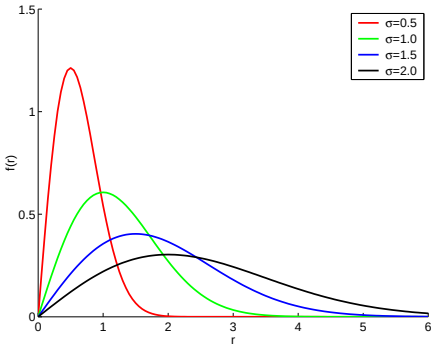

Figure 5.10: The Rayleigh probability density function (equation 5.1) for $\sigma = 0.5$, 1.0, 1.5, 2.0.

$$f(r) = \frac{r}{\sigma^2} e^{\frac{-r^2}{2\sigma^2}} \tag{5.1}$$

Finding an appropriate value for a single parameter, σ, was therefore required to find the best fit between the Rayleigh function and the distribution of pressures in the region of interest. A least squares method was used to do this, and comparison of the obtained values of σ provided a method for quantitative analysis of the near-field region of a phased array.

Discussion of the use of this analysis technique and the results obtained can be found in section 6.6, which describes the results from the fifteen element array, and in chapter 7, which discusses the sensitivity analysis simulations of the fifteen element array.

Chapter 6

Experimental results from the array

6.1 Introduction

In this chapter the experimental results from the fifteen element array are considered. Measurements of the ultrasonic field produced by the individual elements within the array are discussed first, followed by a consideration of inter-element crosstalk measurements, before the measurements of focussed fields are discussed. Throughout the chapter, each experimental profile is compared against simulation, in order to demonstrate the validity of the simulation results and also to identify any areas where the experimental and simulation results differ.

6.2 Characterisation of individual elements

6.2.1 Single element field profiles for a 40 V drive signal

2-D field profiles at the level of the centre of each element in the array were measured to confirm that each element in the array was functional and to allow comparison to the simulation result for a single element. Each profile was measured in the acoustic tank after the array was aligned (following the procedure outlined in section 5.3) such that the profiles included the central axis of each element under test. The elements were driven by a 40 V peak-to-peak square wave using the multi-channel drive electronics (described in section 5.2) in order to replicate the drive conditions

that would be used when operating all fifteen elements as a phased array. When measuring the field from an individual element, that element was driven alone, with all other elements in the array left inactive.

Figure 6.1a illustrates the simulated 2-D intensity profile for an idealised single element of radius 2 mm, where the element is vibrating as an ideal piston at 1 MHz. The theoretical position of the last axial maximum is at $a_{el}^2/\lambda = 2.7$ mm, where a_{el} is the element radius. The near-field region of each element is therefore small relative to the intended focal depth of the array. Since a minimum separation of 8 mm between the hydrophone and transducer was required to prevent damage to the hydrophone, all the experimental measurements were made in the far-field region of an individual element's ultrasonic field.

The experimental measurements showed that nine of the fifteen elements in the array matched the simulation profile reasonably well, while the other elements showed poor agreement. Figure 6.1a shows the simulated intensity profile from a single element, while figure 6.1b shows a typical experimental profile of an element having good agreement with the simulated profile. Figure 6.1c shows an example profile of an element having poor agreement with the simulated profile, where the intensity was skewed to the side. Each of the six elements with poor agreement to the simulated profile showed similar asymmetric intensity profiles to that seen in figure 6.1c.

Despite the variation seen in the shape of the experimental 2-D intensity profiles, the 1-D profiles along the central axis of each element all had a similar shape, although the intensities varied by up to a factor of 4 at the intended focal depth of 60 to 100 mm. Figure 6.1d compares the experimental 1-D profiles along the central axis of each of the fifteen elements to the simulated profile, showing the difference in the intensities produced by the fifteen elements. This variation was still seen when the elements showing poor agreement with the 2-D simulated profiles were excluded.

The skewed intensity profiles observed in figure 6.1b,c may be a result of the array's construction process. The epoxy used for the matching layer was of very

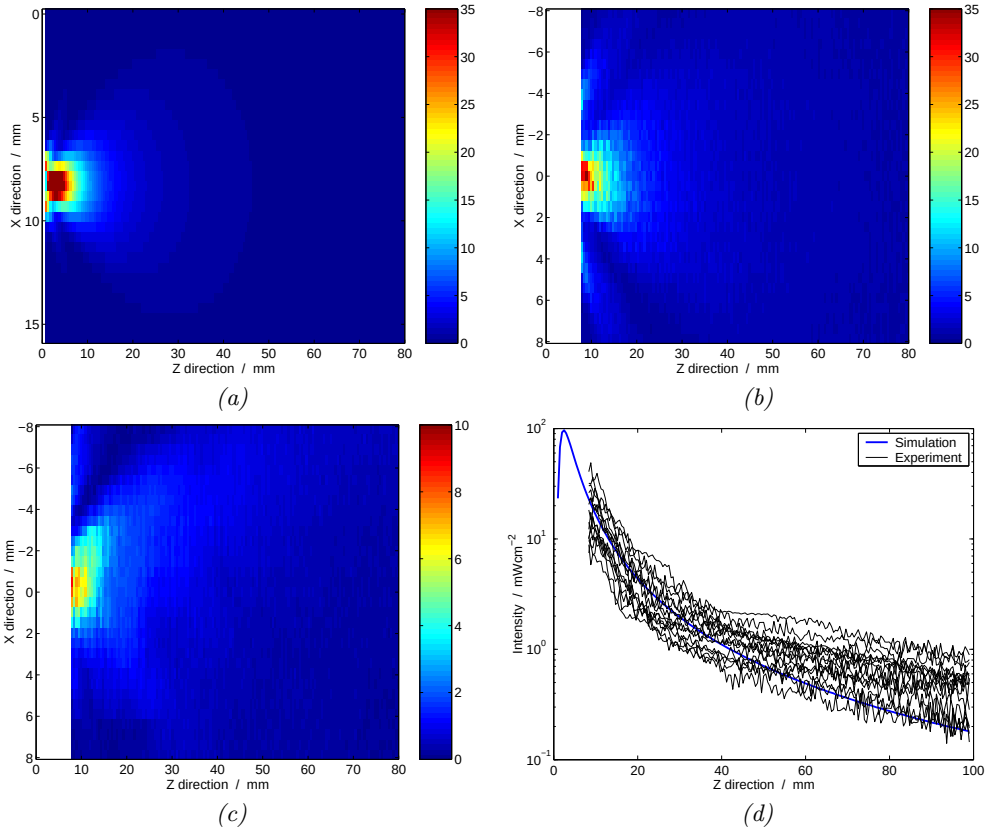

Figure 6.1: (a) Simulated 2-D intensity profiles of a 2 mm radius single element. (b) Experimental 2-D intensity profile of a typical element showing good agreement with simulation. (c) Experimental 2-D intensity profile of a typical element showing poor agreement with simulation. (d) 1-D simulation and experimental intensity profiles along the z axis of each of the 15 elements in the array. The absence of experimental data close to the array surface is due to the minimum separation of 8 mm maintained between the hydrophone and transducer. The colours in plots a,b,c indicate the intensity in $mWcm^{-2}$.

low viscosity, such that it seeped between the sides of the PZT and the perspex frame. However, air bubbles were occasionally trapped between the PZT and the frame, with the result that certain elements were not bound symmetrically to the frame, potentially causing the asymmetric field profiles that were observed for certain elements in the array. Further construction trials were carried out on single element transducers and it was found that skewed profiles were absent in transducers where the diameter of the hole in the perspex frame was increased slightly (by approximately 1 mm), thereby eliminating the formation of air bubbles between the PZT and the frame, and ensuring symmetrical bonding of each element. However, clamping of the PZT edge by the epoxy bonding is likely to restrict movement at the edge and promote non piston-like vibrational modes, thereby affecting the geometry of the field [Dekker et al., 1974]. It was not possible to verify this in the acoustic tank, since the entire near-field region for a single element lay within the region that was too close to the transducer surface to be measured without risking damage to the hydrophone by knocking it against the transducer surface.

A number of factors could be contributing to produce the large variation in the outputs of the individual elements in the array seen in figure 6.1d. According to the specifications for the grade of PZT used in the array (listed in table 4.1) the PZT parameters may vary quite considerably between elements in the array. The specifications for Navy type III PZT allow the piezoelectric coefficient d_{33} to vary by $\pm$ 15%, which will impact on the amplitude of the pressure wave produced by each element. Since intensity is proportional to the square of the pressure amplitude, the intensity output by an element could therefore vary by $\pm$ 32% due to this parameter alone. In addition, the elements in the array were driven at 1 MHz, a frequency close to their specified resonant frequency. According to the PZT specifications in table 4.1, the frequency constant (and hence the resonant frequency) may vary by $\pm$ 8% between each of the elements in the array, and this could potentially have a large impact on the output of each element. In addition to this inherent variation in the PZT parameters, differences in the mounting of each element within the array and variation in the performance of each output channel from the drive electronics

will affect the ultrasonic output of each element.

The existence of this large range in the output of each element is therefore reasonable given the large number of contributory factors. To minimise the variation in output between elements would require drive electronics with a programmable drive voltage amplitude for each channel, which was outwith the scope of the present work.

6.2.2 Single element far-field intensity as a function of drive voltage

It is important to understand the impact of the drive conditions upon the field produced by a single element, as this will shed light on the impact of the drive conditions on an array of elements. Measurements were therefore made of the field produced by an individual element to look at the relationship between the output of an element (in particular, the intensity at a point in the far field) and the drive voltage. One of the elements that showed good agreement with the simulated profile was selected for these measurements. The single-channel drive electronics (discussed in section 5.2) was used to provide the drive signal to the element, thus allowing a square wave of up to 280 V peak-to-peak to be applied.

Figure 6.2 illustrates the results, showing that the intensity measured at a point in the far-field increased with the square of the drive voltage. It can be noted from the figure that there are two slight discontinuities in the measured data (labelled A and B in the figure), such that three measurements (at 180, 200 and 220 V) lie below the best fit line. At A and B the voltage supply to the drive electronics was switched between low, medium and high voltage equipment, and these changes were the source of the discontinuities.

Measurements of the 2-D field produced by a single element were also made for drive voltages of greater than 40 V peak-to-peak, to look at whether increasing the drive voltage had any impact on the field geometry. The maximum applied drive voltage for these measurements was 70 V peak-to-peak, since that was the maximum that could be supplied by the single-channel drive electronics under continuous operation. Results showed that the geometry of the field remained unchanged for

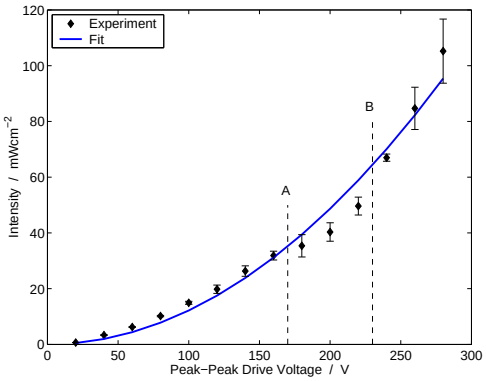

Figure 6.2: Mean and standard deviation of the intensity at a point in the far field of a single element of radius 2 mm over different drive voltages. The measurements were taken at a depth of 40 mm from the element surface. The drive voltages here represent the peak to peak voltage of the square wave drive signal. The fit shows that the intensity increases with the square of the drive voltage. The labels A and B denote the voltages at which the voltage supply to the drive electronics was switched between low, medium and high voltage equipment.

the higher drive voltages, and that only the intensities in the field were increased.

These results are consistent with what would be expected given the characteristics of PZT and the structure of the field from a circular piston source. Application of an electric field across a PZT element produces a strain which is proportional to the electric field strength, as characterised by the parameter d_{33} (section 2.1). As a result, both the amplitude of vibration and the pressure amplitude at the surface of the PZT element also increase linearly with the strength of the applied electric field. According to equation 2.6 the pressure amplitude at any position in the field is proportional to the pressure amplitude at the surface of the vibrating source, and therefore the intensity at all points in the field increases with the square of the applied electric field strength (equation 2.15).

6.3 Inter-element cross-coupling

In any ultrasound array the behaviour of one element can affect the other elements in the array via inter-element cross-coupling, which can arise due to either acoustic

or electric crosstalk [Mo et al., 1992]. Cross-coupling is particularly important for arrays intended for medical imaging and non-destructive testing purposes where the sensitivity of the individual elements is important to allow small signals to be resolved adequately, and it is in these areas that much of the work of others has been focussed. However, inter-element cross-coupling also affects the function of a therapeutic array, since the geometry of the field depends upon the behaviour of the elements in the array. For example, Dias [1982] and Assaad and Bruneel [1997] reported that crosstalk affects the directivity pattern of individual elements (which was defined by equation 2.14 in section 2.3), and this will affect the geometry of the field produced by an array of sources.

Various methods for minimising the crosstalk in phased arrays have been proposed, including designing the electrical interconnections in such a way as to minimise electrical crosstalk [Sokka and Hynynen, 2000], incorporating some form of physical separation between elements to minimise acoustic crosstalk [Ritter et al., 2002] and modifying the drive signal to each element to actively cancel the effects of crosstalk [Zhou et al., 2003]. The design of the fifteen element array used in the present work (section 4) included separate matching layers for each element and electrical shielding of the signal lines to minimise crosstalk in the array. Within this section experimental measurement of the crosstalk within the array is described.

6.3.1 Crosstalk measurements for a 40V drive signal

Crosstalk measurements were made on the fifteen element array by driving a single element in continuous-wave mode using the multi-channel drive electronics (i.e. a 40 V peak-to-peak square waveform) and measuring the resulting electrical signal on each of the undriven elements using the digital oscilloscope. The measurements were made with the array firing into a water medium. Measurements of the crosstalk between element pairs were made for a subset of 98 of the 210 (15×14) possible combinations of drive/receive element pairs, and the results were analysed to investigate whether there was a relationship between the magnitude of the cross-coupling and the separation between elements. The inter-element pitch, defined as the dis-

tance between the centres of the drive and receive elements, was used as a measure of the element separation. For the fifteen element array the inter-element pitch ranged between 9 and 39 mm, depending on the particular pair of elements selected.

Figure 6.3a shows the square-wave drive signal (line *i*) and the waveforms for crosstalk signals measured on three different element pairs in the fifteen element array (lines *ii*, *iii* and *iv*), with their phases shown relative to the square-wave drive signal. A number of observations can be made from this figure:

- The measured crosstalk signals are not sinusoidal. Instead, they consist of high frequency bursts, with the start of each burst occurring at the same time as each rise and fall of the square-wave drive signal. The shape of the crosstalk waveforms looks like that of a high frequency, high-Q resonant system which is caused to ring in time with the sharp rise and fall of the square-wave drive signal.
- The phase of the measured crosstalk signals is the same for each choice of element pairs, indicating that the phase of the waveform is independent of the element separation. This strongly suggests that the measured crosstalk signals are not a result of acoustic coupling, since the time required for an acoustic wave to travel between elements would depend on the element separation and would therefore result in different delay times for each element pair.

Figure 6.3b plots the RMS of the measured crosstalk signal against the inter-element pitch for each pair of elements measured. It can be seen from the figure that there is only a small change in the magnitude of the cross-coupling over the full range of inter-element pitches. The solid line represents the least squares linear fit through the data, and indicates that the cross-coupling is slightly stronger for closely spaced elements than for widely spaced elements. The 95% confidence band for the fit (calculated using the method described by Lohninger [1999]) is indicated by the dashed lines. The confidence band confirms that the change in the magnitude of the cross-coupling with inter-element pitch, although small, is statistically significant since a horizontal best-fit line, indicating no relationship between crosstalk and

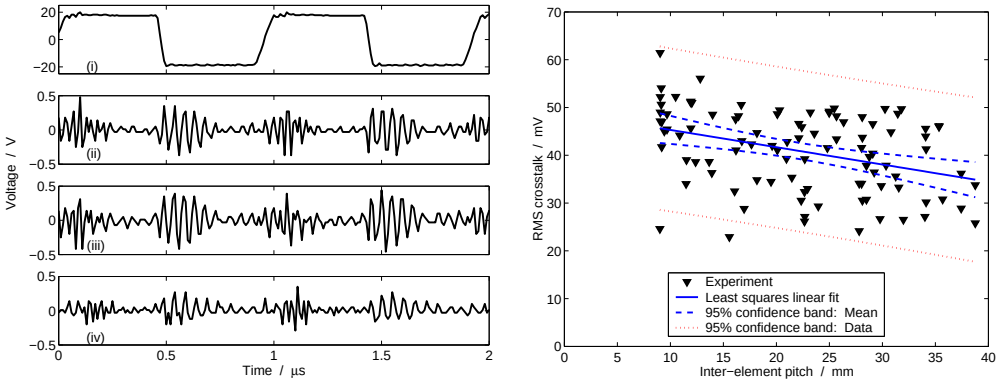

(a) *(b)*

Figure 6.3: Experimental measurements of the crosstalk for the fifteen element array. In plot (a), line i *shows the square-wave drive signal while lines* ii, iii *and* iv *show measured crosstalk waveforms for three different element pairs plotted relative to the drive signal. The inter-element pitch for the three element pairs was: (*ii*) 11.9 mm, (*iii*) 31.1 mm and (*iv*) 10.5 mm. In plot (b), the measured RMS crosstalk signal is plotted against the separation of the drive and receive elements.*

inter-element pitch, cannot be contained within the band. While this confidence band relates to the mean predicted crosstalk, the dotted lines represent the 95% confidence band for the individual data. This confidence band demonstrates how weak the relationship between cross-coupling and inter-element pitch is, since the variation in the individual data is much greater than the change in the mean with element separation.

Measurements by Smith et al. [1991] of the acoustic crosstalk in a 2-D array for medical imaging indicated that acoustic crosstalk is strongly dependent on element separation. The fact that the magnitude of the measured crosstalk in the present work was almost independent of inter-element pitch provides further evidence that the cross-coupling in the fifteen element array was primarily due to electrical coupling between drive lines rather than acoustic coupling between PZT elements.

From figure 6.3a, it can be observed that the maximum RMS crosstalk signal measured on the 15 element array was approximately 62 mV, which is slightly less than 0.5% of the 40 V peak-to-peak drive signal. As such, the impact of cross-

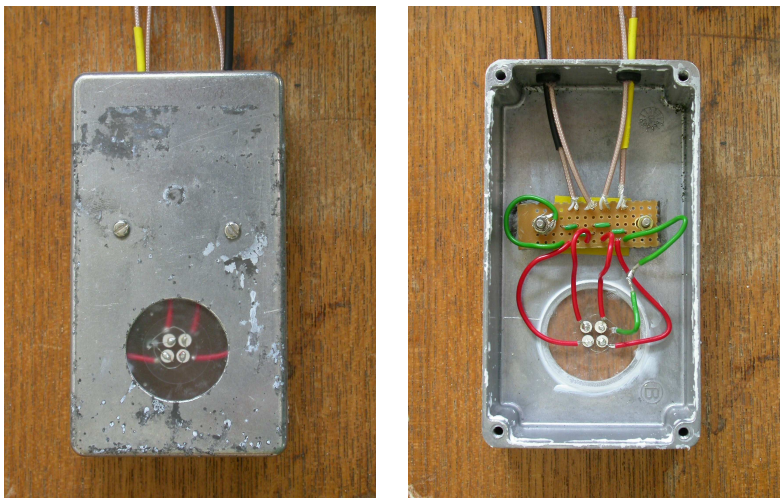

(a) *(b)*

Figure 6.4: The four element array. (a) External. (b) Internal.

coupling on the function of the array would be expected to be small.

6.3.2 Crosstalk measurements for closely spaced elements and high drive voltages

While the results indicated that cross-coupling is weak within the fifteen element array when driven by a 40 V waveform, questions remained as to whether the cross-coupling would be significantly worse for more closely spaced elements and for higher drive voltages. This is important since (as will be discussed in section 8) both a larger number of elements (and therefore closer element spacings) and higher drive voltages would be necessary to create a focal region of sufficient intensity to produce mild hyperthermia in tissue. To allow the crosstalk between more closely spaced elements to be measured, a new transducer array was constructed which was composed of four closely spaced 4 mm diameter elements with a minimum inter-element pitch of 4.4 mm (figure 6.4).

Measurements of the crosstalk in the four element array were made using the same procedure as was used with the fifteen element array. Figure 6.5a shows the 40 V peak-to-peak square-wave drive signal (line i) and the waveforms for crosstalk

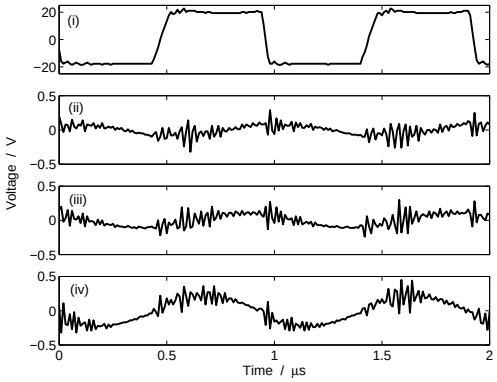

Figure 6.5: Typical measured crosstalk waveforms for three different element pairs from the 4 element array. Line i *shows the square-wave drive signal while lines* ii, iii *and* iv *show measured crosstalk waveforms for three different element pairs plotted relative to the drive signal. The inter-element pitch for the three element pairs was: (*ii*) 4.5 mm, (*iii*) 5.9 mm and (*iv*) 4.4 mm.*

signals measured on three different element pairs in the four element array (lines *ii*, *iii* and *iv*), with their phases shown relative to the square-wave drive signal. A number of observations can be made from these two plots:

- As with the fifteen element array (figure 6.3a), short, high frequency bursts are present, occurring at the rise and fall of the square-wave drive signal. For each choice of element pairs, these bursts always occur at the same time relative to the drive signal, and it is therefore likely that these are due to electrical cross-coupling, as described in section 6.3.1.
- The measured crosstalk signals also contain a 1 MHz sinusoidal component. The phase of this sinusoidal component is different for each each combination of element pairs, strongly suggesting that it is a result of acoustic coupling between elements, since the time required for the acoustic wave to propagate between elements will depend on the element separation and will therefore be different for each choice of element pair.

Since the crosstalk measurements only required a single active drive channel, measurements were also made while using the higher voltage single-channel

drive electronics (described in section 5.2) to provide the drive signal, enabling the crosstalk to be measured for drive signals up to 280 V peak-to-peak. Figure 6.6a illustrates the combined results for the fifteen element and four element arrays using drive voltages of 40 V and 280 V (peak-to-peak square waveforms). The graph shows that for the fifteen element array and drive voltages of 280 V peak-to-peak, the relationship between the magnitude of the crosstalk and the inter-element pitch is similar to the trend that was seen for a 40 V drive waveform: the crosstalk decreases very weakly with increasing inter-element pitch. However, for element pairs in the four element array (where the inter-element pitch is smaller) the magnitude of the cross-coupling is strongly dependent on pitch, indicating that acoustic crosstalk dominates at these smaller element spacings (i.e. for element pairs with an inter-element pitch of less than approximately 8 mm). This was true both for drive voltages of 40 V and of 280 V.

Further measurements of the crosstalk were made at intermediate voltages between 40 V and 280 V, and in figure 6.6b the magnitude of the crosstalk is plotted as a function of the drive voltage. For large inter-element pitches (15-30 mm), the crosstalk rose approximately linearly with voltage beyond a drive voltage of 80 V. For small inter-element pitches (4-5 mm) a similar linear increase in the crosstalk with the drive voltage is seen, but the variability of the measured crosstalk is much greater. This large variation suggests that mounting differences between elements are significant in determining the acoustic crosstalk between element pairs.

Although figure 6.6 shows that the measured crosstalk signals were much stronger for closely spaced elements and high drive voltages, the magnitude of the cross-coupling was still relatively weak in comparison to the drive signal. At the minimum inter-element pitch of 4.5 mm and the maximum drive voltage of 280 V the maximum measured RMS crosstalk signal was approximately 1.2 V, which was less than 1.5% of the 280V peak-to-peak drive signal.

In summary, the results indicate that the crosstalk within an array of this type is weak. Cross-coupling between widely spaced elements (where the pitch is greater than about 8 mm) is primarily due to electrical coupling and takes the form

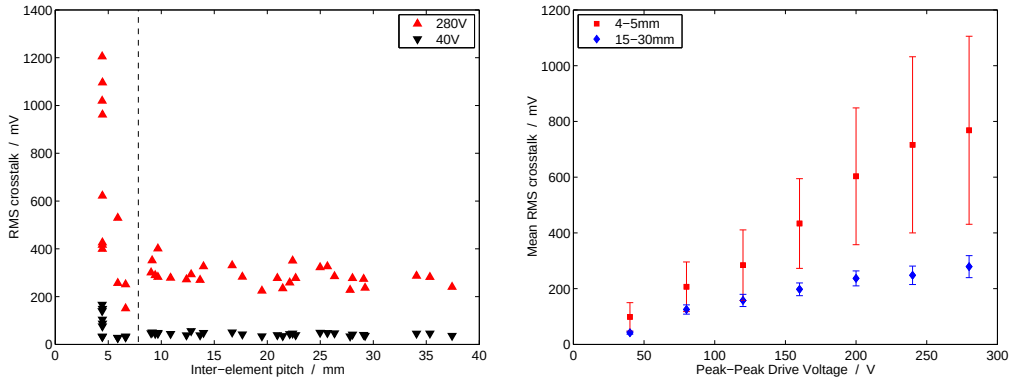

Figure 6.6: Plot (a) shows the measured RMS crosstalk signal against the separation between the drive and receive elements for drive voltages of 40 and 280 V. The data obtained from the fifteen element array are found to the right of the vertical dashed line, while the data obtained from the four element array are found to the left of the line. Plot (b) shows the mean RMS crosstalk signals against drive voltage for element separations within the ranges 4-5 mm and 15-30 mm.

of short, high frequency bursts initiated by the sharp rise and fall of the square-wave drive signal. The strength of this crosstalk is typically less than 0.5% of the drive signal. It will therefore have little influence on the phase of the drive signal at the receiving element. Cross-coupling between closely spaced elements (where the pitch is less than about 8 mm) is more significant and is primarily due to acoustic coupling. The measured waveform for this acoustic crosstalk was sinusoidal.

Acoustic coupling between elements could arise from one of two mechanisms: via transmission of a pressure wave propagating through the Perspex frame, or via a Lamb wave travelling on the surface of the Perspex. The actual mechanism by which acoustic coupling occurred in the four element array has not been identified within the present work. Since the level of the acoustic crosstalk was at most approximately 1.5% of the drive signal, its impact is likely to be small and therefore further investigation of the crosstalk mechanism was not required. However, in arrays composed of a large number of elements it is possible that a small level of crosstalk could impact on the performance of the array, and so simulations investigating this are considered in chapter 7.

6.4 Field profiles of the array focussed on-axis

6.4.1 Focussed field profiles with all 15 elements activated

2-D profiles of the ultrasonic field produced by the fifteen element array were measured in the acoustic tank with the array focussed to a number of different focal depths. The multi-channel drive electronics were used to drive the array for these measurements, driving each element with a 40 V peak-to-peak 1 MHz square wave. Simulations were performed with the same setup as used for the experimental measurements (i.e. with the array focussed to the same focal depth and the pressure field being computed in the same plane as in the experimental measurements) to provide simulated results against which the experimental data could be compared.

The phase differences required to focus the array were calculated using the geometrical method outlined in section 3.2.1 for both the simulation and experimental fields.

Before comparisons could be made between the experimental and simulation results, the simulation data had to be fitted against the experimental data using the field profile fitting algorithm (section 5.5.1) to obtain the scale factor required to convert the simulated pressures into physically meaningful units (Pa). Once scaled, it was then possible to compare the simulations against the experimental data.

2-D plots of both the simulated and measured data are shown in figure 6.7 for phase-defined focal depths of 60, 80, and 100 mm. From these 2-D profiles, the intensities along a line can be plotted to produce 1-D intensity profiles. For the case where the array was focussed to a depth of 80 mm, figure 6.8 shows the simulated and measured 1-D intensity profiles along the central axis of the array (a,c,e), and through the focal region perpendicular to the central axis of the array (b,d,f). In the experimental profiles (both 2-D and 1-D) the absence of data close to the array surface is due to the minimum separation of 8 mm maintained between the hydrophone and transducer to prevent damage to the hydrophone (section 5.2).

The measured profiles demonstrate that the array was capable of producing focussed ultrasound fields, and is tolerant of the variation between individual ele-

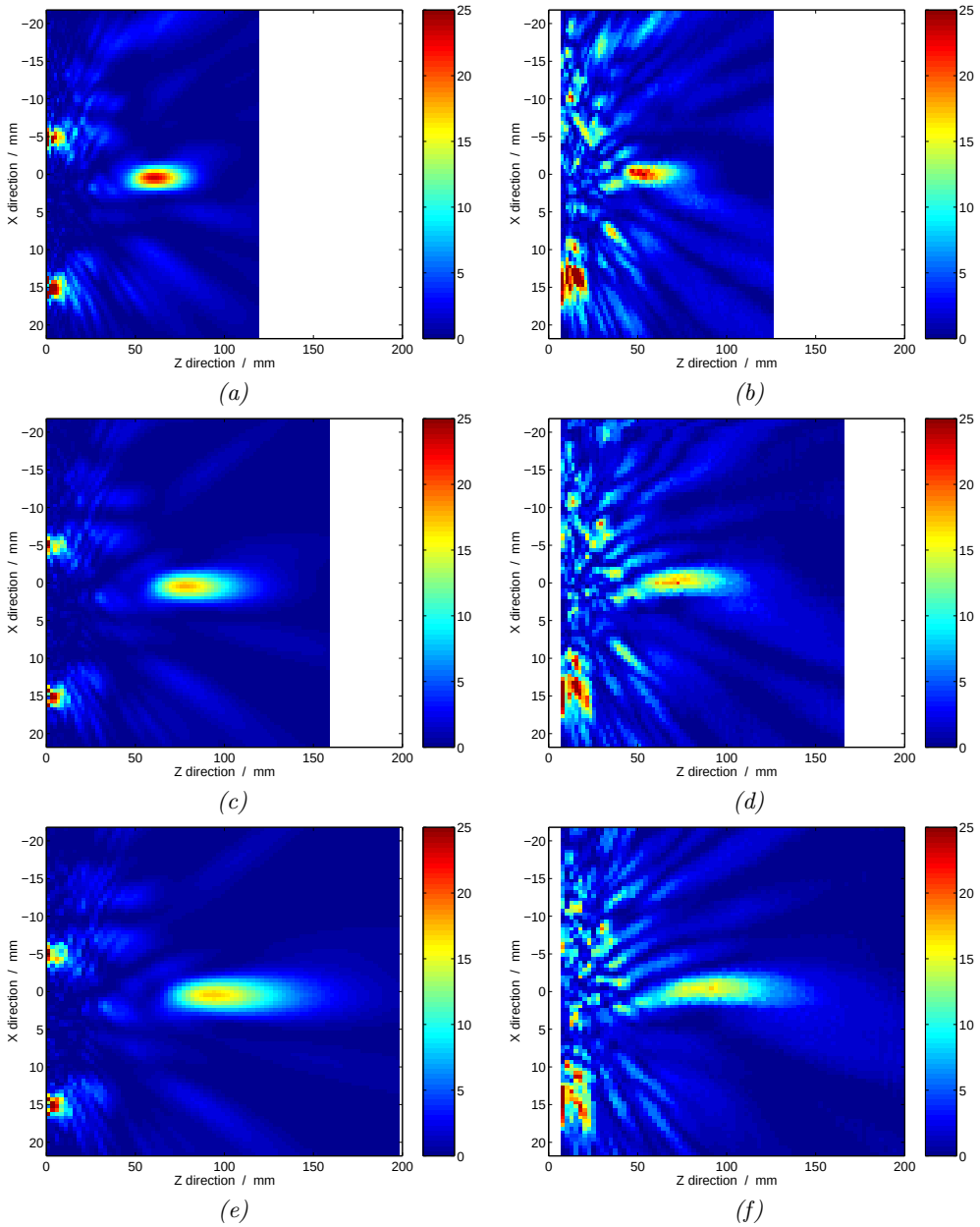

Figure 6.7: Intensity profiles with the array focussed at depths of (a,b) 60 mm, (c,d) 80 mm and (e,f) 100 mm. The left-hand plots (a,c,e) show the 2-D simulation results and the right-hand plots (b,d,f) show the 2-D experimental measurements. The array is positioned at the left hand side with the ultrasound propagating left to right. The colours indicate the intensity in $mWcm^{-2}$.

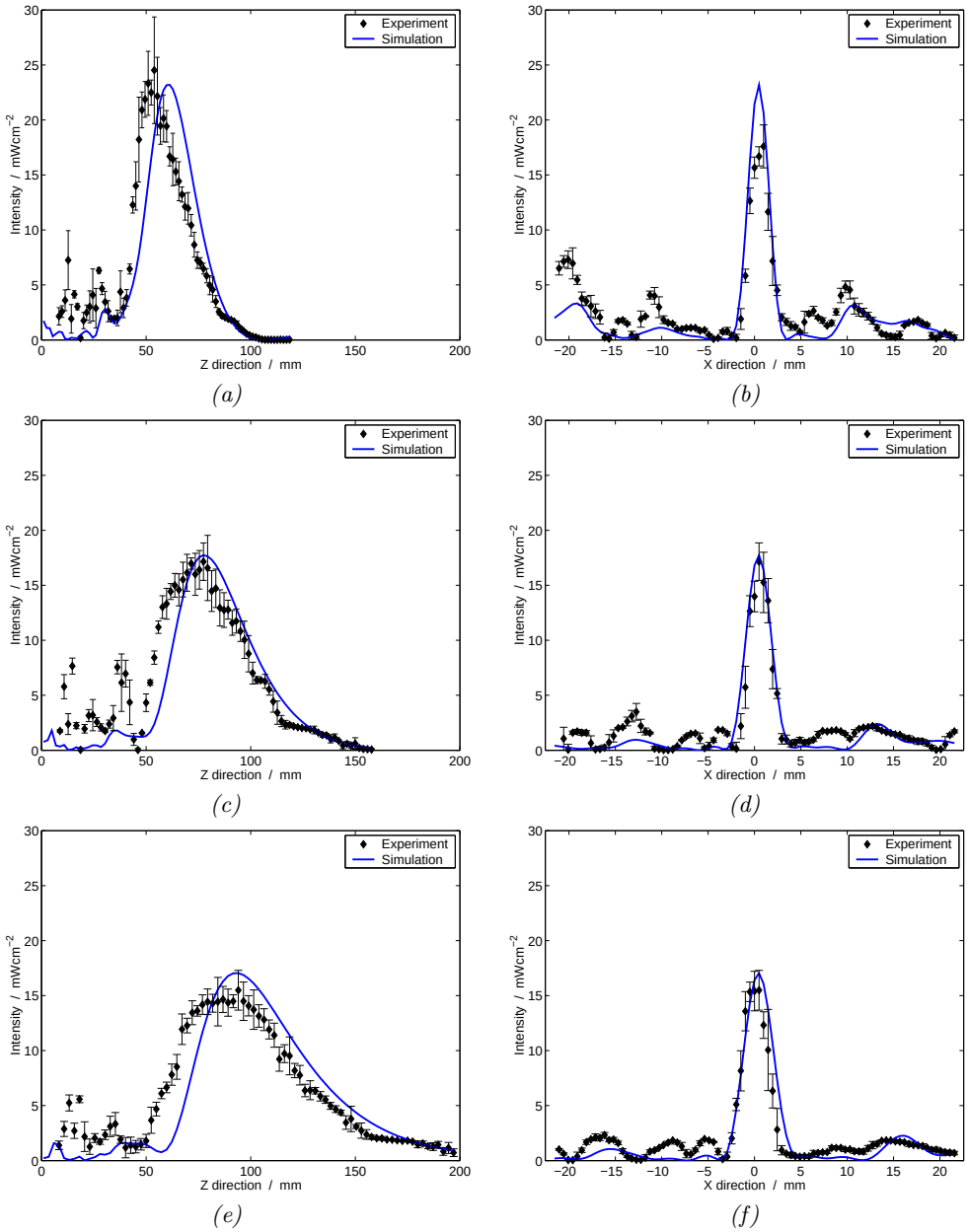

Figure 6.8: Intensity profiles with the array focussed at depths of (a,b) 60 mm, (c,d) 80 mm and (e,f) 100 mm. The left-hand plots (a,c,e) show the simulated and measured intensities along the central axis of the array and the right-hand plots (b,d,f) show the simulated and measured intensities in the x direction through the focus.

ments discussed in section 6.2. The 1-D profiles (figure 6.8) show that there was good agreement between the shape of the simulated and measured profiles at the focus, although the position of the focus in the experimental profiles was about 7 mm nearer the transducer than in the simulated profiles.

The asymmetric fields produced by several of the individual elements (such as that shown in figure 6.1c where the profile is skewed to one side) are limited to depths of less than about 20 mm. Beyond this depth the field from each individual element is approximately symmetric. These skewed profiles therefore do not affect the field at the focal regions of the array since they were located at depths of 60 to 100 mm.

In figure 6.7a,c,e two high intensity regions are visible near the surface of the array in the simulated fields. In the 2-D experimental profiles high intensity regions are found at these two locations, with the region at $x = 15$ mm much more prominent than that at $x =$ -5 mm. These regions are located directly in front of two elements which are in the same plane as the field profile. In an attenuating medium, these high intensity regions will produce heating directly in front of each element. As a consequence of the relatively small number of elements, the intensity of these regions for the fifteen element array is greater than the intensity of the focal region. In fact, it is likely that the maximum intensity in front of each element actually lies within the 8 mm region at the surface of the transducer, and is somewhat greater than the values obtained at the minimum depth of 8 mm. These high intensity regions directly in front of each element could potentially impose a serious limitation on the clinical use of the array because of the heating that would be be produced at the surface of the tissue. This is particularly important since the use of an array is likely to involve scanning of the focus around the tumour volume (section 1.3). As a result, over the course of treatment the average intensity received at the tumour will be somewhat less than the actual focal intensity. In contrast, the high intensity regions at the surface and directly in front of each element will remain in a fixed position throughout the treatment.

There are a number of ways in which the impact of these high intensity

Table 6.1: Comparison of the peak focal intensities obtained from experimental measurement and simulation for the fifteen element array at focal depths of 60, 80 and 100 mm. The scaling of the simulation data has been based on the fit to the experimental data at a focal depth of 60 mm.

Focal distance mm	**Peak focal intensity** $mWcm^{-2}$	
	Experiment	Simulation
60	23.1 $\pm$ 3.0	23.1
80	19.7 $\pm$ 2.1	22.4
100	15.9 $\pm$ 1.3	19.2

regions directly in front of each element could be minimised. Reducing their intensity relative to the focal intensity could be accomplished by increasing the number of active elements in the array. However, heating in the region of the medium in contact with the array is also caused by heat conduction from the PZT elements, since the temperature of these increases when the elements are driven. To overcome this issue, several workers have produced arrays which incorporate a laminar flow layer at the front surface of the transducer [Diederich and Hynynen, 1999; Nau et al., 2000], providing cooling of both the array and the tissue surface. Lin et al. [1999] have indicated that surface cooling of the tissue may help in reducing heating at depths of up to approximately 20 mm. An advantage of applying a laminar flow layer to the array considered in the present work would be that the high intensity regions in front of each PZT element would lie almost entirely within the flow layer.

The peak focal intensities and the -3 dB lengths and widths of the focal region are summarised in tables 6.1, 6.2 and 6.3 respectively, demonstrating the good agreement that was seen between the experimental measurements and the simulated fields for these parameters.

Table 6.2: Comparison of the -3 dB focal lengths obtained from experiment and simulation for the fifteen element array at focal depths of 60, 80 and 100 mm.

Focal distance mm	**-3 dB focal length** mm	
	Experiment	Simulation
60	26.5 ± 0.7	26.5
80	43.1 ± 1.0	39.2
100	61.2 ± 1.2	56.4

Table 6.3: Comparison of the -3 dB focal widths obtained from experiment and simulation for the fifteen element array at focal depths of 60, 80 and 100 mm.

Focal distance mm	**-3 dB focal width** mm	
	Experiment	Simulation
60	2.2 ± 0.2	2.5
80	3.2 ± 0.2	3.7
100	2.9 ± 0.2	3.2

6.4.2 Focussed field profiles with a limited subset of elements activated

Measurements were made to investigate the relationship between the focal intensity and the number of active elements in the array. For these measurements, the array was focussed to a depth of 80 mm and the hydrophone was positioned at the focal peak. Measurements of the focal intensity were made for eleven different subsets of active elements, consisting of five through to fifteen randomly selected elements. No measurements were made with fewer than five active elements.

Figure 6.9 plots the measured and simulated peak focal intensities against the number of active elements in the array. The simulated intensity increased with the square of the number of elements, and the measured data followed this trend. However, there is a discontinuity in the graph where the measured intensity for nine and ten active elements was actually lower than the measured intensity for an array

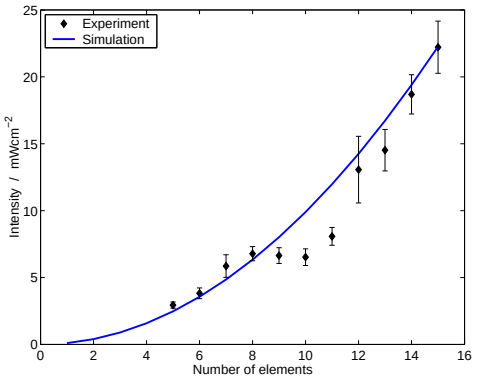

Figure 6.9: Peak focal intensity against the number of elements in use, with the array focussed at a depth of 80 mm. The error bars indicate the standard deviation of the experimental measurements. The intensity increased with the square of the number of elements, as predicted by simulation.

with only eight active elements. This resulted from the fact that the driven elements were chosen randomly, and the selected elements for these unexpectedly low data included a number of the array's lower output elements. Despite this, the overall trend was that the intensity increased with the square of the number of elements, in good agreement with the simulation.

6.5 Field profiles of the array focussed off-axis

6.5.1 Off-axis focussed fields: Position of the focal region

The measurements on focussed fields discussed so far have only concerned the case where the field is focussed on the central axis of the array. Further measurements were made of fields focussed at a depth of 80 mm and steered away from the central axis by 0, 10 and 20 mm, and the 2-D field intensity profiles for these are shown in figure 6.10 in comparison to the simulated profiles. Figure 6.11 shows 1-D profiles through the foci in the x and z directions.

It can be seen from figure 6.10 that the depth of the focal region was closer to the array surface in the experimental results than in the simulations, corroborating the observation from fields focussed on the central axis of the array (section 6.4.1).

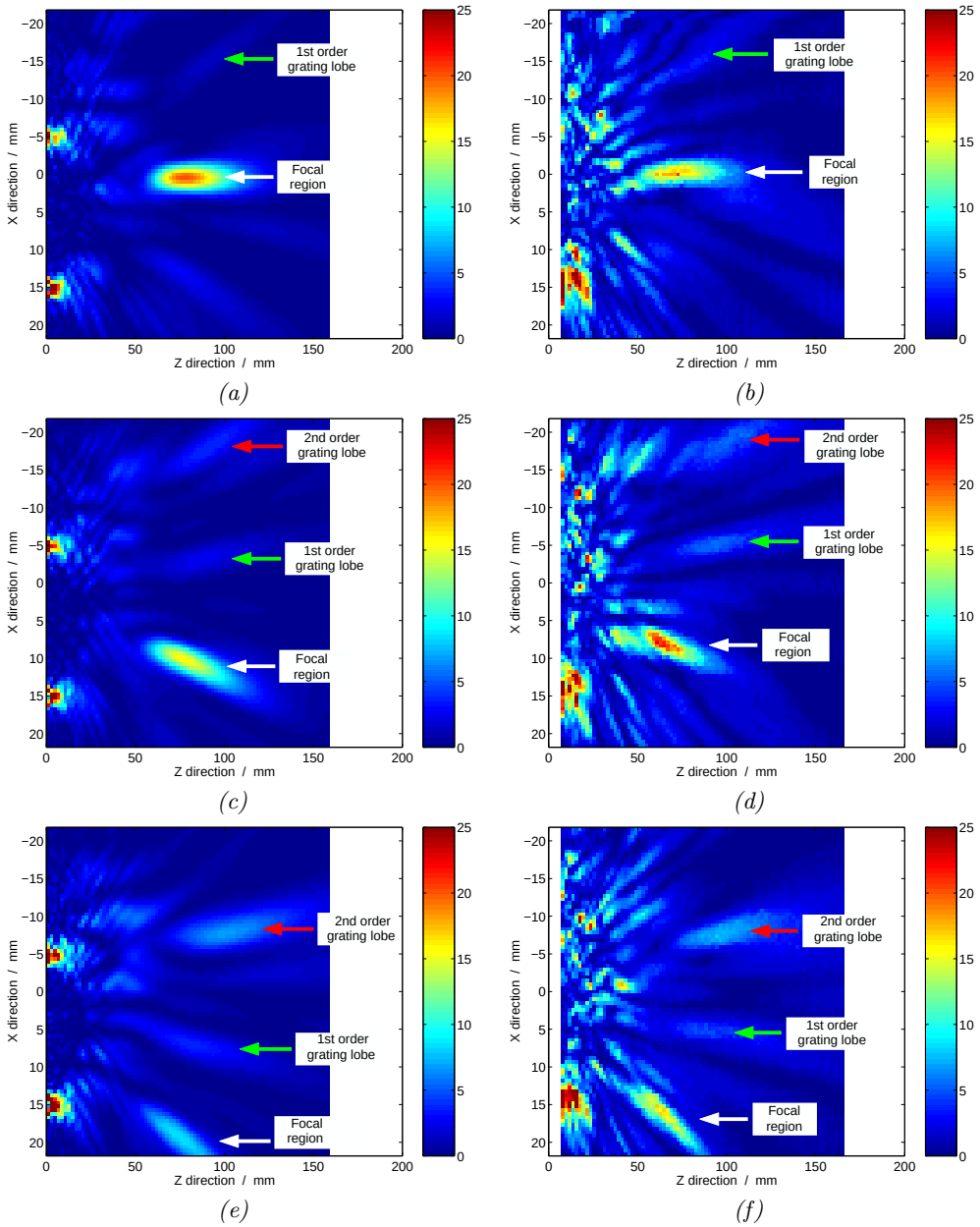

Figure 6.10: 2-D Intensity profiles with the array focussed at a depth of 80mm and steered off-axis by (a,b) 0 mm, (c,d) 10 mm and (e,f) 20 mm. The left-hand plots (a,c,e) show the simulation results and the right-hand plots (b,d,f) show experimental measurements. The array is positioned at the left hand side with the ultrasound propagating left to right. The colours indicate the intensity in $mWcm^{-2}$.

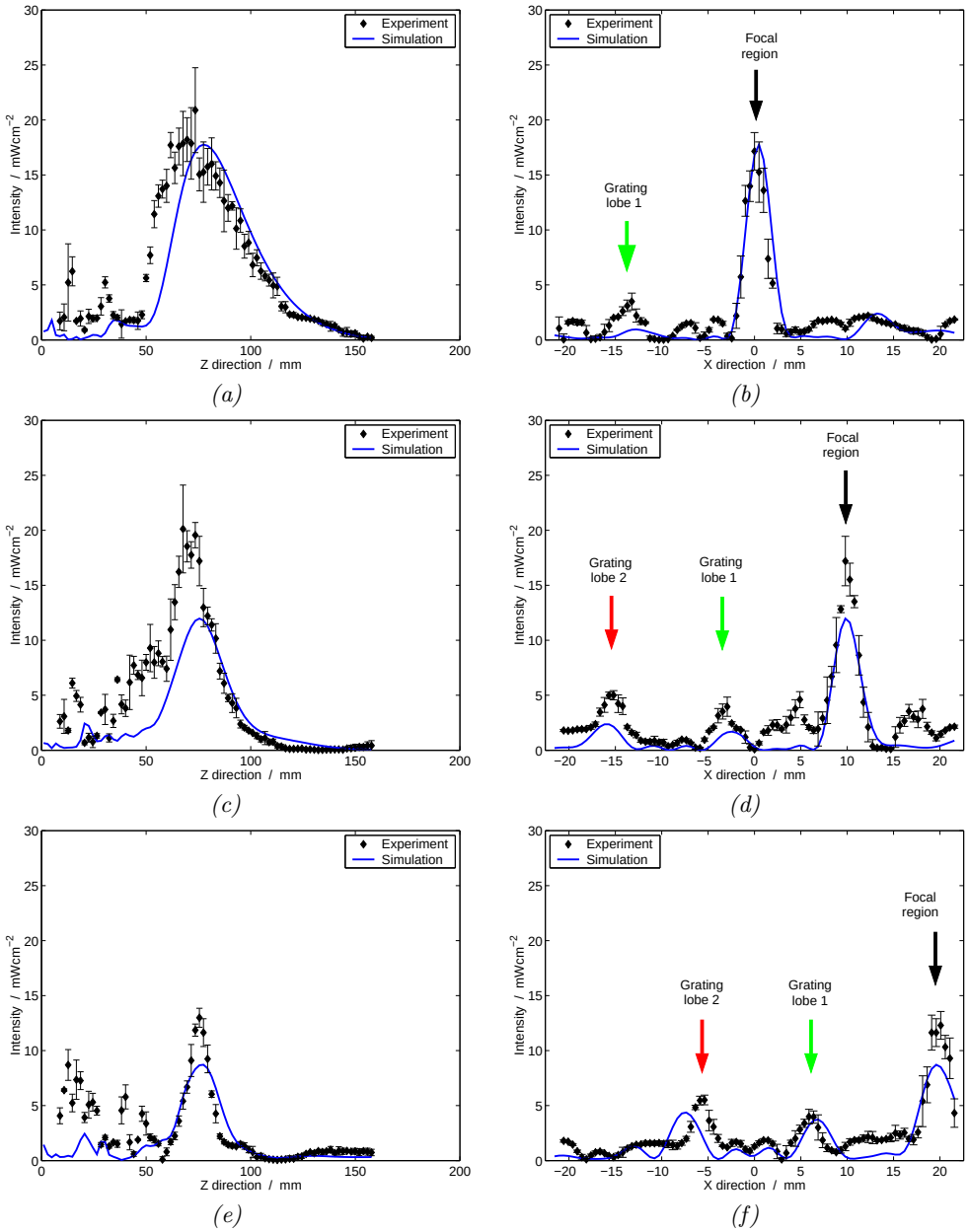

Figure 6.11: Intensity profiles with the array focussed at a depth of 80mm and steered off-axis by (a,b) 0mm, (c,d) 10mm and (e,f) 20mm. The left-hand plots (a,c,e) show the simulated and measured intensities along the central axis of the array and the right-hand plots (b,d,f) show the simulated and measured intensities in the x direction through the focus.

6.5.2 Off-axis focussed fields: Grating lobes

In both the 2-D and 1-D plots the first and second order grating lobes are labelled. Their positions in the experimental profiles show good agreement with the positions in the simulations: In both cases the first order lobe was at an angle of 10 $\pm$ 1° from the focal region, while the second order lobe was at an angle of 18 $\pm$ 1°. (Note that these angles cannot be measured directly from figure 6.10 due to the differing length scales in the x and z directions.)

Although the geometry of the 2-D array is more complex than the 1-D array to which equation 2.13 (section 2.3) applies, that equation may still be used to obtain a simple prediction of the grating lobe angles for the 2-D array. The minimum inter-element pitch for the 2-D array, which was also the most commonly occurring inter-element pitch, was approximately 9 mm (figure 4.1b). For this inter-element pitch, equation 2.13 predicts that the first and second order grating lobes would be found at angles of 9.5° and 19.2° respectively from the principal maximum, which is in good agreement with the angles obtained from both the simulation and experimental profiles for the fifteen element array.

As the focal region was steered away from the central axis, the intensity of the grating lobes increased. It appeared from both the simulation and experimental results that the intensity of the second order grating lobe was greater than that of the first order lobe. However, the simulated intensity profile in the plane parallel to the transducer surface and through the focus is shown in figure 6.12, and it demonstrates that the grating lobes take the form of a band of regional maxima. The particular x, z plane in which the profiles in figure 6.10 were taken contains one of the high intensity maxima within the second order lobe and one of the lower intensity regions within the first order grating lobe. However, the first order lobe does contain several other regional maxima which are more intense than those in the second order lobe.

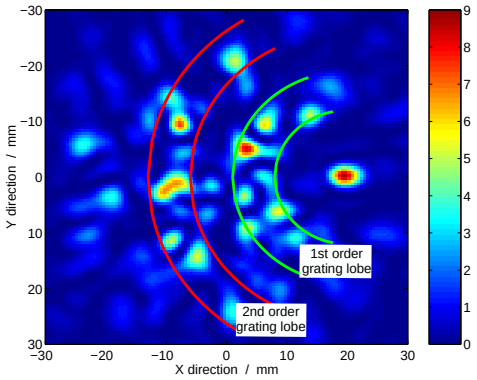

Figure 6.12: 2-D simulated intensity profile for the fifteen element array where the focus is steered 20 mm away from the central axis of the array and to a depth of 80 mm. The profile is in the x, y plane through the focus. The scale on the right indicates the intensity in $mWcm^{-2}$. The 1st and 2nd order grating lobe bands are indicated.

6.5.3 Off-axis focussed fields: Focal intensity

In section 2.3 it was noted that the focal intensity of an array decreases as it is steered away from the central axis of the array (figure 2.1). While it is possible to calculate the expected grating lobes angle from the equations for a 1-D array, calculation of the expected focal intensity for a steered field is more complex. The pressures of the primary peak and the grating lobes are contained within an envelope (which is defined by equation 2.14 for the case of a 1-D linear array), with the result that the focal pressure decreases as it the focal region is moved away from the central axis. As the focus is moved laterally, the amplitude gain of the array must be reduced in order to keep the focus in the same x, y plane. The focal intensity is therefore not defined purely by the diffaction envelope.

Comparison can be made between the simulated and experimentally measured peak focal intensities as the focus is steered away from the central axis for simulation and experiment, as shown in table 6.4. The table shows that the decrease in focal intensity with steering angle was smaller for the experimental results than the simulation results, which indicates the presence of an experimental effect which is not present in the simulations.

Table 6.4: Comparison between the experimentally measured and the simulated peak focal intensity, for fields focussed at distances of 0, 10 and 20 mm away from the central axis of the array. The experimental values represent the median and standard deviation of the measurements at the focal peak.

Distance away from the central axis	**Peak focal intensity relative to the on-axis peak focal intensity**	
mm	Experiment	Simulation
0	1.00	1.00
10	1.07 $\pm$ 0.18	0.78
20	0.82 $\pm$ 0.14	0.35

6.6 Focussed field pressure distributions

6.6.1 Comparison between and experimental and simulated pressure distributions

It was noted in sections 6.4.1 and 6.5 that the focal regions in the experimental profiles are closer to the surface of the fifteen element array than they are in the simulations. Another prominent difference between the simulated and experimental profiles is that numerous local intensity maxima are present between the transducer surface and the focal zone in the experimental profiles, but are absent from the simulated fields. These maxima can be clearly seen both in the experimental profiles of fields focussed at various depths on the central axis of the array (figure 6.7) and in the experimental profiles of fields focussed away from the central axis (figure 6.10).

It is important to note that the positions and intensities of these maxima are likely to be highly sensitive to the exact choice of plane through which the field is measured, and to variation in the physical and material factors which affect the behaviour of each element in the array. Because of this, obtaining good agreement between experimental measurements and simulated field profiles in terms of the positions, geometries and intensities of the maxima is not a realistic expectation.

A more appropriate measure for comparison between simulation and experiment is to consider the distribution of the RMS pressures within the near-field of the

array (where the near-field is defined as the region between the surface of the array and the focal zone). Considering the distribution of pressures allows the near-field as a whole, rather than the features within the near-field, to be characterised.

For the fifteen element array, the pressure distributions were obtained from the simulated and measured 2-D field profiles using the technique outlined in section 5.5.2. The region of interest was defined as the region of the field bounded in the x direction by the edges of the array, and between the array surface and a depth of half the phase-defined focal distance in the z direction. A Rayleigh distribution was fitted to each pressure distribution, again using the technique outlined in section 5.5.2.

The experimental pressure distribution within the region of interest for a field focussed to a depth of 80 mm is shown in figure 6.13a in comparison to the Rayleigh distribution best fit to the experimental data, while figure 6.13b shows the simulated pressure distribution and the corresponding best fit Rayleigh distribution. In both of these plots the pressures are normalised relative to the peak focal pressure. In figure 6.13a the Rayleigh fit is in reasonably good agreement with the overall trend of the experimental pressure distribution, although the experimental data has a bimodal structure which results in some deviation from the fit. This bimodal structure will be considered in section 6.6.2. In figure 6.13b there was good agreement between the simulated pressure distribution and its Rayleigh fit.

While it can be seen qualitatively from figure 6.13 that the simulated pressure distribution contains a higher proportion of low pressure regions than the experimental pressure distribution, the Rayleigh fits enable this difference to be quantified. The values of σ obtained for the Rayleigh fits to experiment and simulation are shown in figure 6.14 for fields focussed to depths of 40, 60, 80, 100 and 120 mm. As described in section 5.5.2, σ defines the position of the peak in the Rayleigh distribution. Over the range of focal depths studied here, σ has a mean value of 0.33 ± 0.03 and 0.19 ± 0.02 times the peak focal pressure for experiment and simulation respectively. The best fit straight line and 95% confidence band for the fit are shown in figure 6.14 for both the experimental and simulation results, clearly showing the

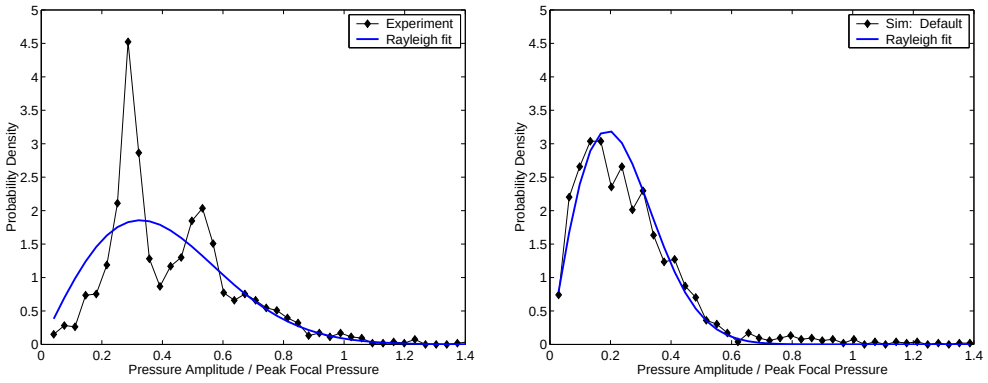

(a) *(b)*

Figure 6.13: (a) Measured and (b) simulated pressure distributions in the region of the field bounded by the outermost edges of the fifteen element array and half the focal distance of 80 mm, in comparison to the best fit Rayleigh distributions. The Rayleigh distribution fits are defined by σ values of 0.33 and 0.19 for experiment and simulation respectively. The pressures are normalised relative to the peak focal pressure.

difference between the two sets of data.

It should be noted that the best fit straight lines through the data in figure 6.14 suggest a possible relationship between σ and the focal depth. However, this trend cannot be said to be statistically significant since a horizontal line fit (representing no relationship between σ and depth) can also be contained within the band.

6.6.2 The bimodal nature of the experimental pressure distributions

Figure 6.13a demonstrated that the experimental pressure distribution for a field focussed at a depth of 80 mm had a bimodal structure that was not predicted by simulation. Figure 6.15 demonstrates that the same bimodal structure was present in the pressure distributions obtained from fields focussed at other depths (from 40 mm to 120 mm). This x-axis of this figure is labelled as the hydrophone output voltage (which is proportional to the RMS pressure) to highlight the fact that the two peaks (labelled A and B) occurred at the same position in each distribution.

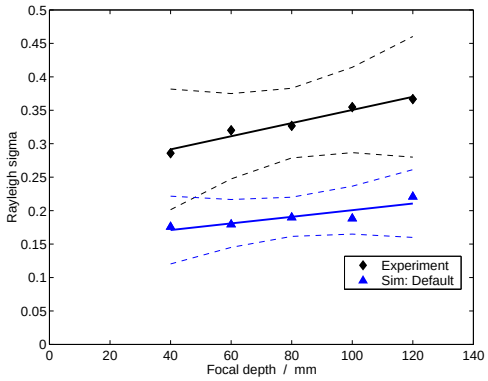

Figure 6.14: The Rayleigh distribution fits to the experimental and simulation data. The data represent the values of σ obtained from the experimental (◆) and simulation (▲) pressure distributions. The best fit straight lines through the data and the corresponding 95% confidence bands and also shown.

The results therefore indicate that the experimental measurements are affected by some factor which is absent from the simulations.

Two potential sources of origin of the bimodal structure can be identified for investigation:

1. The peaks could be a result of array behaviour which is not predicted by simulation, just as the difference in the position of the focus, the presence of local intensity maxima in the near-field, and the difference in the focal intensity of fields steered away from the central axis may be caused by unexpected array behaviour.
2. The two peaks may be an artefact that appears as a result of non-ideal behaviour of the measurement system.

The first of these potential causes of the bimodal distributions is investigated in the sensitivity analysis in chapter 7. As will be described in that chapter, although the other field characteristics could be reproduced by incorporating non-ideal array behaviours into the simulations, the bimodal pressure distributions could not. While the possibility remains that the bimodal distributions are caused by some other array behaviour that has not been considered by the analysis, non-ideal behaviour of the

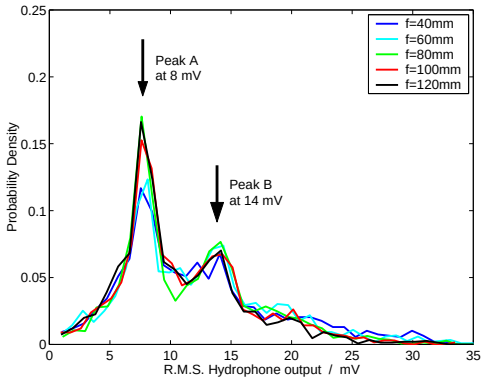

Figure 6.15: Experimentally measured pressure distributions for fields focussed on the central axis of the array to depths of 40, 60, 80, 100 and 120 mm. The distribution of pressures within the region of the field bounded by the outermost edges of the array, and at depths of less than half the focal distance is shown. The hydrophone output is proportional to pressure, with peaks A and B corresponding to RMS pressures of 5300 and 9270 Pa respectively.

experimental measurement system appears to be the prime suspect.

Within the measurement system there are a number of factors which could impact on the shape of the measured pressure distributions. In order for the distribution of measured signals to accurately reflect the distribution of pressures within the field under test the behaviour of several parts of the apparatus must be linear: the movement of the hydrophone positioning system, the response of the hydrophone with pressure, and the response of the oscilloscope to an input signal.

To investigate the nature of the problem, field profiles were plotted to identify whether the pixels associated with the peaks were clustered within a particular region of the field or were randomly spread. Figure 6.16 illustrates the distribution of the pixels in peak A for the case where the array was focussed to a depth of 80 mm. A similarly even spread was seen for peak B. The results demonstrate that the pixels associated with each peak are spread throughout the region of interest without forming any localised clusters. Similar plots of the field at other focal depths were consistent with this result, demonstrating that the peaks are not associated with a cluster of similar hydrophone output voltage measurements within

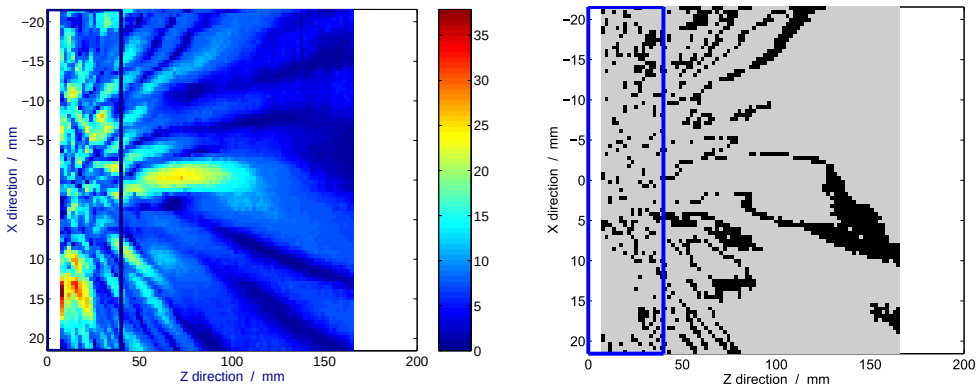

Figure 6.16: Plots showing the measured intensity profile with the array focussed to a depth of 80 mm. A rectangle encloses the region of interest used to obtain the pressure distributions. The scale to the right of plot (a) indicates the RMS hydrophone output in mV, which is proportional to pressure. In plot (b) the pixels belonging to peak A in figure 6.15 are highlighted in black.

a particular region of the field, but are due to a large number of similar voltage measurements spread across the whole region of interest. This suggests that the hydrophone positioning system is not the origin of the problem.

If the two peaks were caused by the hydrophone or oscilloscope then it is to be expected that the peaks would be present at the same hydrophone output in all pressure distribution measurements. Figure 6.15 showed that the two peaks remained fixed at the same hydrophone outputs (and therefore the same pressure amplitudes) when the configuration of the field was varied by changing the depth of the focus from 40 mm to 120 mm. The same was true for the fields focussed away from the central axis of the array, where the two peaks in the pressure distribution remained fixed at the same hydrophone outputs as the focal region was steered away from the central axis. However, these fields are very similar in geometry and intensity and so it is perhaps to be expected that they are also similar in terms of the pressure distributions.

If measurements of the field produced by the fifteen element array were made while driving the array at a higher drive voltage, it would be expected that the pressures in the field would increase linearly with the drive voltage, as was the case

for a single element (section 6.2). Also, the geometry of the field ought to remain unchanged, since that was also the case for a single element. As a result, the peaks in the pressure distribution ought to shift to higher pressures if they are physically real. If however the peaks in the pressure distribution remained at the same hydrophone output value as the drive voltage was increased, then this would confirm that the source of the problem is in the measurement equipment. Unfortunately, making these measurements was not possible within the present work as a modified version of the array drive electronics is required for the higher transducer drive voltages.

Another potential test would be to measure field profiles produced by other arrays and look for peaks in the pressure distribution at the same hydrophone outputs. If the measurement equipment was the source of the problem then peaks ought to occur at the same two hydrophone outputs as for the fifteen element array. These measurements could not be made as part of the present work as no other suitable array was available. While it should also be possible to analyse the field profiles of individual elements for these two peaks, in practice doing so was impractical since the smaller number of measurements involved in single element profiles limited the resolution of the pressure profiles and made it impossible to identify clearly whether the peaks were present or not.

As a result, the exact origin of the bimodal structure of the experimental pressure distributions is not known.

6.7 Summary

The primary aim of the experimental work reported in this chapter was to provide data which could be compared against results obtained by simulation, in order to verify that the simulation model provides physically meaningful results. The results discussed in this chapter have demonstrated that the simulations show good agreement with the experimental results in certain aspects, while in other aspects there are differences between the two.

The aspects in which there was good agreement between the simulation and

experimental results included:

1. The geometry of the field for a single element within the fifteen element array, although there were several elements where the geometry of the experimentally measured field differed from the simulations.
2. The relationship between drive voltage and intensity at a point in the far field of a single element within the fifteen element array, where the intensity is proportional to the square of the drive voltage.
3. The geometry of the focus within focussed fields.
4. The relationship between focal intensity and the number of active elements within the array, where the intensity is proportional to the number of elements within the array.
5. The existence of high intensity regions at the surface of the array directly beneath each element.
6. The position of the grating lobes within a focussed field, in terms of the angle between the grating lobes and the focal region.

The good agreement between experiment and simulation for these aspects provides validation for the work described in chapter 3. The results demonstrate that the geometry of the focal region is predicted well by the simulation tool, giving confidence in the validity of the models describing the focal geometry produced by an idealised array (section 3.4.2) and the effect of practical considerations (in particular, element size) upon these models (section 3.5.1). The good agreement between the experimental and simulation results in the other characteristics of focussed fields (such as the position of the grating lobes) gives confidence in the ability of the simulation software to model arbitrary array geometries, both for fields focussed on and off the central axis of the array.

The secondary aim of the experimental work was to identify any aspects in which there was poor agreement between the experiment and simulated results. These discrepancies point to array behaviour which is not predicted by the sim-

ulations and which requires further investigation to understand and characterise. Aspects in which the experimental results differed from simulation included:

1. The positioning of the focus several millimetres closer to the transducer in the experimental fields in comparison to the simulated fields.
2. The existence of numerous local maxima between the focal region and the transducer surface in the experimental focussed fields, which is illustrated by the larger proportion of higher pressure amplitudes in the experimental pressure distributions in comparison to the simulated distributions.
3. The bimodal nature of the experimental pressure distributions in comparison to the simulated distributions.
4. The intensity of the focal region in the experimental fields decreased less as the focus was steered away from the central axis of the array than predicted by the simulated fields.

The differences between the experimental and simulated fields suggest that there are factors at work in the operation of the real array which are absent in the simulation. However, while these factors affect the field characteristics mentioned above, the impact on the geometry of the focal region for a field focussed on the central axis of the array is sufficiently small that the experimental results still fit the models regarding the focal geometry. Nevertheless, further investigation is required to identify the potential cause of the above differences, and the sensitivity analysis in section 7 describes work which considers this problem.

In addition to these differences between simulation and experiment, the experimental work characterised one factor which is known to be present to some degree within all phased arrays but which is neglected within the simulation models used in this work: that of the inter-element cross-coupling. The results demonstrated that cross-coupling within the array is relatively weak in comparison to the magnitude of the drive signal to each element. However, the experimental results do not provide any insight into the impact this level of cross-coupling may have on the field produced by the array, and this too is investigated in the sensitivity analysis.

Chapter 7

Sensitivity Analysis

7.1 Objectives

In chapter 6, four aspects in which the experimental results differed from the simulation results were highlighted: [i] The difference in the position of the focal region; [ii] The existence of numerous maxima between the transducer surface and the focal zone in the experimental data, but not in the simulated fields; [iii] The bimodal nature of the experimental pressure distributions in the near-field region; [iv] The difference in the focal intensity for fields focussed away from the central axis of the array.

One clear difference between simulation and experiment is that the simulations were performed using a sinusoidal drive signal whereas the measured results were obtained using a square-wave drive signal. The impact of this on the field produced by the array is considered in section 7.2, where it will be shown that the square-wave drive signal cannot account for the discrepancies between the measured and simulated profiles.

An investigation of the impact of other factors on the field produced by the array was therefore required to identify the origin of the difference between the measured and simulated fields. This was done by performing a two stage sensitivity analysis using Ultrasim (sections 7.3 - 7.4). The aim of the first stage was to identify which factors affect the field characteristics of interest. Once identified, the second stage was to investigate the important factors in more detail to obtain an improved fit between the experimental data and the modified simulations, allowing simulations

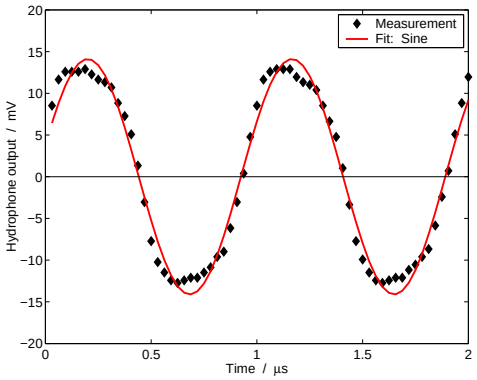

Figure 7.1: The shape of the ultrasound waveform produced by a single 4 mm diameter element, measured at a distance of 8mm directly in front of the element. The least-squares best fit sine wave is plotted for comparison. The coefficient of determination $R^2 > 0.95$ *for the fit.*

to be performed to study the likely impact on arrays composed of a larger number of elements.

7.2 Analysis of the impact of a square-wave drive signal

In section 5.2 it was noted that the drive signal to each element of the fifteen element array took the form of a square-wave. Despite this, the shape of the pressure wave produced by each element was approximately sinusoidal, as illustrated in figure 7.1. While this may suggest that the ultrasound source was vibrating under simple harmonic motion, it is worth describing simulations which investigate the potential impact of square-wave drive conditions on the fifteen element array, before describing the sensitivity analysis where the impact of other factors on the field produced by the array will be investigated.

While Ultrasim cannot directly simulate fields originating from sources where the vibration is not sinusoidal, such simulations are possible using the following method. The Fourier series must first be calculated for the desired waveform, enabling simulations to be performed for each frequency in the Fourier series, such that the pressure contributions from each frequency may be summed to compute

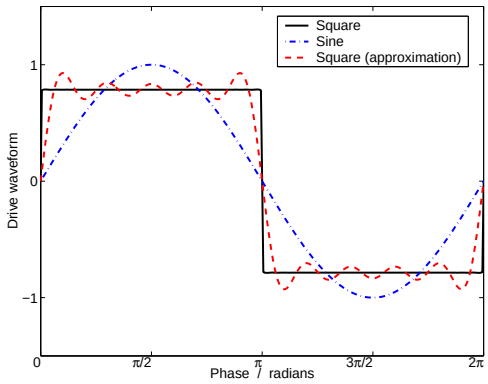

Figure 7.2: An illustration of a square-wave approximation obtained from the first five terms of the square-wave Fourier series.

the resultant pressure field.

The first five terms in the Fourier series for a square-wave are given in equation 7.1, where ω is the fundamental angular frequency. Figure 7.2 illustrates the waveform produced by these five terms, approximating a square-wave. Simulations of the fifteen element array were performed for these five frequencies to study the potential impact of these harmonics on the field produced by the array.

$$f(t) = \sin(\omega t) + \frac{\sin(3\omega t)}{3} + \frac{\sin(5\omega t)}{5} + \frac{\sin(7\omega t)}{7} + \frac{\sin(9\omega t)}{9} + \ldots \tag{7.1}$$

Figure 7.3 illustrates the simulation results for the individual frequencies within the Fourier series, with plots a, b and c showing the pressure profiles corresponding to the first (1 MHz), second (3 MHz) and third (5 MHz) terms in the Fourier series respectively. Three observations can be noted from these plots: [i] The fields produced by the higher frequency terms are very weak in comparison to that produced by the 1 MHz term, which is partly a consequence of the $\frac{1}{3}$ and $\frac{1}{5}$ multipliers in the Fourier series. Since the intensity is proportional to the square of the pressure amplitude (equation 2.15), the contribution to the overall intensity from the higher frequency harmonics will be small; [ii] At the higher frequencies, each element is much more directional than at 1 MHz. This increased directionality means that higher frequency terms in the Fourier series have little impact on

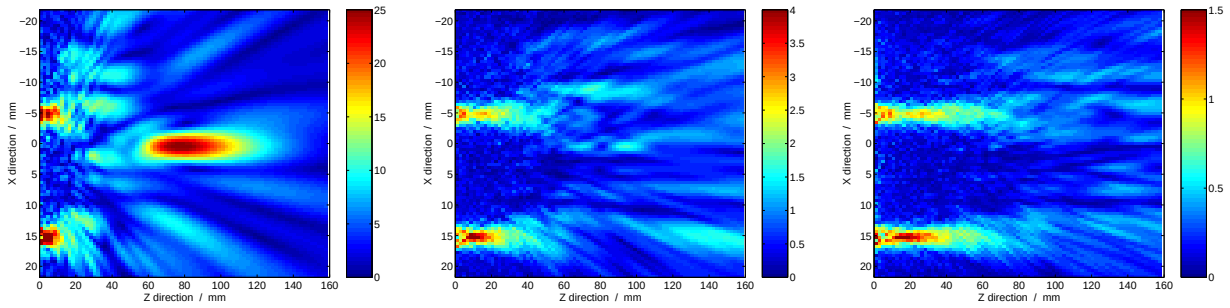

Figure 7.3: Simulation results illustrating the field produced by high frequency harmonics. Plots (a),(b) and (c) illustrate the simulated 2-D pressure profiles for the first ($\sin(\omega t)$), second ($\frac{\sin(3\omega t)}{3}$) and third ($\frac{\sin(5\omega t)}{5}$) terms in the square-wave Fourier series (equation 7.1) respectively. The simulation data has been scaled by fitting the 1 MHz simulated field to the experimental data using the procedure outlined in section 5.5.1, and then by scaling the 3 MHz and 5 MHz simulated fields accordingly. The colours in the plots indicate the RMS pressures in kPa. Note that the pressure scales in plots (b) and (c) are much smaller than in plot (a).

regions of the field not directly in front of the elements; [iii] At the higher frequencies the field does not exhibit a focal region at the focal depth of 80 mm. This is because $\Delta Path_{max} \gg \frac{\lambda}{2}$ for the harmonic frequencies greater than 1 MHz, therefore exceeding the limit on $\Delta Path_{max}$ described in equation 3.7.

To calculate the pressure field that would result from a square-wave drive signal, the (complex) pressure fields corresponding to the first five terms in the Fourier series were summed, and the amplitudes of the resultant pressures were computed.

Figure 7.4 compares the simulation results for the sinusoidal and square-wave drive conditions. Plots (a) and (b) illustrate the simulated 2-D intensity profiles for the sinusoidal and square-wave drive conditions respectively. Visually, the field in figure 7.4b appears very similar to that of figure 7.4a, but has a more textured, 'rippling' appearance. It is clear that the square-wave drive condition has not prompted the appearance of intensity 'hot-spots' in the near-field.

Due to the increased directionality of the field produced at the higher harmonics by each element, it might be expected that the intensity of the high intensity

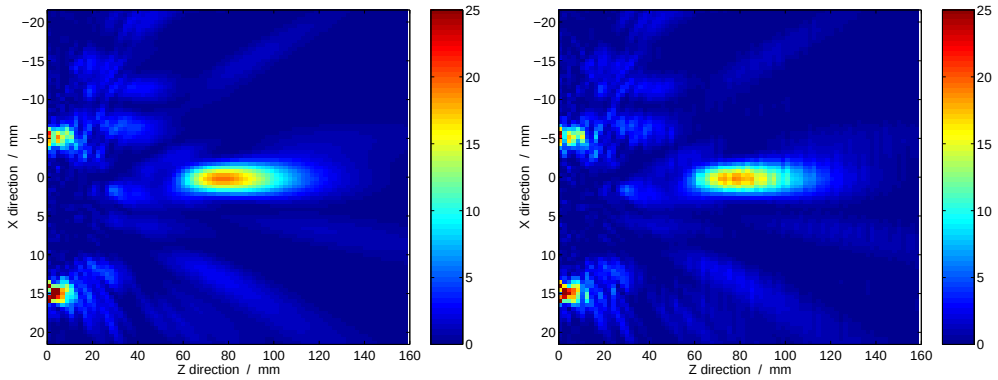

Figure 7.4: Simulation results illustrating the potential impact of square-wave drive conditions. Plots (a) and (b) illustrate the simulated 2-D intensity profiles for the sine and square-wave drive conditions respectively, where the square-wave has been approximated using the sum of the first five terms in the square-wave Fourier series (equation 7.1). The colours indicate the intensities in $mWcm^2$.

regions which are located directly in front of each element in the array would be increased. In fact, the impact in this area was negligible as can be seen from figure 7.4. This is partly a consequence of the low amplitude of the pressure contributions from the higher harmonics, but it is also because the local pressure maximum in the region directly in front of each element moves further from the array as the frequency is increased.

Plot 7.5a compares the simulated 1D intensity profiles along the central axis of the array for sinusoidal and square-wave drive conditions, showing that no change in the position of the focal region has arisen from the addition of the higher frequency harmonics.

Plot 7.5b illustrates the distribution of pressures in the near-field for the sinusoidal and square-wave drive conditions. The Rayleigh distribution fits to these pressure distributions yield σ values of 0.189 and 0.185 respectively, confirming that there was no change in the distribution of pressures in the near-field region caused by the addition of the higher frequency harmonics. This is consistent with the observation made from plot 7.3b, since the directional nature of the high frequency contributions to the pressure field will have little impact on field regions not directly

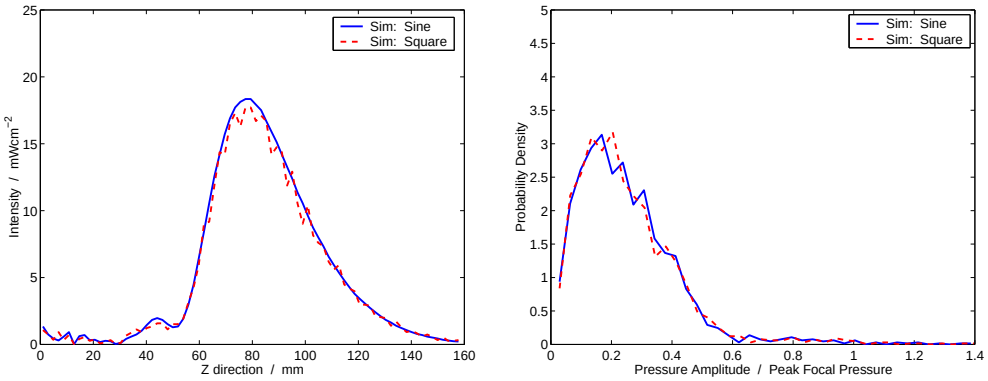

(a) *(b)*

Figure 7.5: Simulation results illustrating the potential impact of square-wave drive conditions. Plot (a) compares the simulated 1D intensity profiles along the central axis of the array for sine and square-wave drive conditions; Plot (b) illustrates the distribution of pressures in the near-field for sine and square-wave drive conditions. The Rayleigh distribution fits to these pressure distributions yielded σ values of 0.189 and 0.185 respectively.

in front of an element. The addition of higher frequency harmonics does not impact on the distribution of pressures in the near-field, or recreate the bimodal pressure distribution observed experimentally (figure 6.15).

In summary, simulations indicate that higher frequency harmonics (which may or may not be present in the real array) would have little impact on the position of the focal region produced by the fifteen element array, or on the distribution of pressures in the near-field. This result confirms that, even if higher frequency harmonics were present, the Rayleigh distribution would remain a suitable function to describe the distribution of pressures in the simulated ultrasound fields.

7.3 Sensitivity analysis stage one: Identification of the significant factors

7.3.1 Design of experiment

The first stage of the analysis was to identify which factors have the potential to impact on the behaviour of the fifteen element array and affect the field characteristics

of interest. A review of the assumptions upon which the original simulations were based (section 3.2.2) together with the processes used in the manufacture of the array (section 4.3) and the limitations of the drive electronics (section 5.2) allowed the following five factors to be identified as potentially impacting on the behaviour of the real array: variation in the amplitude of the output from each element; the effect of including a secondary mode of vibration in each element; quantisation of the phase differences between elements; errors in the spatial positioning of each element; and inter-element cross-coupling. Each of these will now be considered in turn:

1. Element drive amplitude variation:

   Variation in the drive amplitude of each element was included in the sensitivity analysis since the measurements made on individual elements in the array showed a large range in output between elements. In the measurements shown in figure 6.1d, the intensities produced by each element varied by up to a factor of four at the intended focal depth of 60 to 100mm, corresponding to a pressure variation of up to a factor of two. Two situations were included in the sensitivity analysis: the default case, where each element was driven with an equal amplitude; and the modified case where each element in the array was driven at a different amplitude, chosen to match the experimental measurements on corresponding elements in the real array.

2. Mode of vibration:

   The simulations considered so far have assumed that each PZT element behaves as a piston, with all points on the element surface vibrating in phase. However, non piston-like vibration of piezoceramic elements has been identified previously [Koyuncu, 1980]. It has been shown that these non piston-like vibrational modes can affect the geometry of the field produced by a single disc radiator in a number of ways depending on the particular mode involved [Hutchins et al., 1986], but the impact on the field produced by phased arrays is not well understood. In addition, Huang et al. [2004] demonstrated that a

large number of possible modes exist for a circular element. The work of Guo and Cawley [1991] used finite element methods to investigate the transient motion of the surface of circular elements under the application of a drive voltage pulse, and noted that while the motion of elements with a diameter to thickness ratio which is either large ($>\sim$20:1) or very small was approximately piston-like, elements with intermediate diameter to thickness ratios were likely to exhibit non piston-like behaviour. It is therefore likely that the elements within the present array, which also have an intermediate diameter to thickness ratio (2:1), may exhibit non piston-like vibration. However, non piston-like behaviour is complex and the vibrational modes are critically dependent on the element geometry, method of mounting and drive conditions. To fully characterise the modes a finite element analysis including all these factors would be required. Indeed, it is likely that the elements within the array will not all vibrate with the same mode given the slight differences in mounting that will exist for each element, and the variation seen in the shape of the 2-D experimental intensity profiles for each of the individual elements (section 6.2.1) is evidence towards this. However, simulations which model the effect of non piston-like element vibration will be useful in identifying the likely effects of this on the field, even if a simplifying assumption is made that the same mode of vibration is present in each element.

The non piston-like mode considered here is axisymmetric about the central axis of the element. An axisymmetric mode would be expected where the following conditions are satisfied: that the PZT and surrounding materials are each homogeneous; that the bond between the PZT and the surrounding materials is uniform around the entire edge of the element; and that the drive force is the same (in both phase and magnitude) across all points on the element surface. In practice however, for any element within a real array all three of these conditions will never be met perfectly, and even if they were, crosstalk from other elements within the array (however weak) would disturb the symmetry of the system. Further, the modes suggested by Huang et al.

[2004] are not axisymmetric. However, studying an axisymmetric case will be sufficient to demonstrate the likely effect that non piston-like motion of the elements would have on the field produced by an array, without detailed study of more complex non-axisymmetric modes.

There are many possible axisymmetric modes for a circular vibrating element which could be considered, each of which are defined by both the amplitude and relative phase of vibration across the surface of the element. Some modes may contain nodes, positions on the surface which undergo no net motion, at which the amplitude of vibration will be zero. A simple vibrational mode was considered here, where a uniform amplitude of vibration was applied across the entire element surface such that there were no nodes. As such, only the variation in phase across the surface of an element was required to define the mode.

The chosen mode corresponded to the addition of a surface Rayleigh wave originating at the element centre and propagating radially, forming concentric surface ripples moving away from the element centre. For this mode to be physically possible requires the assumption that the wave is not reflected at the element boundary, but continues into the material surrounding the element. While this proposed mode may not correspond to the actual mode of vibration of the elements within the fifteen element array, the simulations will be sufficient to investigate the potential impact of non piston-like vibration of the elements on the field produced by the array.

Figure 7.6 shows the particular mode that was considered, where a sinusoidal variation in the phase was applied across the surface of each element within the fifteen element array with the centre leading the edge by 0.5λ. Varying the magnitude of the phase variation in the simulation allowed the relative strength of this secondary mode of vibration to be varied, and hence the effect of this on the ultrasound field to be studied. However, for the sensitivity analysis only two modes of vibration were studied: Ideal piston-like behaviour (the default case), and the case illustrated in figure 7.6, where the centre of

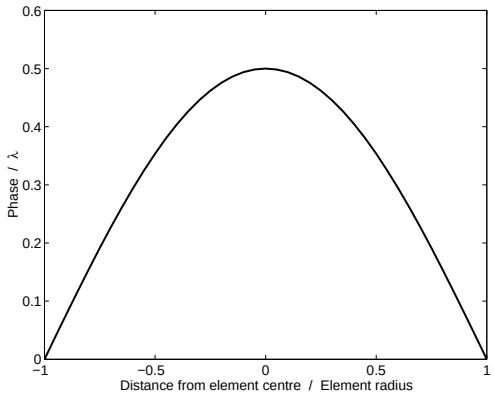

Figure 7.6: Sinusoidal phase variation across the face of an element with the centre of the element leading the edge by 0.5 λ, allowing a secondary mode of vibration to be included in the simulations.

each element led the edge sinusoidally by 0.5λ.

3. Phase quantisation:

   In our experimental set-up (described in section 5.2), the phase of the drive signal was quantised into 8-bits. The simulation software was modified to allow the phase applied to each element in an array to be quantised, with the number of bits being defined by the user. Two situations were considered for the sensitivity analysis: no phase quantisation (the default case); and 6-bit phase quantisation. A coarser phase quantisation was chosen than the 8-bits used in the experimental set-up to amplify the effect of the quantisation in the simulations, as well as to allow for errors in the timing of the drive electronics which would give rise to a phase error greater than that due to 8-bit quantisation alone.

4. Element positioning:

   Element positioning was included in the sensitivity analysis to investigate the impact of construction tolerances in the field produced by the array. A random spatial positioning error for each element in the array was generated based on a normal distribution with a defined standard deviation, σ. Two situations were included in the sensitivity analysis: $\sigma = 0.0$ mm (the default case) and $\sigma = 0.5$

mm, since this was considered to be the 'worst-case' machining tolerance for the positioning of the holes holding the PZT elements in the perspex frame.

5. Inter-element cross-coupling:

   Measurements in section 6.3 showed that the crosstalk within the fifteen element array was primarily due to electrical coupling between elements, while acoustic coupling was negligible. To investigate the impact of this electrical coupling on the field produced by the array, the sensitivity analysis allowed each element's drive signal to be modified by adding a component relating to the crosstalk signals picked up from the other elements in the array.

   The waveform of the crosstalk signal due to electrical coupling was complex, containing frequencies higher than the 1 MHz drive signal (as was shown by the sample waveform in figure 6.3a). Since the total effective drive voltage of a single element within the array can be calculated by taking the sum of its own drive signal (which for the purposes of simulation is assumed to be sinusoidal) and the contributions due to crosstalk from each of the other elements in the array (which for electrical crosstalk are not sinusoidal), the total effective drive voltage will be in the form of a sine wave with high frequency components added to it.

   However, the simulation software required that the vibration of each point source was sinusoidal, and it was necessary to consider a much simpler situation to allow crosstalk to be considered within the sensitivity analysis. Within the simulations, a simplifying assumption was therefore made that the waveform due to electrical crosstalk was sinusoidal, with the result that the drive signal to an individual element could be modified by the addition of crosstalk waveforms to produce an effective drive signal which was also sinusoidal. Equation 7.2 describes how the original sinusoidal drive signal on an element $\overrightarrow{V_{drive}}$ is modified by a sinusoidal crosstalk signal from each of the other 14 elements in the array to give the effective drive signal $\overrightarrow{V_{effective}}$. The crosstalk contribution from element n is given by the product of b_n, a number between 0 and

1 representing the strength of the crosstalk signal from that element, and $\overrightarrow{V_n}$, the drive signal applied to element n. Equation 7.2 considers each voltage as a vector, allowing the phase of each to be included in the consideration.

$$\overrightarrow{V_{effective}} = \overrightarrow{V_{drive}} + \sum_{n=1}^{14} b_n \overrightarrow{V_n} \tag{7.2}$$

Since the crosstalk in the fifteen element array was due to electrical coupling between elements, the phase of the crosstalk signal $b_n\overrightarrow{V_n}$ was assumed to be the same as the phase of $\overrightarrow{V_n}$. In contrast, had the crosstalk been due to acoustic coupling, a phase delay would have been required to take account of the propagation time of the acoustic signal between the two coupled elements.

As regards the strength of the cross-coupling b_n between element pairs, the experimental measurements on the fifteen element array discussed in section 6.3.1 showed that when a 40 V drive signal was applied there was some variation in the strength of the cross-coupling depending on the particular choice of element pair. However, the general trend was that the strength of the cross-coupling was almost independent of the inter-element pitch (figure 6.3b). For the sensitivity analysis simulations, the random variation in b_n was neglected for simplicity, and b_n was assumed to be constant and independent of the inter-element pitch.

The sensitivity analysis considered two situations: The default case where there was no crosstalk ($b_n = 0\%$) and the case where the coupling between elements was 5% of the drive signal ($b_n = 5\%$). The value of 5% used within the sensitivity analysis was an order of magnitude larger than strength of the crosstalk in the experimental measurements (in section 6.3.1) in order to allow the effects of the crosstalk on the field produced by the array to be easily identified.

In addition to these five factors, the impact of non-linear propagation is another potential source of discrepancies between experimental and simulation results. In section 2.5 the example was given of a spherically focussed transducer of similar

dimensions to the fifteen element array with a focal intensity of 1 Wcm^{-2}, and in that case non-linear propagation resulted in distortion of the waveform at the focus. However, the intensities involved in the present work are much lower than this: In comparison, the peak focal intensity produced by the fifteen element array at a depth of 60 mm was 23 $mWcm^{-2}$ (section 6.4.1). Non-linear wave propagation was therefore not included as a factor in the sensitivity analysis due to the low intensities involved.

While one of the aims of the sensitivity analysis was to investigate the impact of each of the five factors individually, the ability to identify any significant interactions between them was also desirable, since the observed field characteristics may not be caused by a single factor but by an interaction between multiple factors. A full-factorial experimental design was therefore a suitable approach to use, as it allows effects arising from any combination of the five factors to be identified. For each of the five factors, the full-factorial design considered two situations: one where that particular factor was included, and one where it was not. As such, the sensitivity analysis produced 2^5 (32) distinct simulation results.

The analysis of the simulation results was performed in two parts. First, the impact of each of the five factors acting independently was investigated, and this will be described in section 7.3.2. Following this, all combinations of the five factors were studied to check for any interactions between factors, and this will be described in section 7.3.3.

The stimulus for the sensitivity analysis was to identify the cause of the four discrepancies between the experimental and simulation results described at the beginning of this section. However, to minimise the number of simulations, the investigation was initially limited to fields focussed on the central axis of the array. Analysis of these results therefore concentrated on the position of the focal region, and on the distribution of pressures in the near-field region. Once the relevant causative factors had been identified from this analysis, the second stage of the sensitivity analysis (in section 7.4) looked at these causative factors in greater detail, and this included an investigation of fields focussed away from the central axis of

the array.

7.3.2 Stage one results: The independent impact of each factor

Pressure distribution in the near-field

Figure 7.7 illustrates a selection of the 32 pressure distributions obtained from the sensitivity analysis in comparison to the experimental result, to illustrate the effect of each of the factors investigated upon the pressure distributions in the near-field. The plots indicate that variation in the amplitude of the output from each element (figure 7.7a), quantisation of the phase differences between elements (figure 7.7c), errors in the spatial positioning of each element (figure 7.7d) and inter-element cross-coupling (figure 7.7e) have little effect on the pressure distribution in the region of the field considered here, since there is no clear difference between the distributions where the factor was not applied (solid line) and those where the factor was applied (dashed line). That is, these factors cannot produce the large change in shape of the simulated pressure distribution required to match the experimental result, and therefore are unlikely to be the cause of the numerous maxima and minima seen in the near-field of the experimental profiles. However, the inclusion of variation in the phase of vibration across the face of each element did produce the large scale change in shape of the pressure distribution required to match the experimental profile, as evidenced by figure 7.7b where there is a clear difference between the distribution where the factor was not applied (solid line) and that where the factor was applied (dashed line).

While the graphs in figure 7.7 show qualitatively that, of the five factors considered, the variation in the phase of vibration across the face of each element was the primary factor responsible for the change in the shape of the pressure distribution required to match the experimental distribution, an analysis that quantifies the effect of each factor is desirable. Previous workers have not investigated the pressure distributions in the near-field of a phased array quantitatively, and therefore an appropriate method of analysis had to be developed within this project.

To do this, Rayleigh distributions were fitted to each of the 32 pressure

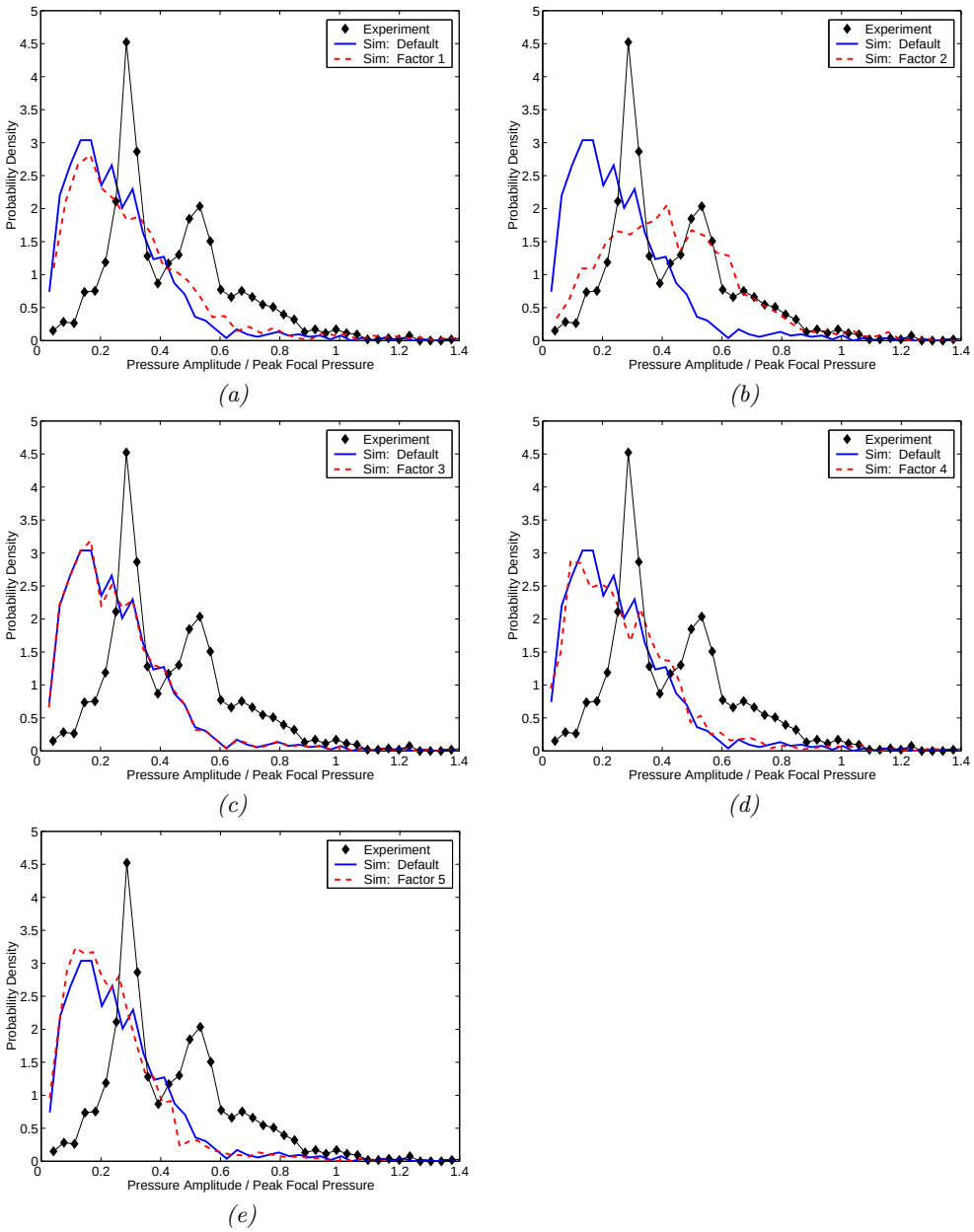

Figure 7.7: Pressure distributions in the region of the field bounded by the outermost edges of the array, and at depths of less than half the focal distance of 80mm. Each plot shows the experimental result, the default simulation result, and the simulation result which included the following factor: (a) Variation in the drive amplitude between each element; (b) Variation in the phase of vibration across the face of each element; (c) Phase quantisation; (d) Element position variation; (e) Inter-element crosstalk.

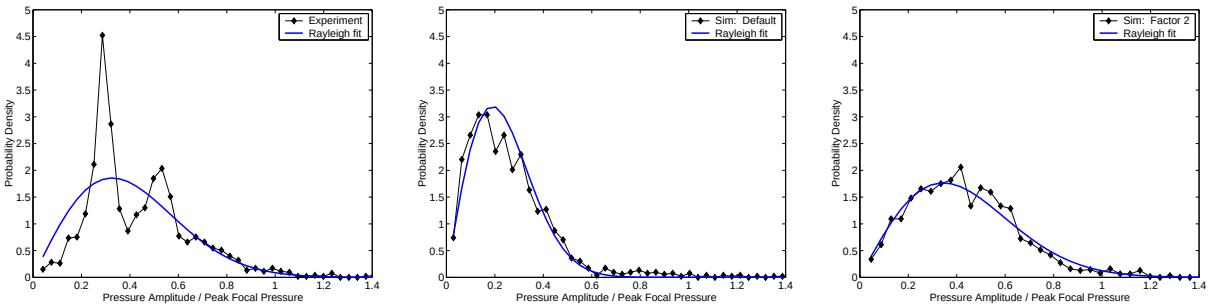

(a) *(b)* *(c)*

Figure 7.8: Graphs comparing the Rayleigh distribution fits against the pressure distributions in the region of the field bounded by the outermost edges of the array, and at depths of less than half the focal distance of 80mm. (a) The experimental result. (b) The default simulation result. (c) The simulation result where the only factor included in the simulation was the variation in the phase of vibration across the face of each element.

distributions obtained from the sensitivity analysis. The rational for the use of the Rayleigh distribution in this situation and a description of the technique used to obtain the fits to the simulated pressure fields are discussed in section 5.5.2. A Rayleigh distribution is defined by equation 7.3 where $f(r)$ is the probability density of the variable r and σ defines the mode (i.e. peak) of the function. As such the Rayleigh distribution fits corresponding to each of the 32 simulated fields could be characterised by the single parameter σ, thereby providing a means for quantitative comparison of the 32 distributions.

$$f(r) = \frac{r}{\sigma^2} e^{\frac{-r^2}{2\sigma^2}} \tag{7.3}$$

For a focal depth of 80 mm, figure 7.8 illustrates the pressure distributions and the corresponding Rayleigh distributions computed by the fitting algorithm for three examples: The experimental data; the default simulation data; and simulation data where the only factor included in the simulation was the variation in the phase of vibration across the face of each element. For these three examples, the Rayleigh distributions are defined by σ values of 0.33, 0.19 and 0.34 respectively. The figure demonstrates that the Rayleigh distribution fits were in good agreement with the

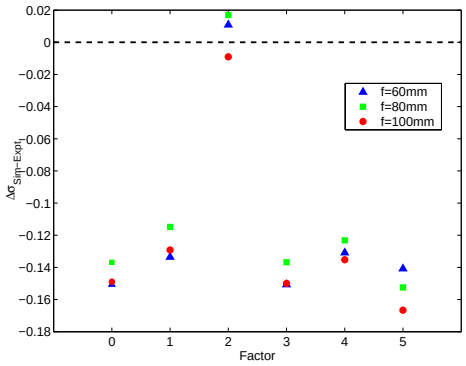

Figure 7.9: Plot showing the effect of each of the factors in the sensitivity analysis. The points show the difference between the Rayleigh distribution σ for experimental result and for the sensitivity analysis simulations, where each factor is included independent of any other factors. The labelled factors are: 0. Default simulation with piston-like motion of each element; 1. Variation in the drive amplitude between each element; 2. Variation in the phase of vibration across the face of each element; 3. Phase quantisation; 4. Element position variation; 5. Inter-element crosstalk.

simulation data, confirming that an analysis based on a comparison of the Rayleigh fits is an appropriate method to use to evaluate the simulated pressure distributions.

The effect of the independent inclusion of each factor on σ is plotted in figure 7.9. In this plot, the y-axis represents the difference between σ_{Expt}, the value obtained from the simulation results and σ_{Expt}, the value obtained experimentally. The horizontal black line at $\Delta\sigma_{Sim-Expt} = 0$ indicates the point of best agreement between the simulation and the experimental pressure distributions, at which σ_{Sim} and σ_{Expt} are equal. Results are shown for six simulation configurations: The default simulation is shown (labelled '0'), as are simulations with each of the five factors (labelled '1' to '5') included in the absence of all other factors.

Figure 7.9 demonstrates that the variation of the phase of vibration across the face of each element (labelled as factor '2') was the only factor which caused a change in σ that was sufficiently large to approach the experimental result. The inclusion of each of the other factors produced little change in σ from the default simulation.

Position of the focus

While the sensitivity analysis showed that the addition of a variation in the phase of vibration across the face of each element in the array was the most significant factor in producing the observed maxima in the near field, the other effect of interest was the difference between the simulation and experimental positions of the focus.

The graphs in figure 7.10 show qualitatively that, of the factors considered, the variation in phase of vibration across the face of each element was also the primary factor responsible for the shift in the position of the focal region. Again, an analysis that quantifies the effect of each factor upon the position of the focal region is desirable.

The analysis performed on the Rayleigh pressure distributions was repeated here to look at effect on the focal position f of the addition of each factor, and the results are plotted in figure 7.11. In this figure, the y-axis represents the difference between the depth of the position of peak intensity obtained experimentally (f_{Expt}) and the depth obtained from the simulation results (f_{Sim}). Results are shown for six simulation configurations: The default simulation is shown (labelled '0'), and simulations (labelled '1' to '5') are shown where each factor of the five factors has been included in the absence of all other factors.

The spread of the results for each focal depth is greater in figure 7.11 than it was for the Rayleigh distribution σ (figure 7.9) because the step size of the data in the z-direction was large relative to the difference between the experimental and simulated focal position. For focal depths of 60, 80, and 100 mm the step size of the data in the z-direction was 1.47, 1.96 and 2.45 mm respectively, and therefore the values of $\Delta f_{Sim-Expt}$ plotted in figure 7.11 are quantised in steps of the same size. As such, a shift of only 3 to 5 pixels in the simulation data was required to produce good agreement with the experimental data. In contrast, the values of σ obtained for each pressure distribution were not quantised.

Despite the relatively large spread in the results caused by the quantisation of the data, it is clear from figure 7.11 that the effect of including a variation of phase of vibration across the face of each element was the only factor which caused

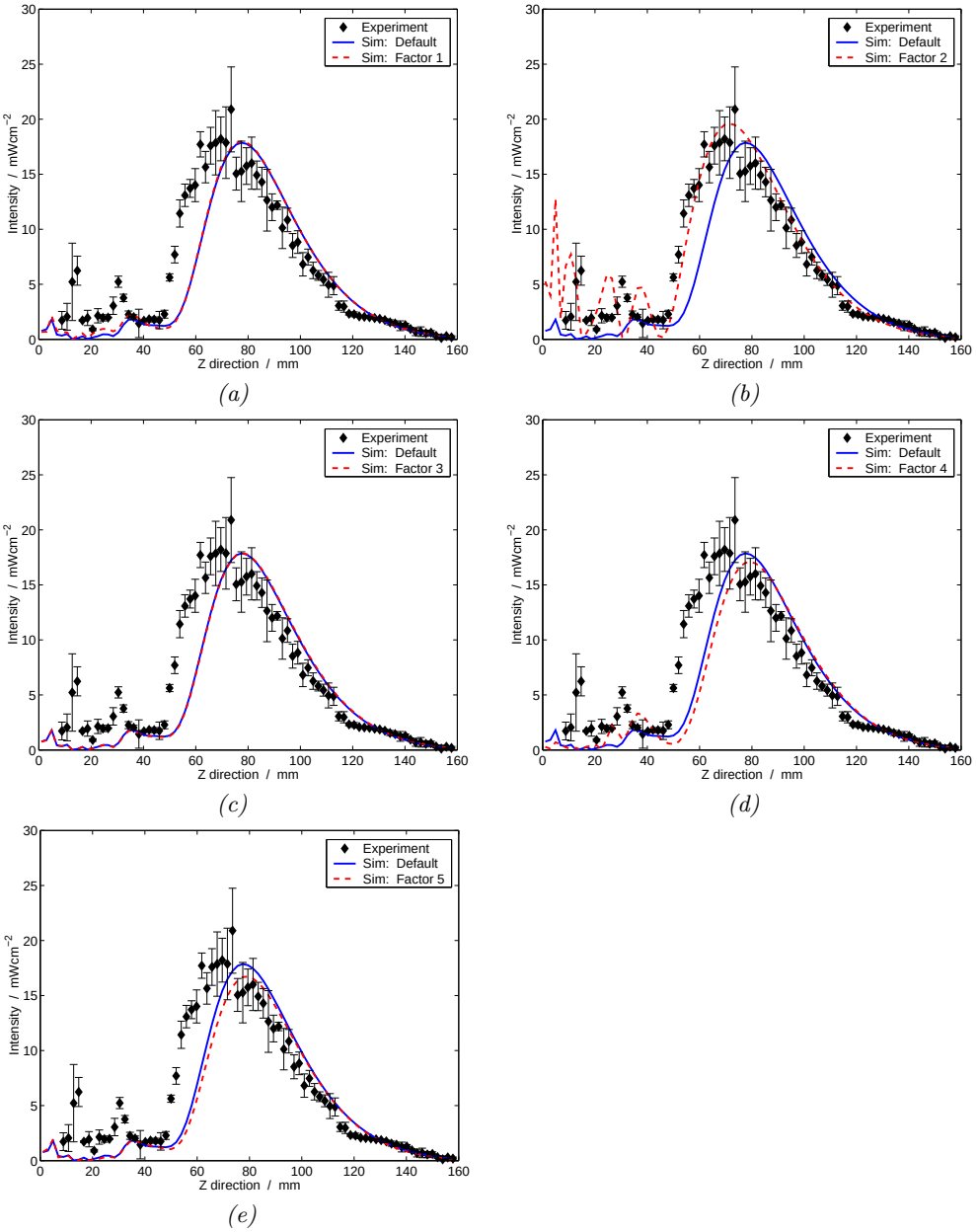

Figure 7.10: Intensity profiles along the central axis of the array for a focal distance $f = 80$ mm. Each plot shows the experimental result, the default simulated profile, and the simulation result which included the following factor: (a) Variation in the drive amplitude between each element; (b) Variation in the phase of vibration across the face of each element; (c) Phase quantisation; (d) Element position variation; (e) Inter-element crosstalk.

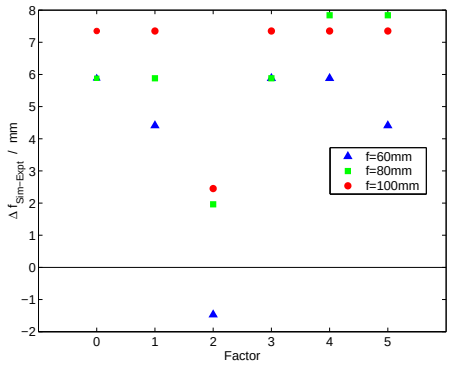

Figure 7.11: Plot showing the effect of each of the factors in the sensitivity analysis. The points show the difference between the focal position f in the experimental result and in the sensitivity analysis simulations, where each factor is included independent of any other factors. The labelled factors are: 0. Default simulation with piston-like motion of each element; 1. Variation in the drive amplitude between each element; 2. Variation in the phase of vibration across the face of each element; 3. Phase quantisation; 4. Element position variation; 5. Inter-element crosstalk.

a change in the position of the focal region that was sufficiently large to approach the experimental result.

Discussion

The difference in the position of the focal region in the experimental and simulation results initially appeared the more straightforward of the two to analyse, since it would be difficult for a simulation to reproduce the exact positions of each of the maxima within the complex structure of the near-field seen in the experimental results. However, figures 7.9 and 7.11 indicate that the use of the Rayleigh distribution to aid the analysis of the structure of the near-field actually provides a more sensitive measure than the analysis of the focal position, since it is not limited by the spatial quantisation of the positional data.

Figures 7.9 and 7.11 point to a single factor (the phase variation across the face of each element, equivalent to the addition of a secondary mode of vibration) as being responsible for both the pronounced maxima at depths of less than half the focal distance and of the positioning of the focal zone closer to the transducer than

expected.

None of the factors investigated in this analysis reproduced the bimodal nature of the pressure distribution seen in the experimental measurements, adding weight to the conjecture discussed in section 6.6.2 that these peaks could be a result of non-ideal behaviour of the measurement system rather than being intrinsic to the field.

It was perhaps surprising that the large variation in the drive amplitude of each element (which modelled the differing output of the elements shown in the experimental results of figure 6.1d) was not an important factor, as can be seen from the fact that factor #1 has no effect on either the Rayleigh distribution σ (figure 7.9) or the position of the focal region (figure 7.11).

7.3.3 Stage one results: Interactions between combinations of factors

The question of whether there are any significant interactions between factors was also investigated using the results of the simulation analysis. An interaction between multiple factors occurs if the combination of factors produces an effect which is not the same as the cumulative effect of each factor on its own. The order of the interaction describes the number of factors involved, where first order involves two factors, second order involves three, etc.

Pressure distribution in the near-field

When testing for interactions between factors, the null hypothesis is that there are no interactions. When considering the pressure distributions in the near-field, a value for σ_{null} can be calculated by adding the σ values for each individual factor alone. These values of σ can be obtained from figure 7.9. As an example, equation 7.4 defines σ_{null} for the combination of factors #1 and #2.

$$\sigma_{null} = \sigma_1 + \sigma_2 \tag{7.4}$$

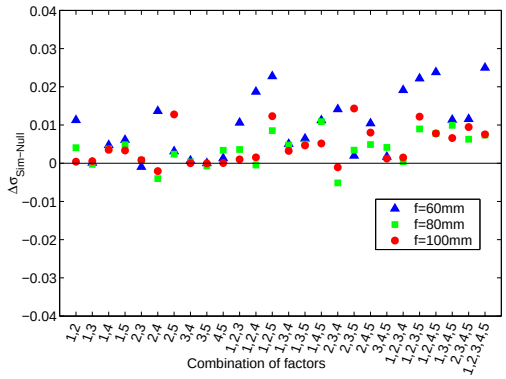

Figure 7.12: Plot of the difference between the values of the Rayleigh pressure distribution σ obtained from simulation (σ_{sim}) and calculated from the null hypothesis (σ_{null}) for each combination of factors in the sensitivity analysis. A non-zero difference would imply the presence of an interaction between two factors. The labelled factors are: 1. Variation in the drive amplitude between each element; 2. Variation in the phase across the face of each element; 3. Phase quantisation; 4. Element position variation; 5. Inter-element crosstalk.

If an interaction exists between factors #1 and #2, then the value of σ obtained from simulation (which shall be denoted σ_{sim}) will be given by equation 7.5.

$$\sigma_{sim} = \sigma_1 + \sigma_2 + \sigma_{12} \tag{7.5}$$

The simulations can therefore be used to test whether any interactions between factors are present by looking at $\sigma_{sim} - \sigma_{null}$, since this will equal zero if no interactions are present.

The sensitivity analysis simulation results were analysed using this technique, and the results are plotted in figure 7.12 for all possible combination of factors. The results indicate that while $\sigma_{sim} - \sigma_{null}$ is generally not zero, it is very small (never more than 4%) in comparison to the difference between σ_{sim} and σ_{expt}. That is to say, the results indicate that the effect of interactions between factors on the Rayleigh pressure distributions are almost negligible.

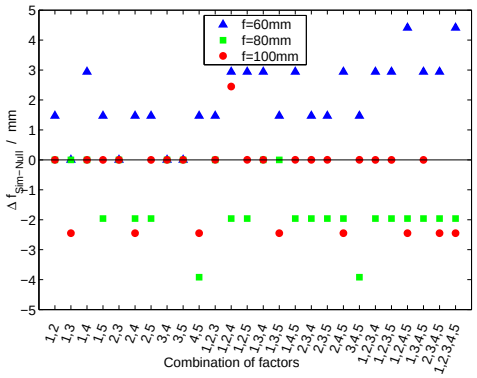

Figure 7.13: Plot of the difference between the values of the focal position f obtained from simulation (f_{sim}) and calculated from the null hypothesis (f_{null}) for each combination of factors in the sensitivity analysis. A non-zero difference would imply the presence of an interaction between two factors. The labelled factors are: 1. Variation in the drive amplitude between each element; 2. Variation in the phase across the face of each element; 3. Phase quantisation; 4. Element position variation; 5. Inter-element crosstalk.

Position of the focus

The same analysis was performed to look at whether the position of the focal region was affected by first-order interactions between any combination of factors. Figure 7.13 illustrates the difference between the simulated focal position (f_{sim}) and the null hypothesis value (f_{null}) for each combination of factors. The results indicate that the position of the focal region was not affected by interactions between any combination of factors, since $f_{sim} - f_{null}$ is consistent with zero given the spread of the results for the different focal depths.

7.4 Sensitivity analysis stage two: Detailed consideration of the significant factors

The first stage of the sensitivity analysis in section 7.3 indicated that, of the five factors studied, the inclusion of a phase variation across the face of each element was the only factor that had any real impact on the two field characteristics of interest (namely, the pressure distribution in the near-field of the array and the

position of the focal zone). With this factor now identified as the one having most influence on the array, another stage of the sensitivity analysis was required to provide information on the nature of the relationship between the phase variation and these two field characteristics. This investigation is discussed in section 7.4.1.

In addition, while the analysis in section 7.3 demonstrated that the impact of inter-element cross-coupling was negligible for a fifteen element array, further analysis is necessary to investigate its impact in an array composed of a greater number of elements spaced more closely together where acoustic coupling will come into play. This is considered in section 7.4.2.

Since the results from stage one of the sensitivity analysis demonstrated that there were no strong interactions between any combination of factors (figures 7.12 and 7.13), the simulations within this section which investigate two of these factors more closely have been performed looking at each of the two independently.

7.4.1 Non piston-like behaviour of the PZT

Simulations of the fifteen element array were performed to investigate in more detail the effect of the non piston-like vibration of the elements within the array introduced in section 7.3. While the real vibrational mode of the elements is likely to be much more complex than that modelled by the simple sinusoidal phase variation in the present analysis, a model which can replicate the performance of the array (in terms of the field characteristics) will be useful even if it gives little insight into the actual vibrational behaviour of the elements themselves. Such a model would allow predictions to be made about the performance of other arrays which have been constructed similarly and of similar materials, but which may be based upon a different layout of elements or have different phase-defined focal depths or positions.

The present study took the mode considered in section 7.3 and looked at the impact of changing the magnitude of the phase variation across the surface while keeping the same axisymmetric sinusoidal geometry. Fifteen configurations were considered, and for each of these the phase variation across the surface of an element is shown in figure 7.14. These ranged from having phase of vibration at the

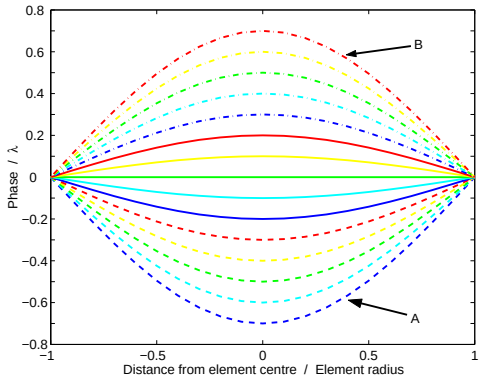

Figure 7.14: Plot of the 15 different configurations of the phase of vibration across the face of each element used in the simulations of the fifteen element array. For each configuration, the phase variation across the surface of the element was sinusoidal and axisymmetric, with the centre of the element leading or trailing the edge. The two extreme configurations are labelled: A indicates the configuration where the phase of vibration at the centre of each element trailed the edge by 0.7λ, while B indicates the configuration where the phase of vibration at the centre of each element led the edge by 0.7λ. The curves between A and B represent the 13 other phase configurations.

centre of each element which trailed the edge by 0.7λ (labelled A in figure 7.14) to having a phase of vibration at the centre which led the edge by 0.7λ (labelled B in figure 7.14). For each of the 15 configurations, simulations of the field produced by the fifteen element array were performed with phase-defined focal depths of 60, 80 and 100 mm.

The simulated fields were analysed using the same techniques applied to the results in section 7.3 in order to study the impact of the phase variation on the pressure distribution in the near-field and on the position of the focal zone, and the results of this analysis are summarised in figure 7.15.

Figure 7.15a illustrates the difference between σ_{sim} (the Rayleigh distribution σ obtained for the simulation near-field pressure distributions) and σ_{expt} (the Rayleigh distribution σ obtained for the experimental near-field pressure distributions) for the 15 phase configurations considered by the simulations. The horizontal black line at $\Delta\sigma_{sim-expt} = 0$ indicates the point where the simulation matches the

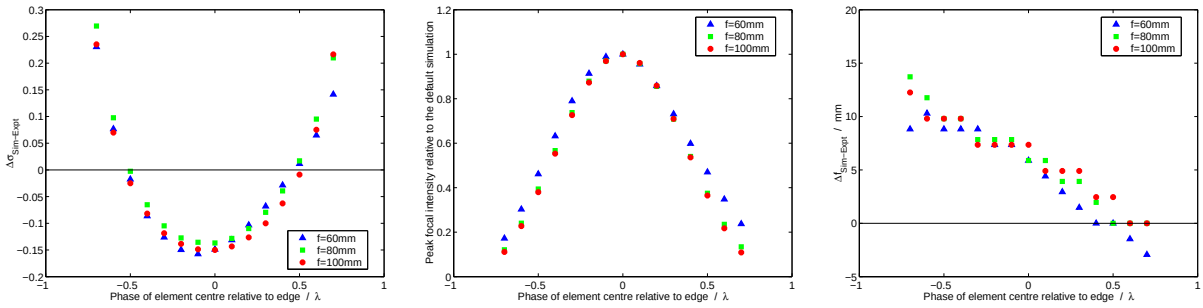

Figure 7.15: Graphs showing the effect of changing the magnitude of the phase variation across the face of each element on (a) the value of the Rayleigh distribution σ, (b) the peak focal intensity and (c) the position of the focal peak.

experimental pressure distributions, at which σ_{sim} and σ_{expt} are equal. The lowest value of σ_{sim} occurred for simulations where the elements vibrated with a piston-like motion, with no variation in the phase across the element surface. At this point, σ_{sim} was approximately 0.14 less than σ_{expt}. As the magnitude of the phase variation increased, the distribution of pressures in the near-field changed and σ_{sim} increased until good agreement with σ_{expt} was achieved for simulations where the phase of vibration at the centre of each element either led or trailed the edge of the element by $\frac{\lambda}{2}$.

Figure 7.15b shows the peak focal intensities for the 15 phase configurations considered by the simulations, showing that the addition of the secondary mode of vibration results in a decrease in the focal intensity. In fact, this reduction in the focal intensity is the underlying cause of the change in $\Delta\sigma_{sim-expt}$ shown in figure 7.15a. This can be explained as follows: If the peak focal pressure decreases then the distribution of pressures in the region of interest (shown in figure 7.8b for the default simulation) changes, because the pressures in this distribution are normalised against the peak focal pressure; The consequence of this is that σ_{sim}, which defines the Rayleigh fit to the pressure distribution, increases as the peak focal pressure decreases; This increase in σ_{sim} brings σ_{sim} closer to σ_{expt}, therefore causing a reduction in $\Delta\sigma_{sim-expt}$ for lower peak focal pressures.

Figure 7.15c shows the relationship between the position of the focal region and the phase variation across the element surface. In this plot, the difference between f_{sim} (the depth of the focal peak in the simulated fields) and f_{expt} (the depth of the focal peak in the experimental fields) are shown for the 15 phase configurations considered by the simulations. Again, the horizontal black line at $\Delta f_{sim-expt} = 0$ indicates the point where the simulation matches the experimental focal depths (i.e. the point at which $f_{sim} = f_{expt}$). The figure shows that the focal depth decreases approximately linearly as the phase difference between the centre and edge of each element is increased. Good agreement with f_{expt} was achieved for simulations where the phase of vibration at the centre of each element led the edge by $\frac{\lambda}{2}$.

From figures 7.15a and 7.15c it can be observed that the experimental data was matched by the simulations in terms of both the pressure distribution and the focal position when the phase of vibration at the centre of each element led the edge by $\frac{\lambda}{2}$. For this case, figure 7.16 illustrates the simulated field with the array focussed to a depth of 80 mm. The 2-D intensity profile (figure 7.16a) shows numerous maxima between the transducer surface and the focal zone similar to those apparent in the experimental profile (figure 6.7e), while the position of the peak is in good agreement with the experimental profile (figure 7.16b). The pressure distribution in the region of the field bounded by the outermost edges of the array, and at depths of less than half the focal distance is shown in figure 7.16c in comparison to the experimental distribution.

Finally, simulations were performed to look at the impact of non piston-like element vibration on the peak intensity as the focus is steered away from the central axis of the array, since that is the final aspect in which the default simulations differed from the experimental data (section 6.7). Simulations were performed with the phase of vibration at the centre of each element leading the edge by $\frac{\lambda}{2}$, since that was the setting which provided the best fit to the experimental data in terms of the pressure distribution in the near-field and the on-axis focal position (figure 7.16). The results were compared against the experimental off-axis focal intensities

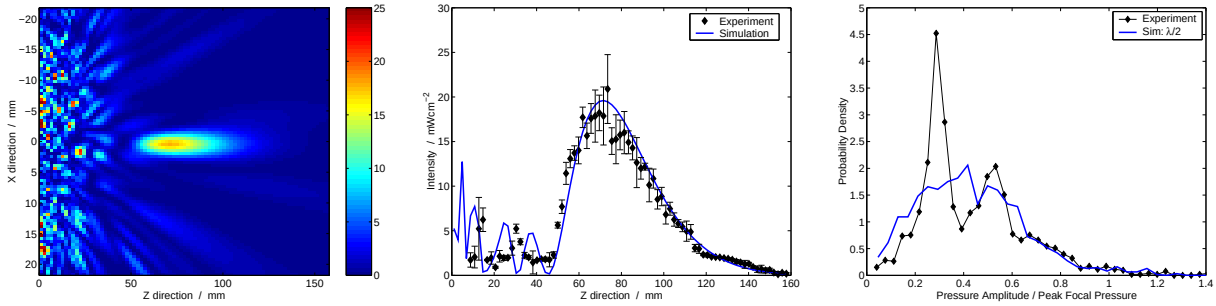

(a) *(b)* *(c)*

Figure 7.16: (a) Simulation results for the fifteen element array where the phase at the centre of each element led the edge of the element by $\frac{\lambda}{2}$ in order to provide the best agreement with the experimental results. Results are shown for a focal depth of 80mm. (a) 2-D intensity profile. The array is positioned at the left hand side with the ultrasound propagating left to right. The colours indicate the intensity in $mWcm^{-2}$. (b) Intensity profile along the central axis of the array. (c) Comparison between the simulated and experimental pressure distributions in the region of the field bounded by the outermost edges of the array, and at depths of less than half the focal distance.

discussed in section 6.5, and are summarised in table 7.1. The results in the table demonstrate that the inclusion of non piston-like element vibration resulted in a smaller decrease in the focal intensity with distance steered away from the central axis of the array in comparison to the default (piston-like) simulations, giving improved agreement with the experimental data.

This analysis indicates that imperfections in the piston-like behaviour of the transducer elements are the likely origin of the intensity 'hot-spots' in the near-field. The behaviour of the elements is independent of the medium and therefore it is to be anticipated that the intensity 'hot-spots' would also also exist in an inhomogeneous tissue medium. However, the pattern of the distribution in an inhomogeneous medium could be very different from that in a homogeneous medium, and a Rayleigh distribution may no longer provide a suitable model for the distribution of pressures in tissue. In addition, it is also worth noting that real tissue contains a significant density of small inhomogeneities less than a wavelength in size, and these will scatter the ultrasound and may have the effect of averaging out the 'hot-spots'. Future

Table 7.1: Peak focal intensity with distance steered away from the central axis of the array. The table lists the focal intensities relative to the on-axis case for fields focussed to a depth of 80 mm, and to distances of 0, 10 and 20 mm away from the central axis of the array. The experimental values represent the median and standard deviation of the measurements at the focal peak. In the non piston-like simulations, the centre of each element led the edge by $\frac{\lambda}{2}$, as illustrated in figure 7.6.

Distance away from the central axis	**Peak focal intensity relative to the on-axis peak focal intensity**		
mm	Experiment	Simulation (Piston-like)	Simulation (Non piston-like)
0	1.00	1.00	1.00
10	1.07 $\pm$ 0.18	0.78	0.90
20	0.82 $\pm$ 0.14	0.35	0.67

work will require the development of a suitable model to enable the ultrasound field within an inhomogeneous tissue medium to be computed, allowing the impact of changing from a homogeneous to an inhomogeneous field to be studied, along with the impact this will have on the performance and design of the array.

7.4.2 Inter-element crosstalk

While the first stage of the sensitivity analysis (section 7.3) indicated that the impact of inter-element crosstalk on the field produced by the fifteen element array was negligible, the question remained as to whether the effect of crosstalk would become significant in arrays with a greater number of elements. To investigate this, simulations were run to investigate the impact of crosstalk within an array of 60 elements each of radius 2 mm, randomly distributed within an array radius of 22 mm.

Figure 7.17a illustrates the layout of the simulated array (which is the same layout as that used for the random array in section 3.5.3), while figures 7.17b and 7.17c illustrate the probability density of inter-element pitches and angles respectively, demonstrating the lack of periodicity in the array. The elements were spaced

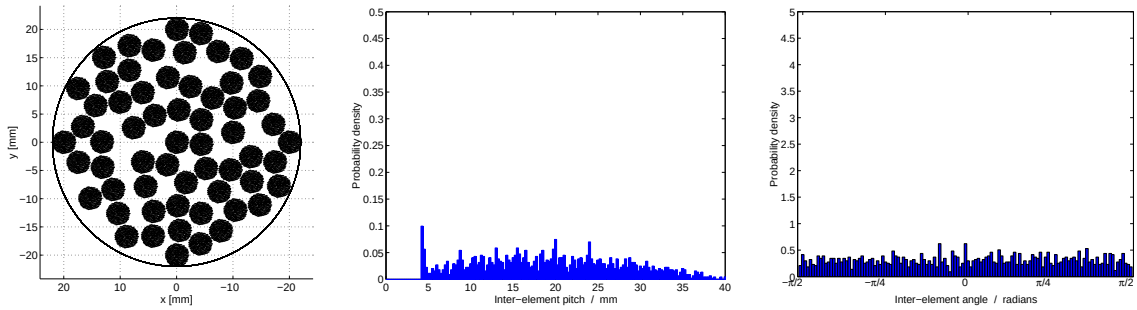

(a) *(b)* *(c)*

Figure 7.17: The array configuration used to study the impact of crosstalk within an array of 60 closely spaced elements arranged in a random layout. (a) Array layout. (b) The spectrum of inter-element pitches, where the probability density is quantised with a bin width of 0.25 mm. (c) The spectrum of inter-element angles, where the probability density is quantised with a bin width of $\frac{\pi}{128}$ radians.

close together with a minimum inter-element pitch of 4.3 mm. As shown by the experimental results discussed in section 6.3.2, such a small element spacing results in acoustic coupling between adjacent elements. The method of including crosstalk in the simulations therefore needs to be modified from that used in section 7.3, which related to electrical coupling, to a new method suitable for acoustic coupling.

As described in section 7.3.1, to take crosstalk into account the vibration of a single element within the array can be calculated by taking the sum of its own drive signal and the contributions from each of the other elements in the array. Equation 7.2 described the calculation of the effective drive voltage on an element when crosstalk from other elements in the array was due to electrical coupling alone. If the crosstalk is due to acoustic rather than electrical coupling then this equation must be modified to take into account an additional phase delay due to the time taken for the acoustic wave to propagate between the pair of elements in question. For the case where crosstalk from other elements in the array is due to acoustic coupling alone, the effective drive voltage $\overrightarrow{V_{effective}}$ on an element can be calculated as shown in equation 7.6, where the original drive signal to the element $\overrightarrow{V_{drive}}$ is modified by the acoustic crosstalk signal from each of the N elements. The crosstalk contribution from element n is given by the product of b_n, a number between 0 and 1

representing the strength of the crosstalk signal from that element, and $\overrightarrow{V_n}$, the drive signal applied to element n. Equation 7.6 considers each voltage as a vector, allowing the phase of each to be included in the consideration. The term $e^{i\theta_n}$ modifies the phase of the crosstalk signal to include the delay due to the time taken for the acoustic wave to propagate between the pair of elements in question. θ_n is defined as shown in equation 7.7, where f is the frequency of vibration, d_n is the distance between the two elements and c is the speed of sound in the material between the two elements.

$$\overrightarrow{V_{effective}} = \overrightarrow{V_{drive}} + \sum_{n=1}^{N} e^{i\theta_n} b_n \overrightarrow{V_n} \tag{7.6}$$

$$\theta_n = 2\pi f \frac{d_n}{c} \tag{7.7}$$

For these simulations cross-coupling was included between pairs of elements where the inter-element pitch was no greater than 8 mm, while cross-coupling between pairs of elements where the inter-element pitch was greater than 8 mm was neglected. This was done to approximate the finding from the experimental crosstalk measurements (section 6.3), that the electrical coupling between pairs of elements with a pitch greater than 8 mm was small in comparison with the acoustic coupling between pairs of elements with a pitch less than 8 mm. For each element within the 60 element array, an average of 6.1 neighbouring elements lay within this 8 mm distance.

For element pairs spaced less than 8 mm apart the simulations assumed that the strength of the cross-coupling was independent of distance. While this is not strictly true (figure 6.3b suggests that the coupling is stronger at shorter element spacings) the large range in the strength of the cross-coupling for pairs of elements with the same inter-element pitch means that obtaining a meaningful relationship between pitch and the strength of the cross-coupling is difficult. The assumption that the strength of the cross-coupling between closely spaced elements is independent of distance allows the situation to be simplified, yet will still provide an insight into the effect of acoustic coupling on the field produced by the array.

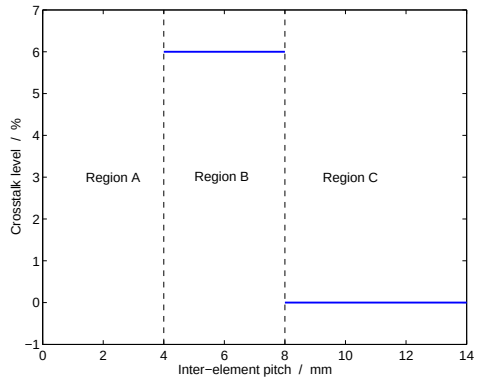

Figure 7.18: Plot showing the strength of the simulated crosstalk between pairs of elements against the inter-element pitch. The plot is divided into three regions: In region A there is no data, since the array contains no element-pairs with a pitch of less than 4 mm (which is twice the element radius of 2 mm); In region B, which extends from inter-element pitches of 4 to 8 mm, the magnitude of the received crosstalk signal is constant, and for this example is equal to 6% of the drive signal; In region C, which comprises of inter-element pitches greater than 8 mm, no crosstalk was applied.

Figure 7.18 summarises the crosstalk configuration used in these simulations. For element pairs with an inter-element pitch between 4 and 8 mm the magnitude of the crosstalk was constant, as can be seen in region B in the figure. Simulations were performed to investigate the impact of four different strengths of acoustic cross-coupling with region B: 0%, 2%, 4% and 6%. In comparison, the experimental measured acoustic crosstalk between closely spaced elements (section 6.3.2) was at most 1.5% of the drive signal. The range of simulated crosstalk magnitudes therefore studied crosstalk up to a level somewhat greater than that measured experimentally.

Simulations were performed for fields focussed to depths of 60, 80 and 100 mm on the central axis of the array, and the results were analysed to look at the effect of acoustic crosstalk on the pressure distribution close to the array surface and on the depth of the focal region. The results of this analysis are illustrated in figure 7.19. It was found that the crosstalk had little effect on the pressure distribution close to the array surface, since there was little change in the Rayleigh distribution σ as the strength of the crosstalk was increased (figure 7.19a). Figure 7.19b illustrates

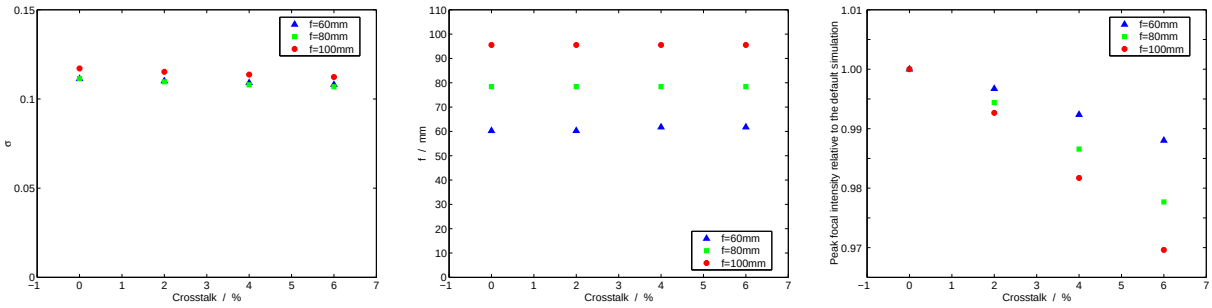

(a) *(b)* *(c)*

Figure 7.19: Graphs showing the effect of changing the strength of the simulated crosstalk between pairs of elements on (a) the value of the Rayleigh distribution σ, (b) the position of the focal peak and (c) the peak focal intensity.

that there was also little change in the depth of the focal region as the strength of the crosstalk increased. Figure 7.19c indicates that the focal intensity decreased as the strength of the crosstalk increased, but that the change was small. When the strength of the cross-coupling was 6%, which is significantly stronger than the acoustic crosstalk measured experimentally in section 6.3, the focal intensity was only between 1 and 3% lower (depending on focal depth) than in the simulations with no crosstalk.

In summary, the results indicate that crosstalk at levels similar to those measured experimentally will have little effect on the field produced by an array composed of a greater number of elements.

7.5 Summary

In summary, simulations were performed to investigate the origin of the differences between the experimentally measured and the simulated fields which were highlighted in chapter 6. While the impact of several factors was investigated, the characteristics of the experimental data could only be reproduced in the simulations by incorporating non piston-like vibration of the elements.

Further simulations investigated the addition of non piston-like vibration in greater detail, demonstrating that the inclusion of this factor can provide good

agreement between the simulated and experimentally measured fields in terms of the focal position, the distribution of pressures in the near-field, and the focal intensity for fields focussed away from the central axis of the array. While the non piston-like vibrational mode considered here is one possible mode that may affect the elements in the physical array, it may not be the same as the actual vibrational mode(s). However, it does enable the simulation tool to model the performance of the actual array, providing a means of predicting the behaviour of other arrays based on a similar structural design. In chapter 8 this is done to consider potential array designs and drive requirements for a device suitable for use in a clinical context.

Finally, results indicate that crosstalk at levels similar to the crosstalk measurements described in section 6.3 will have negligible effect on the field produced by an array composed of a greater number of elements.

Chapter 8

Feasibility for *in-vivo* applications

8.1 Introduction

The simulation and experimental results discussed so far have been limited to relatively low intensity focussed fields in a water medium. In this chapter, the feasibility of developing an array based on the same design scheme but intended for *in-vivo* applications will be considered.

8.2 Prediction of the focal intensity in tissue

The measurements of the focal intensity produced the fifteen element array in chapter 6 were made in a water-filled acoustic tank, and are therefore greater than the intensities that would be produced in deep tissue due to the difference in the attenuation coefficients for the two media. However, the feasibility of developing a device intended for clinical use based on the same design scheme as the fifteen element array can be investigated by using the measured intensity in water as a baseline from which predictions can be made of the intensities that could be achieved in tissue.

Many of the ultrasound transducers reported by other workers are aimed at HIFU applications, where the focal intensities are typically in the region of 1 $kWcm^{-2}$ [ter Harr, 1999] in order to raise tissue temperatures rapidly (within 1-2 seconds) to greater than 60 °C to ablate selected volumes of tissue. For hyperthermia

to be used in conjunction with chemotherapy or radiotherapy such high temperatures and rapid temperature rises are not required, and therefore lower intensities are more suitable. ter Harr [1999] gave the example that an intensity of 1 Wcm^{-2} at 1 MHz would lead to a temperature rise in liver of 2.88 $°Cmin^{-1}$, assuming that all attenuation is due to absorption and neglecting heat transport away from the tissue. In practice, heat conduction and blood flow will mean that a greater intensity is required to produce the same rate of temperature rise *in-vivo*. In addition, the focus will need to be steered around the tumour volume to ensure uniform heating, and this will necessitate still further increase in the focal intensity if the same rate of temperature rise is to be achieved throughout the tumour volume. To account for these factors, values of between 50 and 300 Wcm^{-2} (predicted by simulation) [Ibbini et al., 1987; Ju et al., 2003] have been proposed for the required focal intensity.

The peak focal intensity achieved by the fifteen element array when driven by a 1 MHz, 40 V peak-to-peak square wave was 23 $mWcm^{-2}$ at a depth of 60 mm in water. Taking into account the different attenuation coefficients of water and tissue (which are 0.0022 $dBcm^{-1}$ and approximately 0.5 $dBcm^{-1}$ respectively, as described in section 2.4), simulation shows that the fifteen element array would be capable of producing a peak focal intensity in tissue in the region of 11 $mWcm^{-2}$ when driven with the same drive conditions.

Clearly, this is well below the range of intensities suitable for hyperthermia. However, the experimental work described in chapter 6 demonstrated two straightforward routes by which the focal intensity can be increased without impacting on the geometry of the focal region:

1. Figure 6.2 demonstrated that the intensity measured in the far-field of a single element is proportional to the square of the drive voltage. Increasing the drive voltage of all elements in an array will therefore result in an increase in the focal intensity proportional to the square of the drive voltage increase.
2. Figure 6.9 showed that the focal intensity is proportional to the square of the number of elements. An additional benefit of this is that the intensities directly in front of each element at the array surface are reduced relative to

the focal intensity.

The focal intensity that could be achieved in tissue by an array composed of a large number of elements and driven by a high drive voltage can be predicted from these relationships, taking as a baseline the focal intensity of 11 $\mathrm{mWcm^{-2}}$ for the fifteen element array described above. As an example, a planar array of 60 circular elements, each of radius 2 mm and made of the same PZT-8 material, within an overall array radius of 22 mm would provide a peak focal intensity of 50 $\mathrm{Wcm^{-2}}$ at a depth of 60 mm in tissue ($\mu = 0.5$ $\mathrm{dBcm^{-1}}$) when driven by a square wave drive signal in the region of 675 V peak-to-peak. This example demonstrates that it should be possible to reach the lower end of the values reported for *in-vivo* hyperthermia using a practical array with a similar design to the fifteen element array, assuming that the medium remains linear and homogeneous at the higher field intensities.

However, other approaches would be needed to provide further increase in the focal intensity. Increasing the number of elements to greater than 60 becomes impractical if a random distribution of elements to be maintained, although a maximum of 91 elements is possible using a regular close-packed layout. Also, the prediction requires that the intensity is proportional to the square of the drive voltage at voltages up to 675 V, although in section 6.2 the relationship was confirmed only up to 280 V since that was the maximum that could be supplied by the present equipment. The use of drive voltages of a similar range has been reported by other workers such as Sokka and Hynynen [2000], who reported an intra-cavitary ultrasound array intended for prostate ablation where the device was designed to handle drive voltages of up to 500 V peak-to-peak.

Other potential routes towards increasing the focal intensity include the following:

1. Increasing the size of the elements in the array would increase the focal intensity (if the number of elements remains constant), since the focal intensity is proportional to square of the individual element area (equation 3.8). This

would require the array radius to be modified in order to satisfy equation 3.7, which would in turn result in an increase in the volume of the focal region according to the equations in 3.2. While the desirability of an increase in the dimensions of the focal region depends upon the geometry of the region being treated, a larger focal volume would make it easier to achieve hyperthermia due to the increase in the total power deposited in the tissue. The relationship between the element size and the geometry of the focal region will be discussed further in section 8.3.

2. Modification of the array construction design to inhibit non piston-like modes of vibration would be beneficial. As indicated in 7.15b the inclusion of non piston-like vibration (with the centre of each element leading the edge by 0.5λ) resulted in the focal intensity decreasing by approximately 60%. Further work would be required to look at the feasibility of this.

3. The addition of electrical impedance matching could improve the efficiency of the system and reduce the drive voltage requirements. Further experimental work would be required to quantify the potential benefits of this. However, impedence matching does have the disadvantage of making precise phase control of the drive signals more difficult. However, the results of the sensitivity analysis (section 7.3.2) suggest that the field produced by a phased array is likely to be tolerant of errors of $\sim$1% in the phase of the drive signals, since 6-bit quantisation of the phase had no impact on the field.

8.3 Proposed design improvements

The experimental results discussed in section 6.5 showed that while the fifteen element array was capable of creating a focus away from the central axis of the array, the intensity of the focus decreased the further off-axis it was moved. In addition, under steering the grating lobes became more prominent in comparison to the focus. This behaviour is not ideal as it will complicate the control mechanism required to maintain a constant temperature within the target region, since the intensity and

geometry of the focal region depends not only on depth, but also on steering angle. Removing this dependency on steering angle will reduce the complexity of the control problem.

The array design can be modified to ensure that the focal intensity and shape remain constant under steering, without any increase in the grating lobe intensities, by following the design approach illustrated in figure 8.1. Figure 8.1 illustrates a planar array of circular elements with an overall array diameter larger than that required for focussing to the target depth, and with the elements distributed randomly across the face of the array. To produce a focussed field, only a subset of the elements within the array would be driven. Figure 8.1a illustrates the subsets of elements that would be driven for focussing to depths of 60, 80 and 100 mm along the central axis of the array. Only the elements within a radius a_{sub} from the projection of the focal position onto the array surface are included within the subset, where a_{sub} is defined by equation 8.1 for a focal depth f, element radius a_{el}, and ultrasonic wavelength λ with the medium. (Equation 8.1 can be derived from equation 3.6 by substituting a_{sub} for a_{arr} and setting $\Delta Path_{max} = \frac{\lambda}{2}$.)

$$a_{sub} = \frac{\lambda f}{\sqrt{4a_{el}^2 - \lambda^2}} \tag{8.1}$$

This design approach is similar to that described by Seip et al. [2003] in their discussion of arrays for intra-cavitary HIFU applications. They reported simulations of an array where depth control and steering along the longitudinal axis of their array was achieved by driving only a subset of elements, which they called a 'sub-aperture', with their objective being to eliminate off-axis steering gain loss. However, a similar approach for a 2-D extra-corporeal would provide additional benefits which will be described in the present section.

For focussing away from the central axis of the array, a different subset of elements would be selected, as indicated in figure 8.1b for a focal position 10 mm to the side of the array's central axis of symmetry at depths of 60, 80 and 100 mm. The advantages of this design approach are that under steering, the intensity and geometry of the focal region and the intensity and geometry of the grating lobes

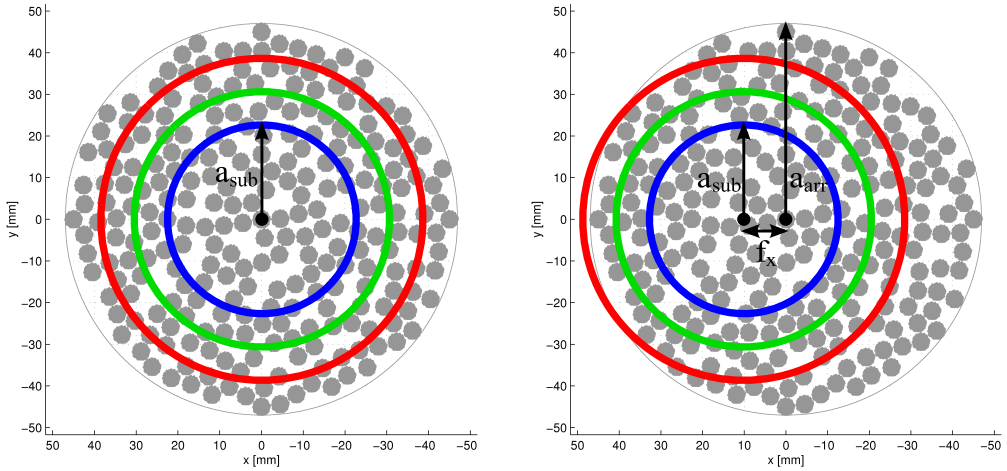

(a) *(b)*

Figure 8.1: Proposed design approach for a planar array where the focal geometry is independent of the focal position. In this example, the array radius a_{arr} is 47 mm, the element radius a_{el} is 2 mm and the total number elements in the array is 250. A limited subset of the elements is activated depending on the required position of the focal region: the elements within the blue (inner), green (middle) and red (outer) circles correspond to the active elements for focussing to depths of 60, 80 and 100 mm respectively. The subset of selected elements is different for (a) on-axis focussing and (b) off-axis focussing (in this case, to a position 10 mm off-axis).

remain constant. In addition, for an array in a non-attenuating medium the focal dimensions are unaffected by focal depth. Instead, the focal dimensions are defined by the element radius alone as shown in equations 8.2 and 8.3 for the -3 dB length (L_{-3dB}) and width (W_{-3dB}) of the focal region respectively. As an example, for an array designed to create a focal region region within a hypothetical tumour of diameter 40 mm (as described in section 1.4), equation 8.2 can be used to indicate that an element radius of approximately 3 mm or less should be used.

$$L_{-3dB} \approx 8.1 \left(\frac{a_{el}^3}{\lambda} \right)^{\frac{1}{2}} \tag{8.2}$$

$$W_{-3dB} \approx 1.1 \left(\frac{a_{el}^3}{\lambda} \right)^{\frac{1}{4}} \tag{8.3}$$

The geometry of the field close to the array surface will be affected by steering, due to the selection of different subsets of elements for each focal position. That is, the positions of the local maxima and minima close to the array surface will change according to the particular subset of elements in use. This would be beneficial since it would make the heating in this region more uniform, rather than being concentrated in a number of fixed locations.

The maximum focal depth f_z of the array is limited by the array geometry as shown in equation 8.4, while the lateral steering distance from the central axis f_x is limited by equation 8.5, where a_{arr} is the overall array radius. These equations indicate that the focus can be positioned anywhere within a cone whose base is given by the array edge and whose peak is given by the maximum focal depth f_{zmax}. Inside this cone, the geometry of the focal region is independent of the focal position, while the intensity is dependent only on the focal depth f_z. Steering to positions outwith the cone is possible, but will result in a deterioration of the focal geometry and intensity similar to the changes under steering that were described in section 6.5.

$$f_z \leqslant \frac{a_{arr}}{\lambda} \sqrt{4a_{el}^2 - \lambda^2} \tag{8.4}$$

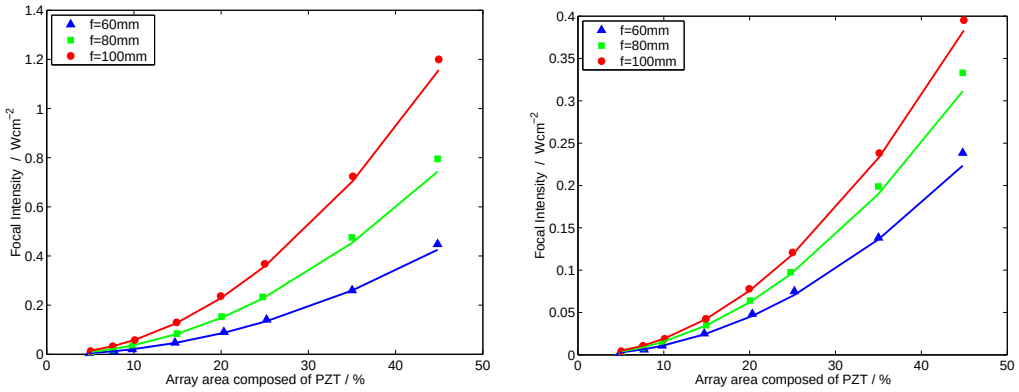

Figure 8.2: Peak focal intensity for an array of 4 mm diameter elements in a medium of (a) water and (b) tissue with each simulated element functioning non piston-like behaviour. The points indicate the simulation results, while the lines indicate the least-squares best fit to a square relation. The results have been calibrated using the experimental result from the fifteen element array focussed at a depth of 60 mm.

$$f_x \leqslant a_{arr} - a_{sub} \tag{8.5}$$

Simulations were performed for the array illustrated in figure 8.1 to investigate the relationships between the focal intensity and the focal depth, and the focal intensity and the density of elements in the array. The simulations included the effect of non piston-like behaviour using the technique discussed in section 7.4.1, such that the phase at the centre of each element led the edge sinusoidally by $\frac{\lambda}{2}$, and were performed for two homogeneous media: water and tissue. Figure 8.2 shows how the simulated peak focal intensities varied with element density and with focal depth in water (figure 8.2a) and tissue (figure 8.2b). The results demonstrate the focal intensity is greater at deeper focal depths, and this is a consequence of fact that a larger number of elements can be included within the active subset for deeper focussing.

The major disadvantage of this design approach is that the large number of elements in the array would require drive electronics providing a large number of drive channels. However, the number of elements could be reduced somewhat from

that of the example illustrated in figure 8.1 by increasing the element diameter, depending on the required focal dimensions. Also, drive electronics could be designed with a total number channels less than the total number of elements in the array, since only a subset of elements would be active at any one time.

Chapter 9

Conclusions

The research presented in this thesis has identified the scientific foundations that have the potential to lead to a transducer suitable for the creation of mild hyperthermia in deep body tumours. Several areas have been considered, and the main conclusions from each will be described here.

In chapter 3 simulation was used to determine the relationship between the design of a phased array and the characteristics of the field produced by the array. This study was necessary because although much research has been carried out by other workers in the field of transducer design (section 1.3.2), many of the conclusions from those studies apply specifically to the particular array design in question and cannot be applied more generally to other array configurations. Within this thesis, distinction has been made between two different types of parameter which define phased arrays: [i] Fundamental array parameters (such as the array diameter, radius of curvature and operating frequency); and [ii] Secondary array parameters (such as the individual element size, number density and layout geometry). Consideration of the fundamental array parameters alone has provided a new set of general equations which enable the geometry of the field produced by an idealised array to be related to the parameters which define the overall array geometry, keeping separate the impact of the secondary design parameters. These secondary parameters modify the field from the idealised case, and further simulations enabled the impact of these factors to be examined. This approach has led to the definition of a new upper limit which can be placed on the element size within an array (equation 3.7), providing a general rule which is applicable to any planar phased array. In addition, the simula-

tions have demonstrated the benefits of distributing the elements randomly within the array, confirming the observations of Goss et al. [1996] and Gavrilov and Hand [2000] that a random layout minimises the intensities of the grating lobes under steering. The results reported in section 3.5.4 also demonstrated that increasing the number density of elements also provides a reduction in the intensities of the grating lobes relative to the focal region, while having no impact on the geometry of the focal region.

The construction of a fifteen element phased array based on the design principles established within the simulation work was described in chapter 4, demonstrating a method of constructing robust arrays which are potentially suitable for clinical applications. In contrast to many of the transducer designs of other workers (discussed in section 1.3.2), the construction process described in the present work is relatively simple, requiring no machining of the PZT to form the elements in the array. Measurement of the inter-element cross-coupling (section 6.3) demonstrated that the crosstalk within the fifteen element array was primarily due to electrical coupling, while closer element spacings would lead to acoustic coupling becoming dominant. However, the crosstalk measured between pairs of closely spaced elements was typically less than 1.5% of the drive signal, and would have negligible impact on the field produced by large arrays manufactured using the same construction process (section 7.4.2).

In chapter 6 comparison was made between experimentally measured and simulated fields from the fifteen element array, demonstrating that there was good agreement in certain aspects (such as in the geometries of the focal region and grating lobes), while also revealing several differences between measured and simulated fields. In particular, the focal region was closer to the surface of the physical transducer in the measured fields compared to the simulation results, and there were numerous small high intensity regions between the surface of the transducer and the focus which were absent from the simulation fields. Since there is no existing standard technique of analysing the region of the field between the surface of the array and the focal zone, a new method was devised to characterise the distribution

of pressures by fitting a Rayleigh distribution to the data (section 5.5.2). Section 6.6 demonstrated the use of this technique as a method of quantitative comparison between experimental and simulated pressure distributions.

No standard methods have been reported for the investigation of the origin of differences between experimentally measured and simulated fields. In chapter 7 of this thesis the sensitivity of the array to a number of factors has been investigated through a simulated factorial experiment, in order to identify the factors which have the potential to cause the effects observed in the experimental data. This analysis indicated that the presence of a secondary vibrational mode within the elements of the array was the principal cause for both the shift in the position of the focus and for the unwanted maxima close to the surface of the array. While the impact of non piston-like vibrational modes on the field produced by single elements has been studied in the past [Hutchins et al., 1986], the impact of such modes on phased arrays has not.

Finally, the feasibility of the design approach described in this thesis for clinical applications was demonstrated. Extrapolation of the experimental results indicated that an array of 60 elements, based on the design described, driven by 675 V peak-to-peak pulses would be capable of producing a peak focal intensity of 50 Wcm^{-2} at a depth of 60 mm in tissue, which is within the lower range of intensities appropriate for mild hyperthermia. Possible modifications to the array design have also been proposed, describing a design approach similar to that suggested by Seip et al. [2003] for intra-cavitary applications, using a large array where only limited subsets of elements are activated at any one time. In addition to the observation made by Seip et al. [2003] that such a design eliminates off-axis steering gain loss, the present work also demonstrated other improvements in field characteristics, in terms of a constant focal geometry being maintained independent of the position of the focus, and the avoidance of grating lobes under steering.

In summary, the research presented in this thesis has examined the underlying principles governing the characteristics of the field produced by phased array transducers. Experimental measurements have verified these relationships, and cal-

culations based on the experimental results have demonstrated the feasibility of constructing an array suitable for clinical application of mild hyperthermia in deep tumours.

References

Arora D, Cooley D, Perry T, Skliar M, and Roemer RB. Direct thermal dose control of constrained focused ultrasound treatments: phantom and in vivo evaluation. *Phys Med Biol*, 50:1919–1935, 2005.

Assaad J and Bruneel C. Radiation from finite phased and focused linear array including interaction. *J Acoust Soc Am*, 101:1859–1867, 1997.

Bacon DR. Finite amplitude distortion of the pulsed fields used in diagnostic ultrasound. *Ultrasound Med Biol*, 10(2):189–195, 1984.

Baronozio GF and Hager ED, editors. *Hyperthermia in cancer treatment: A primer*, chapter 22 - Future perspectives of interstitial and perfusional hyperthermia, pages 338–360. Springer, 1998a. ISBN 0-387-33440-8.

Baronozio GF and Hager ED, editors. *Hyperthermia in cancer treatment: A primer*, chapter 4 - Thermotherapy and Nanomedicine, pages 60–63. Springer, 1998b. ISBN 0-387-33440-8.

Benkeser PJ, Pao TL, and Yoon YJ. Ultrasonic phased array controller for hyperthermia applications. *Ultrasonics*, 29:85–88, January 1991.

Berlincourt D. Piezoelectric ceramic compositional development. *J Acoust Soc Am*, 91(5):3034–3040, 1992.

Bold RJ, Termuhlen PM, and McConkey DJ. Apoptosis, cancer and cancer therapy. *Surg Oncol*, 6(3):133–142, 1997.

Brizel DM, Dodge RK, Clough RW, and Dewhirst MW. Oxygenation of head and neck cancer: changes during radiotherapy and impact on treatment outcome. *Radiother Oncol*, 53:113–117, 1999.

Cahill MD and Baker AC. Increased off-axis energy deposition due to diffraction and nonlinear propagation of ultrasound from rectangular sources. *J Acoust Soc Am*, 102(1):199–203, July 1997.

Cain CA and Umemura S-I. Concentric-ring and sector-vortex phased-array applicators for ultrasound hyperthermia. *IEEE Trans Microwave Theory Tech*, 34(5): 542–551, 1986.

Cassereau D and Fink M. Time reversal of ultrasonic fields - part III: Theory of the closed time-reversal cavity. *IEEE Trans Ultrason Ferroelectr Freq Control*, 39(5): 579–592, 1992.

Cathignol D, Birer A, Nachef S, and Chapelon J. Electronic beam steering of shock waves. *Ultrasound Med Biol*, 21(3):365–377, 1995.

Clement GT and Hynynen K. Field characterization of therapeutic ultrasound phased arrays through forward and backward planar projection. *J Acoust Soc Am*, 108(1):441–446, July 2000.

Coley WB. Contribution to the knowledge of sarcoma. *Ann Surg*, 14(3):199–220, September 1891.

Curie J and Curie P. Développement, par pression de l'électricité polaire dans les cristaux hémièdres à faces inclinées. *C R Hebd Seances Acad Sci*, 91:294–295, 1880.

Curley SA. Radiofrequency ablation of malignant liver tumours. *The Oncologist*, 6: 14–23, 2001.

Damianou CA, Sanghvi NT, Fry FJ, and Maass-Moreno R. Dependence of ultrasonic attenuation and absorption in dog soft tissues on temperature and thermal dose. *J Acoust Soc Am*, 102(1):628–634, July 1997.

Daum DR and Hynynen J. A 256-element ultrasonic phased array system for the treatment of large volumes of deep seated tissue. *IEEE Trans Ultrason Ferroelectr Freq Control*, 46(5):1254–1268, September 1999.

Deardorff DL and Diederich CJ. Ultrasound applicators with internal water-cooling for high-powered interstitial thermal therapy. *IEEE Trans Biomed Eng*, 47(10): 1356–1365, October 2000.

Debicki PS, Okoniewski M, Okoniewska E, Shrivastava PN, Debicka AM, Baert LV, and Petrovich Z. Cooled microwave transrectal applicator with adjustable directional beam for prostate treatment. *Int J Hyperthermia*, 11(1):95–108, 1995.

Dekker DL, Piziali RL, and Dong Jr. E. Effect of boundary conditions on the ultrasonic-beam characteristics of circular disks. *J Acoust Soc Am*, 56(1):87–93, July 1974.

Dewhirst MW, Viglianti BL, Lora-Michiels M, Hanson M, and Hoopes PJ. Basic principles of thermal dosimetry and thermal thresholds for tissue damage from hyperthermia. *Int J Hyperthermia*, 19(3):267–294, December 2003.

Dewhirst MW, Vujaskovic Z, Jones E, and Thrall D. Re-setting the biologic rationale for thermal therapy. *Int J Hyperthermia*, 21(8):779–790, December 2005.

di Filippo F, Anzà M, Rossi CR, Cavaliere F, Botti C, Lise M, Garinei R, Giannarelli D, Vasselli S, Zupi G, and Cavaliere R. The application of hyperthermia in regional chemotherapy. *Semin Surg Oncol*, 14:215–223, 1998.

Dias JF. An experimental investigation of the cross-coupling between elements of an acoustic imaging array transducer. *Ultrasonic Imaging*, 4:44–55, 1982.

Diederich CJ and Hynynen K. Ultrasound technology for hyperthermia. *Ultrasound Med Biol*, 25(6):871–887, July 1999.

Duck FA. Nonlinear acoustics in diagnostic ultrasound. *Ultrasound Med Biol*, 28: 1–18, 2002.

Duck FA, Baker AC, and Starritt HC, editors. *Ultrasound in Medicine*, chapter 2 - Nonlinear effects in ultrasound propagation, pages 23–38. IOP publishing, 1998a. ISBN 0-7503-0593-2.

Duck FA, Baker AC, and Starritt HC, editors. *Ultrasound in Medicine*, chapter 8 - Ultrasound Hyperthermia and the Prediction of Heating, pages 151–176. IOP publishing, 1998b. ISBN 0-7503-0593-2.

Ebbini ES and Cain CA. Multiple-focus ultrasound phased-array pattern synthesis: Optimal driving signal distributions for hyperthermia. *IEEE Trans Ultrason Ferroelectr Freq Control*, 36(5):540–548, September 1989.

Falk MH and Issels RD. Hyperthermia in oncology. *Int J Hyperthermia*, 17(1):1–18, 2001.

Fan X, Moros EG, and Straube WL. Acoustic field prediction for a single planar continuous-wave source using an equivalent phased array method. *J Acoust Soc Am*, 102(5):2734–2741, November 1997.

Fatehi D, van der Zee J, de Bruijne M, Franckena M, and van Rhoon GC. RF-power and temperature data analysis of 444 patients with primary cervical cancer: Deep hyperthermia using the Sigma-60 applicator is reproducible. *Int J Hyperthermia*, 23(8):623–643, 2007.

Fink M. Time reversal of ultrasonic fields - part I: Basic principles. *IEEE Trans Ultrason Ferroelectr Freq Control*, 39(5):555–566, 1992.

Fjield T, Fan X, and Hynynen K. A parametric study of the concentric-ring transducer design for MRI guided ultrasound surgery. *J Acoust Soc Am*, 100(2):1220–1230, 1996.

Ford RD. *Introduction to acoustics*, chapter 3 - Sound waves in three dimensions, pages 45–68. Elsevier, 1970. ISBN 0444-20078-9.

Gallego-Juárez JA. Piezoelectric ceramics and ultrasonic transducers. *J Phys E: Sci Instrum*, 22:804–816, 1989.

Gavrilov LR and Hand JW. A theoretical assessment of the relative performance of spherical phased arrays for ultrasound surgery. *IEEE Trans Ultrason Ferroelectr Freq Control*, 47(1):125–139, January 2000.

Goss SA, Frizzell LA, Kouzmanoff JT, Barich JM, and Yang JM. Sparse random ultrasound phased array for focal surgery. *IEEE Trans Ultrason Ferroelectr Freq Control*, 43(6):1111–1121, November 1996.

Griffin RJ, Okajima K, Barrios B, and Song CW. Mild temperature hyperthermia combined with carbogen breathing increases tumor partial pressure of oxygen (pO_2) and radiosensitivity. *Cancer Res*, 56:5590–5593, December 1996.

Guo N and Cawley P. Transient response of piezoelectric discs to applied voltage pulses. *Ultrasonics*, 29:208–217, May 1991.

Haertling GH. Ferroelectric ceramics: History and technology. *J Am Ceram Soc*, 82(4):797–818, 1999.

Hahn GM, Braun J, and Har-Kedar I. Thermochemotherapy: Synergism between hyperthermia (42-43°) and adriamycin (or bleomycin) in mammalian cell inactivation. *Proc Nat Acad Sci USA*, 72(3):937–940, March 1975.

Hall DE, editor. *Basic Acoustics*. Harper & Row, 1987.

Hildebrandt B, Wust P, Ahlers O, Dieing A, Sreenivasa G, Kerner T, Felix R, and Riess H. The cellular and molecular basis of hyperthermia. *Critical Reviews in Oncology/Hematology*, 43:33–56, 2002.

Hildebrandt B, Hegewisch-Becker S, Kerner T, Nierhaus A, Bakhshandeh-Bath A, Janni W, Zumschlinge R, Sommer H, Riess H, and Wust P. Current status of radiant whole-body hyperthermia at temperatures >41.5°C and practical guidelines for the treatment of adults. The German 'Interdisciplinary Working Group on Hyperthermia'. *Int J Hyperthermia*, 21(2):169–183, 2005.

Hill CR, Bamber JC, and ter Haar GR, editors. *Physical principles of medical ultrasonics*, chapter 1 - Basic acoustic theory, pages 1–40. Wiley, 2004a. ISBN 0-471-97002-6.

Hill CR, Bamber JC, and ter Haar GR, editors. *Physical principles of medical*

ultrasonics, chapter 4 - Attenuation and absorption, pages 93–166. Wiley, 2004b. ISBN 0-471-97002-6.

Hoffelner J, Landes H, Kaltenbacher M, and Lerch R. Finite element simulation of nonlinear wave propagation in thermoviscous fluids including dissipation. *IEEE Trans Ultrason Ferroelectr Freq Control*, 48(3):779–786, 2001.

Holm S. Ultrasim - a toolbox for ultrasound field simulation. *Nordic Matlab conference*, October 2001. URL `http://www.ifi.uio.no/~sverre/papers/01_Matlab.pdf`.

Holm S, Teigen F, Ødegaard L, Berre V, Erstad JO, and Epasinghe K. *Ultrasim user's manual version 2.1.* Department of Informatics, University of Oslo, April 1998.

Hu Z, Yang XY, Liu Y, Sankin GN, Pua EC, Morse MA, Lyerley HK, Clay TM, and Zhong P. Investigation of HIFU-induced anti-tumour immunity in a murine tumour model. *Journal of Translational Medicine*, 5(34), 2007.

Huang C-H, Lin Y-C, and Ma C-C. Theoretical analysis and experimental measurement for resonant vibration of piezoceramic circular plates. *IEEE Trans Ultrason Ferroelectr Freq Control*, 51(1):12–24, 2004.

Hutchins DA, Mair HD, Puhach PA, and Osei AJ. Continuous-wave pressure fields of ultrasonic transducers. *J Acoust Soc Am*, 80(1):1–12, July 1986.

Huttunen T, Kaipio JP, and Hynynen K. Modeling of anomalies due to hydrophones in continuous-wave ultrasound fields. *IEEE Trans Ultrason Ferroelectr Freq Control*, 50(11):1486–1500, November 2003.

Hynynen K. Present status of ultrasound hyperthermia. *IEEE Ultrasonics Symposium*, pages 941–946, 1988.

Ibbini M, Ebbini E, Umemura S-I, and Cain CA. Ultrasound phased arrays for hyperthermia: New techniques based on the field conjugation method. *IEEE Ultrasonics Symposium*, pages 863–866, 1987.

Iliakis G, Wu W, and Wang M. DNA double strand break repair inhibition as a cause of heat radiosensitization: Re-evaluation considering backup pathways of NHEJ. *Int J Hyperthermia*, 24(1):17–29, February 2008.

Johnson JE, Neuman DG, Maccarini PF, Juang T, Stauffer PR, and Turner P. Evaluation of a dual-arm Archimedean spiral array for microwave hyperthermia. *Int J Hyperthermia*, 23(6):475–490, September 2006.

Jones EL, Prosnitz LR, Dewhirst MW, Marcom PK, Hardenbergh PH, Marks LB, Brizel DM, and Vujaskovic Z. Thermochemoradiotherapy improves oxygenation in locally advanced breast cancer. *Clinical Cancer Research*, 10:4287–4293, July 2004.

Jones EL, Oleson JR, Prosnitz LR, Samulski TV, Vujaskovic Z, Yu D, Sanders LL, and Dewhirst MW. Randomised trial of hyperthermia and radiation for superficial tumors. *J Clin Oncol*, 23(13):3079–3085, May 2005.

Jordan A. Magnetic fluid hyperthermia (MFH): Cancer treatment with AC magnetic field induced excitation of biocompatible superparamagnetic nanoparticles. *Journal of Magnetism and Magnetic Materials*, 201:413–419, 1999.

Jorritsma JBM and Konings AWT. Inhibition of repair of radiation-induced strand breaks by hyperthermia, and its relationship to cell survival after hyperthermia alone. *Int J Radiat Biol*, 43(5):505–516, 1983.

Ju K-C, Chen Y-Y, Lin W-L, and Kuo T-S. One-dimensional phased array with mechanical motion for conformal ultrasound hyperthermia. *Phys Med Biol*, 48: 167–182, 2003.

Karayannidou EG, Achilias DS, and Sideridou ID. Cure kinetics of epoxyamine resins used in the restoration of works of art from glass or ceramic. *Eur Polym J*, 42:3311–3323, 2006.

Kaye GWC and Laby TH. *Tables of Physical and Chemical Constants*. Longman, 16th edition, 1995. ISBN 0-582-22629-5.

Kennedy JE, ter Haar GR, and Cranston D. High intensity focussed ultrasound: surgery of the future? *The British Journal of Radiology*, 76:590–599, September 2003.

Kerr JFR, Winterford CM, and Harmon BV. Apoptosis: Its significance in cancer and cancer therapy. *Cancer*, 73(8):2013–2026, April 1994.

King RJB, editor. *Cancer Biology*. Pearson Education Ltd., 2nd edition, 2000.

Knorr C, Meyer T, Janssen T, Goehl J, and Hohenberger W. Hyperthermic isolated limb perfusion (HILP) in malignant melanoma. experience with 101 patients. *EJSO*, 32:224–227, 2006.

Kong G and Dewhirst MW. Hyperthermia and liposomes. *Int J Hyperthermia*, 15 (5):345–370, 1999.

Koyuncu B. The investigation of high frequency vibration modes of PZT-4 transducers using ESPI techniques with reference beam modulation. *Opt Lasers Eng*, 1:37–49, 1980.

Krautkrämer J and Krautkrämer H. *Ultrasonic Testing of Materials*, chapter 6 - Attenuation of Ultrasonic Waves in Solids, pages 108–116. Springer-Verlag, 4th edition, 1990. ISBN 0-387-51231-4.

Lage H, Jordan A, Scholz R, and Dietel M. Thermosensitivity of multidrug-resistant human gastric and pancreatic carcinoma cells. *Int J Hyperthermia*, 16(4):291–303, 2000.

Lagendijk JJW. Hyperthermia treatment planning. *Phys Med Biol*, 45:R61–R76, 2000.

Lepock JR. Role of nuclear protein denaturation and aggregation in thermal radiosensitization. *Int J Hyperthermia*, 20(2):115–130, March 2004.

Lin W-L, Yen J-Y, Chen Y-Y, Jin K-W, and Shieh M-J. Relationship between acoustic aperture size and tumor conditions for external ultrasound hyperthermia. *Med Phys*, 26:818–824, 1999.

Liu X, Li J, Gong X, and Zhang D. Nonlinear absorption in biological tissue for high intensity focused ultrasound. *Ultrasonics*, 44:e27–e30, 2006.

Lohninger H. *Teach/Me Data Analysis*. Springer-Verlag, 1999. ISBN 3-540-14743-8.

Lovejoy A, Pedrick P, Doran A, Delchar TA, Mills JA, and Stamm A. A novel 8-bit ultrasound phased-array controller for hyperthermia applications. *Ultrasonics*, 33 (1):69–73, 1994.

Lucas BG and Muir TG. The field of a focusing source. *J Acoust Soc Am*, 72(4): 1289–1296, October 1982.

Ma J, Lowe MJS, and Simonetti F. Feasibility study of sludge and blockage detection inside pipes using guided torsional waves. *Meas Sci Technol*, 18:2629–2641, July 2007.

Main IG. *Vibrations and Waves in Physics*. Cambridge University Press, 3rd edition, 1993. ISBN 0-521-44701-1.

Mansouri A, Henle KJ, Benson AM, Moss AJ, and Nagle WA. Characterization of a cisplatin-resistant subline of murine RIF-1 cells and reversal of drug resistance by hyperthermia. *Cancer Res*, 49:2674–2678, May 1989.

Martin RW, Vaezy S, Proctor A, Lee JBJ, and Crum LA. Water-cooled, high-intensity ultrasound surgical applicators with frequency tracking. *IEEE Trans Ultrason Ferroelectr Freq Control*, 50(10):1305–1317, 2003.

Mason WP. *Physical acoustics - Principles and methods*, volume 2B - Properties of polymers and nonlinear acoustics, chapter 10 - Nonlinear acoustics, pages 231–264. Academic Press Inc., 1965.

Mast TD. Simplified expansions for radiation from a baffled cicular piston. *J Acoust Soc Am*, 118:3457–3464, 2005.

Meaney PM, Clarke RL, ter Haar GR, and Rivens IH. A 3-D finite-element model for computation of temperature profiles and regions of thermal damage during

focussed ultrasound surgery exposures. *Ultrasound Med Biol*, 24(9):1489–1499, 1998.

Meaney PM, Cahill MD, and ter Haar GR. The intensity dependence of lesion position shift during focused ultrasound surgery. *Ultrasound Med Biol*, 26(3): 441–450, 2000.

Mitsumori M, Hiraoka M, Okuno Y, Nishimura Y, Li YP, Fujishiro S, Nagata Y, Abe M, Koishi M, Sano T, Marume T, and Takayama N. A phase I and II clinical trial of a newly developed ultrasound hyperthermia system with an improved planar transducer. *Int J Radiation Oncology Biol Phys*, 36(5):1169–1175, 1996.

Mo J-H, Fowlkes JB, Robinson AL, and Carson PL. Crosstalk reduction with a micromachined diaphragm structure for integrated ultrasound transducer arrays. *IEEE Trans Ultrason Ferroelectr Freq Control*, 39(1):48–53, 1992.

Nakao K, Otsuki Y, Akao Y, Ito Y, Marukawa O, Tachibana S, Kawakami M, and Sasaki S. The synergistic effects of hyperthermia and anticancer drugs on induction of apoptosis. *Med Electron Microsc*, 33:44–50, 2000.

Nasoni RL, Bowen T, Dewhirst MW, Roth HB, and Premovich R. The speed of sound as a function of temperature in mammalian tissue. *IEEE Ultrasonics Symposium*, pages 1077–1082, 1980.

Nau WH, Diederich CJ, and Stauffer PR. Directional power deposition from direct-coupled and catheter-cooled interstitial ultrasound applicators. *Int J Hyperthermia*, 16(2):129–144, 2000.

Pain HJ. *The Physics of Vibrations and Waves*. Wiley, 5th edition, 1999. ISBN 0-471-98543-0.

Paulides MM, Bakker JF, Neufeld E, van der Zee J, Jansen PP, Levendag PC, and van Rhoon GC. The HYPERcollar: A novel applicator for hyperthermia in the head and neck. *Int J Hyperthermia*, 23(7):567–576, 2007.

Persson HW and Hertz CH. Acoustic impedance matching of medical ultrasound transducers. *Ultrasonics*, 23(2):83–89, 1985.

Ponce AM, Vujaskovic Z, Yuan F, Needham D, and Dewhirst MW. Hyperthermia mediated liposomal drug delivery. *Int J Hyperthermia*, 22(3):205–213, 2006.

Ritter TA, Shrout TR, Tutwiler R, and Shung KK. A 30-MHz piezo-composite ultrasound array for medical imaging applications. *IEEE Trans Ultrason Ferroelectr Freq Control*, 49(2), February 2002.

Ryan TP. *Modern regression methods*, chapter 2 - Diagnostics and remedial measures, pages 44–100. Wiley, 1997. ISBN 0-471-52912-5.

Saleh KY and Smith NB. Two-dimensional ultrasound phased array design for tissue ablation for treatment of benign prostatic hyperplasia. *Int J Hyperthermia*, 20 (1):7–31, 2004.

Saleh KY and Smith NB. A 63 element 1.75 dimensional ultrasound phased array for the treatment of benign prostatic hyperplasia. *Biomed Eng Online*, 4(39), June 2005.

Sanghvi NT, Fry FJ, Bihrle R, Foster RS, Phillips MH, Syrus J, Zaitsev AV, and Hennige CW. Noninvasive surgery of prostate tissue by high-intensity focused ultrasound. *IEEE Trans Ultrason Ferroelectr Freq Control*, 43(6):1099–1110, November 1996.

Seip R, Chen W, Tavakkoli J, Frizzell LA, and Sanghvi NT. High-intensity focused ultrasound (HIFU) phased arrays: Recent developments in transrectal transducers and driving electronics design. *Third International Symposium on Therapeutic Ultrasound*, June 2003.

Sherar M, Liu F, Pintilie M, Levin W, Hunt J, Hill R, Hand J, Vernon C, van Rhoon G, van der Zee J, Whaley J, and Machin D. Relationship between thermal dose and outcome in thermoradiotherapy treatments for superficial recurrences of

breast cancer: Data from a phase III trial. *Int J Radiation Oncology Biol Phys*, 39(2):371–380, 1997.

Smith NB, Merrilees NK, Dahleh M, and Hynynen K. Control system for an MRI compatible intracavitary ultrasound array for thermal treatment of prostate disease. *Int J Hyperthermia*, 17(3):271–282, 2001.

Smith SW, Pavy Jr. HG, and von Ramm OT. High-speed ultrasound volumetric imaging system - part I: Transducer design and beam steering. *IEEE Trans Ultrason Ferroelectr Freq Control*, 38(2):100–108, 1991.

Sokka SD and Hynynen KH. The feasibility of MRI-guided whole prostate ablation with a linear aperiodic intracavitary ultrasound phased array. *Phys Med Biol*, 45: 3373–3383, 2000.

Song CW, Park HJ, Lee CK, and Griffin R. Implications of increased tumor blood flow and oxygenation caused by mild temperature hyperthermia in tumor treatment. *Int J Hyperthermia*, 21(8):761–767, 2005.

Starnes CO. Coley's toxins in perspective. *Nature*, 357:11–12, 1992.

Stauffer PR. Evolving technology for thermal therapy of cancer. *Int J Hyperthermia*, 21(8):731–744, 2005.

Strutt JW. On the resultant of a large number of vibrations of the same pitch and of arbitrary phase. *Phil. Mag. Series 5*, 10(60):73–78, 1880.

Strutt JW. *The theory of sound*, volume 1, §42a, pages 35–42. Dover Publications, 1894. ISBN 0-486-60292-3.

Strutt JW. *The theory of sound*, volume 2, §278, pages 106–109. Dover Publications, 1896. ISBN 0-486-60293-1.

Sullivan DM, Buechler D, and Gibbs FA. Comparison of measured and simulated data in an annular phased array using an inhomogeneous phantom. *IEEE Trans Microwave Theory Tech*, 40(3):600–604, 1992.

Sun L, Schiano J, and Smith NB. Novel adaptive control system for ultrasound hyperthermia treatment of prostate disease. *IEEE Ultrasonics Symposium*, 10 (60):1274–1277, 2003.

ter Harr GR. Ultrasound focal beam surgery. *Ultrasound Med Biol*, 21(9):1089–1100, 1995.

ter Harr GR. Therapeutic ultrasound. *Eur J Ultrasound*, 9:3–9, 1999.

ter Harr GR. Therapeutic applications of ultrasound. *Prog Biophys Mol Biol*, 93: 111–129, 2007.

Tsung K and Norton JA. Lessons from Coley's toxin. *Surgical Oncology*, 15:25–28, 2006.

U.S. Department of Defense. MIL-STD-1376B: Piezoelectric ceramic material and measurements guidelines for sonar transducers, February 1995.

Vernon CC, Hand JW, Field SB, Machin D, Whaley JB, van der Zee J, van Putten WLJ, van Rhoon GC, van Dijk JDP, González DG, Liu F, Goodman P, and Sherar M. Radiotherapy with or without hyperthermia in the treatment of superficial localized cancer: Results from five randomized controlled trials. *Int J Radiation Oncology Biol Phys*, 35(4):731–744, 1996.

Wang Y, Hunt JW, Foster FS, and Plewes DB. Tissue ultrasound absorption measurement with MRI calorimetry. *IEEE Trans Ultrason Ferroelectr Freq Control*, 46(5):1192–1200, September 1999.

Wells PNT. Absorption and dispersion of ultrasound in biological tissue. *Ultrasound Med Biol*, 1:369–376, 1975.

Wojcik G, DeSilets C, Nikodym L, Vaughan D, Abboud N, and Mould Jr. J. Computer modeling of diced matching layers. *IEEE Ultrasonics Symposium*, pages 1503–1508, 1996.

Wooh S and Shi Y. Influence of phased array element size on beam steering behavior. *Ultrasonics*, 36:737–749, 1998.

Wu F, Thomas J-L, and Fink M. Time reversal of ultrasonic fields - part II: Experimental results. *IEEE Trans Ultrason Ferroelectr Freq Control*, 39(5):567–578, 1992.

Wust P, Hildebrandt B, Sreenivasa G, Rau B, Gellerman J, Riess H, and Schlag PM. Hyperthermia in combined treatment of cancer. *Lancet Oncol*, 3(8):487–497, 2002.

Yatvin MB, Wesinstein JN, Dennis WH, and Blumenthal R. Design of liposomes for enhanced local release of drugs by hyperthermia. *Science*, 202:1290–1293, 1978.

Zhou S, Wojcik GL, and Hossack JA. An approach for reducing adjacent element crosstalk in ultrasound arrays. *IEEE Trans Ultrason Ferroelectr Freq Control*, 50 (12):1752–1761, December 2003.